การตอบสนองต่อแก๊สของฟิล์มบางแคลเซียมคอปเปอร์ไททาเนตโดปด้วยนิกเกิลสังเคราะห์ด้วยวิธีโซล-เจล

นางสาวอริสรา บุญธรรม

วิทยานิพนธ์นี้เป็นส่วนหนึ่งของการศึกษาตามหลักสูตรปริญญาวิทยาศาสตรมหาบัณฑิต
สาขาวิชาฟิสิกส์ ภาควิชาฟิสิกส์
คณะวิทยาศาสตร์ จุฬาลงกรณ์มหาวิทยาลัย
ปีการศึกษา 2560

GAS SENSING RESPONSE OF NICKEL DOPED CALCIUM COPPER TITANATE THIN FILMS SYNTHESIZED BY SOL-GEL METHOD

Miss Arisara Boontum

A Thesis Submitted in Partial Fulfillment of the Requirements
for the Degree of Master of Science Program in Physics
Department of Physics
Faculty of Science
Chulalongkorn University
Academic Year 2017

Thesis Title	GAS SENSING RESPONSE OF NICKEL DOPED CALCIUM COPPER TITANATE THIN FILMS SYNTHESIZED BY SOL-GEL METHOD
By	Miss Arisara Boontum
Field of Study	Physics
Thesis Advisor	Associate ProfessorSatreerat Hodak, Ph.D.
Thesis Co-Advisor	Anurat Wisitsoraat, Ph.D.

Accepted by the Faculty of Science, Chulalongkorn University in Partial Fulfillment of the Requirements for the Master's Degree

.....Dean of the Faculty of Science
(Associate ProfessorPolkit Sangvanich, Ph.D.)

THESIS COMMITTEE

.....Chairman
(Assistant ProfessorRattachat Mongkolnavin, Ph.D.)

.....Thesis Advisor
(Associate ProfessorSatreerat Hodak, Ph.D.)

.....Thesis Co-Advisor
(Anurat Wisitsoraat, Ph.D.)

.....Examiner
(Sathon Vijarnwannaluk, Ph.D.)

.....External Examiner
(Panwong Kuntanawat, Ph.D.)

อริสรา บุญธรรม : การตอบสนองต่อแก๊สของฟิล์มบางแคลเซียมคอปเปอร์ไททาเนตโดปด้วยนิกเกิลสังเคราะห์ด้วยวิธีโซล-เจล (GAS SENSING RESPONSE OF NICKEL DOPED CALCIUM COPPER TITANATE THIN FILMS SYNTHESIZED BY SOL-GEL METHOD) อ.ที่ปรึกษาวิทยานิพนธ์หลัก: รศ. ดร.สตรีรัตน์ โฮดัค, อ.ที่ปรึกษาวิทยานิพนธ์ร่วม: ดร.อนุรัตน์ วิศิษฏ์สรอรรถ, 128 หน้า.

ฟิล์มบางแคลเซียมคอปเปอร์ไททาเนตโดปนิกเกิล (Ni-doped CCTO) ที่เตรียมด้วยนิกเกิลออกไซด์ (NiO) และนิกเกิลอะซิเตท ($C_4H_6NiO_4$) ถูกสังเคราะห์ด้วยวิธีโซล-เจล โดยในกระบวนการปลูกฟิล์มนั้นได้ทำการปลูกฟิล์มที่มีปริมาณความเข้มข้นของตัวโดปนิกเกิลต่าง ๆ รวมทั้งฟิล์มที่ไม่โดปสี่ชั้นลงบนแผ่นรองรับซิลิคอนและอลูมินาด้วยเทคนิคการปั่นหมุนและให้ความร้อนในแต่ละชั้นฟิล์มด้วยอุณหภูมิ 800 องศาเซลเซียส การวิเคราะห์ตัวอย่างที่ได้ทั้งหมดอาศัยเทคนิคการเลี้ยวเบนรังสีเอกซ์ (XRD) เทคนิคการวิเคราะห์ธาตุ (EDX) เอกซ์เรย์โฟโตอิมิสชั่นสเปกโทรสโกปี (XPS) และกล้องจุลทรรศน์อิเล็กตรอนแบบส่องกราดชนิดฟิลด์อีมิสชั่น (FESEM) เฉพาะฟิล์มที่โดปเตรียมด้วยนิกเกิลออกไซด์ได้ทำการวิเคราะห์ด้วยรามานสเปกโทรสโกปี นอกจากนี้ฟิล์มแคลเซียมคอปเปอร์ไททาเนตถูกสร้างเป็นอุปกรณ์เซนเซอร์เพื่อวัดสมบัติการตอบสนองต่อแก๊ส ผลของการเลี้ยวเบนรังสีเอกซ์แสดงเฟสหลักของฟิล์มที่ไม่โดปและโดปนิกเกิลเป็นโครงสร้างลูกบาศก์เพอรอพสไกต์และมีการเจือปนของรูไทล์ไททาเนียมไดออกไซด์เพียงปริมาณเล็กน้อย จากสัญญาณ XPS ยืนยันว่านิกเกิลที่มีเลขออกซิเดชัน 2+ พบในฟิล์มแคลเซียมคอปเปอร์ไททาเนตโดปนิกเกิล นอกจากนี้ภาพ FESEM ของฟิล์ม 4 ชั้นบนแผ่นรองรับซิลิคอนแสดงความหนาของฟิล์มประมาณ 400-600 นาโนเมตรและพื้นผิวของฟิล์มประกอบด้วยอนุภาคเม็ดกลม ในกรณีของการวัดสมบัติการตอบสนองต่อแก๊สของฟิล์มได้ทำการทดสอบต่อแก๊สชนิดต่าง ๆ (ไนโตรเจนไดออกไซด์ ไฮโดรเจน แอมโมเนีย ไฮโดรเจนซัลไฟด์ และเอทานอล) ซึ่งฟิล์มทั้งหมดแสดงความจำเพาะต่อการตอบสนองแก๊สดีที่สุดต่อแก๊สไฮโดรเจนซัลไฟด์เมื่อเปรียบเทียบกับแก๊สอื่นๆ นอกจากนี้การตอบสนองต่อแก๊สของฟิล์มเพิ่มขึ้นตามปริมาณการโดปนิกเกิล เซนเซอร์แคลเซียมคอปเปอร์ไททาเนตโดปนิกเกิล 7 เปอร์เซ็นต์โดยน้ำหนักเตรียมด้วยนิกเกิลออกไซด์แสดงการตอบสนองต่อการรับรู้มากที่สุด 112 ภายใต้แก๊สไฮโดรเจนซัลไฟด์เข้มข้น 10 พีพีเอ็ม ที่ 250 องศาเซลเซียส ขณะที่การตอบสนองต่อการรับรู้มากที่สุดของเซนเซอร์แคลเซียมคอปเปอร์ไททาเนตโดปนิกเกิล 5 เปอร์เซ็นต์โดยน้ำหนักเตรียมด้วยนิกเกิลอะซิเตทเป็น 175 ที่ 300 องศาเซลเซียส ในทั้งสองกรณีการตอบสนองต่อการรับรู้ของฟิล์มแคลเซียมคอปเปอร์ไททาเนตโดปนิกเกิลมากกว่าฟิล์มที่ไม่โดปแสดงให้เห็นว่าตัวโดปนิกเกิลในฟิล์มที่ทำหน้าที่เป็นตัวเร่งปฏิกิริยาปรับปรุงการตอบสนองต่อการรับรู้ให้ดีขึ้น

ภาควิชา	ฟิสิกส์	ลายมือชื่อนิสิต	.....
สาขาวิชา	ฟิสิกส์	ลายมือชื่อ อ.ที่ปรึกษาหลัก	.....
ปีการศึกษา	2560	ลายมือชื่อ อ.ที่ปรึกษาร่วม	.....

5772212623 : MAJOR PHYSICS
KEYWORDS: CALCIUM COPPER TITANATE, SOL-GEL TECHNIQUE , HYDROGEN SULFIDE GAS SENSOR

ARISARA BOONTUM: GAS SENSING RESPONSE OF NICKEL DOPED CALCIUM COPPER TITANATE THIN FILMS SYNTHESIZED BY SOL-GEL METHOD. ADVISOR: ASSOC. PROF.SATREERAT HODAK, Ph.D., CO-ADVISOR: ANURAT WISITSORAAT, Ph.D., 128 pp.

Nickel-doped calcium copper titanate (Ni-doped CCTO) thin films prepared by nickel oxide (NiO) and nickel (II) acetate ($C_4H_6NiO_4$) have been synthesized using sol-gel method. Four layers of Ni-doped CCTO films with various nickel dopant concentrations including undoped film were deposited by a spin coating technique on silicon and alumina substrates. Each film layer was annealed at a fixed annealing temperature of 800 °C. All samples were characterized by X-ray diffraction (XRD), energy dispersive X-ray spectroscopy (EDX), X-ray photoelectron spectroscopy (XPS) field emission scanning electron microscope (FESEM). Only the doped films prepared by NiO were analyzed by Raman spectroscopy. Moreover, the CCTO films were fabricated as gas sensors to measure gas sensing properties. XRD patterns showed that the main phase of undoped and Ni-doped CCTO were a cubic perovskite structure and there is only a small amount of impurity phase of rutile TiO_2. The XPS signals confirmed that $Ni^{2}+$ was found in Ni-doped CCTO films. Moreover, FESEM images presented the films thickness of approximately 400-600 nm for four-layered films on silicon and the surface of the films contained granular particles. In case of gas sensing property measurements, the obtained films were tested towards different types of gases (NO_2, H_2, NH_3, H_2S and ethanol). All films exhibited the best selectivity towards H_2S compared to other gases. In addition, the sensor response of the films increases with increasing Ni-doping concentrations. The 7 wt% Ni-doped CCTO sensor prepared by NiO exhibited the highest sensor response of 112 under 10 ppm H_2S at 250 °C while the highest sensor response of 5 wt% Ni-doped CCTO sensor prepared by nickel (II) acetate was 175 at 300 °C. In both cases, the sensor response of Ni-doped CCTO films is more than that of the undoped indicating that Ni-dopants in the films acting as a catalyst improve much better sensor responses.

Department:	Physics	Student's Signature	.....
Field of Study:	Physics	Advisor's Signature	.....
Academic Year:	2017	Co-Advisor's Signature	.....

ACKNOWLEDGEMENTS

The author would like to express my deep gratitude to my advisor, Associate Professor Dr. Satreerat K Hodak for her patience, understanding, encouragement, kindness, friendly and useful suggestions discussion during this work.

The author would like to specially thanks Dr. Anurat Wisitsoraat and Mr. Disayut Phokharatkul for teaching me how to fabricate gas sensors and help me on gas-sensing properties measurements. Also, the author would like to really thank to Dr. Adisorn Tuantranont and National Electronics and Computer technology (NECTEC) for gas-sensing facilities.

The author would like to really thank Assistant Professor Dr. Jose Hodak for guiding me about gas sensing mechanism.

The author wishes to greatly thank to Assistant Professor Dr. Rattachat Mongkolnavin for being the chairman, Dr. Sathon Vijarnwannaluk and Dr. Panwong Kuntanawat and committee numbers of this thesis.

The author would also take this opportunity to thanks the Department of Physics, Faculty of science, Chulalongkorn University for providing financial support and the grants to accomplish this thesis. The department sponsored me for expenses to attend the conferences.

The author would like to thank to the Science Achievement Scholarship of Thailand (SAST) and the 90th Year Chulalongkorn Scholarship from Graduate School, Chulalongkorn University for supporting my tuitions and research budgets in this work.

Finally, the author is thankful to my family and friends for their love, understanding, inspiration, guidance, encouragement and support throughout my entire study.

CONTENTS

Page

Page

List of Tables

Table Page

List of Figures

Figure Page

CHAPTER I

INTRODUCTION

1.1 Motivation

$CaCu_3Ti_4O_{12}$ (CCTO) is one of materials that are widely known for many electronic applications such as capacitors, memory devices, power systems and the automotive industry [1, 2]. It is used many electronic applications because of its giant dielectric constant (10^4 - 10^5) [3, 4] that is not change in a wide range of temperature and frequency. In addition, one of interested applications of CCTO is to use to apply as gas sensors for several gases. CCTO thin films were prepared by pulsed laser deposition onto poly (methyl methacrylate) (PMMA) microsphere template substrates and they exhibited sensor response towards H_2 under temperature 30 – 600 ºC as reported by Kim, I.-D. et al [5]. Joanni, E. et al. studied RF sputtering synthesis and the fabrication gas sensor of CCTO thin and they found that the porous microstructure on CCTO film surface lead to enhanced sensor response towards O_2 [6]. Moreover, Para, R. et al. found that gas sensing properties of CCTO thin films exhibited high sensor response and short response time towards O_2 and N_2 at 220 - 290 ºC [7]. From table 1.1, it can be observed that the research about CCTO sensor is mostly involved with gases that are not so much hazardous.

Table 1.1: Gas sensing properties of CCTO sensor [8].

Materials	Methods	Sensor response	Concentration	Temp. (ºC)	Reference
CCTO+Al_2O_3 substrate + Pt electrode	Pulsed laser deposition	H_2 (1.25)	5 %	30 - 600	Kim, I.-D. et al [5]
CCTO + Si/SiO_2/Ti + Pt substrates	RF sputtering	O_2 (1.5)	12 %	100 - 200	Joanni, E. et al. [6]
CCTO + Si/SiO_2 substrate + Pt electrode	Sol-Gel	O_2 and N_2	220 -290	-	Para, R. et al. [7]

In the past, it can be observed that the research of hazardous detection CCTO sensor is very few. The hazardous gases are very harmful and dangerous to vegetation, buildings and human if a leakage occurs. They are toxic, combustible and inflammable gases. For example, carbon monoxide (CO) affects a cellular respiration and it is also flammable [9]. Hydrogen (H_2) with the concentration higher than 4% in air can explode and flame [10]. Ammonia (NH_3) can irritate the respiratory system, skin and eyes [11]. Moreover, hydrogen sulfide (H_2S) which is one of dangerous gases because of its toxicity, flammable and bad smell like a rotten-egg [12]. H_2S is caused by chemical laboratories, natural gas, automobile exhaust gas, sewage plants, hot springs and coal mines industries [12, 13]. There are many danger of hydrogen

sulfide. For example, H_2S have eroded concrete sewers and causes the reduction of concrete thickness [14]. H_2S inhalation at low-level concentrations can irritate organs involved in the process of respiration and human can be also numb, if they smell high concentrations of H_2S [15, 16]. In addition, H_2S gas can cause hypesthesia, headache or even block the transfer of oxygen to blood cells in the human respiratory system [16]. The human sense of smell can recognize exposure to H_2S for 8 hour at 10 ppm H_2S. H_2S is a colorless gas [17] so, the H_2S detection is important for human safety and environment at a low concentration.

Recently, the researchers in our laboratory discovered that CCTO thin film can interact with H_2S gas and the interaction between CCTO and H_2S gas lead to change electrical properties of CCTO, so the CCTO thin film are used to fabricate H_2S gas sensor. Preparation process of CCTO thin films could be done with several methods such as sol-gel method [18], metal organic chemical vapor deposition (MOCVD) [19], pulsed laser deposition (PLD) [20] and reactive RF magnetron sputtering [21]. Compared with other methods, sol-gel method is a simple process using low cost apparatus and homogeneous material with large area coating on complex substrate can be obtained easily. Moreover, doping with different elements and concentrations can be done during the growth process to improve some properties of CCTO films. As mention earlier, previous studies in our laboratory have shown that the Fe-doped CCTO films exhibited good sensor response towards H_2S [22]. The undoped and 9 wt% Fe-doped CCTO films exhibited the sensor response of 10 and 126 to 10 ppm H_2S at 250°C, respectively. The best sensor response for 9 wt% Fe-doped CCTO films operating was twelve times better than with undoped CCTO. However, the Fe-doped CCTO sensors still exhibited moderate response time and

large recovery time. The undoped and 9 wt% Fe-doped CCTO films presented the response time of ~40 s and ~8.5 s, respectively while the recovery time is ~1100 s and ~500 s, respectively. Thus, it is of interest to enhance the CCTO response towards H_2S by means of finding the most suitable doping element that allows high sensor response. Many dopants that could strongly interact with sulfur and afford for the transfer of two electrons to the system are such Mn, Mo, Co and Ni.

The gas sensing properties of Ni-doped CCTO films were not examined in recent reports. In the past, it was reported that Ni-doped materials improve the sensor response toward several hazardous gases [22]. For example, NiO modified SnO_2 film exhibited sensor response and recovery time of 440 and 4 min for 10 ppm H_2S at room temperature, respectively while SnO_2 exhibited sensor response and recovery time of 15 and 8 min [23]. Rambua, A.P. et al. showed that Ni-doped ZnO films were the most sensitive to ammonia against LPG and ethanol. In addition, the increase of Ni concentration affected to increase the sensor response [24]. Wang, X. et al. reported that Ni-doped ZnO nanofibers showed higher sensitivities to flammable acetylene (C_2H_2) than that of pure ZnO nanofibers, and Ni doping concentration at 5% by weight obtained the best sensor response [25]. In other research work, Jing, Z. et al. studied the gas sensing properties of Ni-doped gamma-Fe_2O_3 synthesized by anhydrous solvent method. They found that 15 mol % Ni-doped γ-Fe_2O_3 sensors exhibited good sensor response towards both acetone and ethanol which are vapor gases that are not too harmful to human death [26]. Furthermore, gas sensing properties of bare CuO microspheres, flower-like NiO and CuO-NiO core-shell microspheres were studied by Wang, Y. et al [27]. They found that the response of

CuO-NiO core-shell microspheres towards H_2S was approximately two times better than with bare CuO microspheres and flower-like NiO as shown in Fig. 1.1.

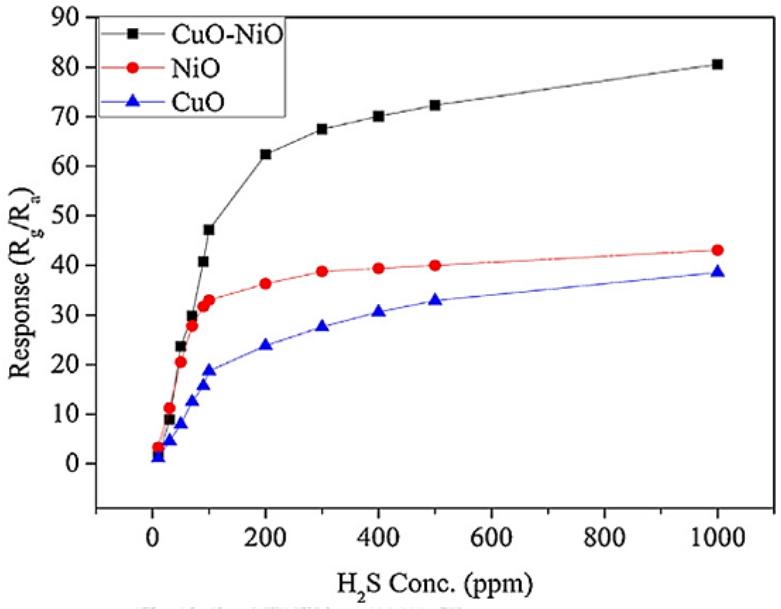

Figure 1.1: Response of bare CuO microspheres, flower-like NiO and CuO-NiO core-shell microspheres as function of temperature [28].

This indicates that NiO improve to enhanced response of CuO and NiO is also catalytic in chemical reaction [28]. Therefore, Ni-doping was interested in thesis work due to CCTO thin film contains of CuO. Moreover, we expect that Ni-doped CCTO can detect other toxic gases above H_2S gas. The gas sensing properties of several Ni-doped materials can observe in Table 1.2.

Table 1.2: Gas-sensing response of recently reported metal oxide sensors doped with Ni towards different types of gases.

Materials	Methods	Temp. (°C)	Concentration (ppm)	Response gas (s)	Reference
Fe-doped CCTO films	Sol-gel method	250	10	H_2S ~126	Pongpaiboo-nkul,S. et.al. [22]
SnO_2: NiO thin films	RF sputtering	Room temp.	10	H_2S ~440	Kaur, M.,et.al. [24]
Ni-doped ZnO films	Spin coating	190	850	ammonia 9.3	Rambua, A.P. et.al. [25]
Ni 5wt % doped ZnO nanofibers	Electro- spinning	250	2000	acetylene ~16.9	Wang, X., et.al. [26]
Ni 15 mol% doped γ-Fe_2O_3 nanopowders	Anhydrous solvent	270	1000	Ethanol 45 Acetone 50	Jing, Z. [27]
Ni-doped SnO_2 hollow spheres	Carbon microsphere template	300	50	n-butanol ~29	Liu, X. [28]
Fe_2O_3 nanopartic le decorated NiO Nanoplate	A Facile solvothermal route	300	200	H_2S 26.5	Sun, G., et.al. [17]
Ni-doped SnO_2 nanofiber	Modified electrospinning technique followed with hot-press and calcination	250	20	NO_2 90.3	Li, W., et.al. [29]
Ni-doped WO_3 nanoneedles	Aerosol assisted chemical vapor deposition method	200	5	H_2S ~2.8	Vilic, T., et.al. [30]

In this work we interested in synthesis of Ni-doped CCTO thin films by a sol-gel method for enhancing the CCTO response towards toxic gases especially H_2S. This is because CCTO contains copper ions in its structure which are capable of interaction with sulfide in H_2S. The concentrations of nickels in the films that could be prepared during the growth process were mainly focused. Nickel oxide (NiO) and nickel (II) acetate ($C_4H_6NiO_4$) were used as the compounds for Ni dopant. After the gas sensing response and performance of each film are examined, the correlations between the physical and chemical properties with the gas sensing properties of Ni-doped CCTO thin films are investigated. The gas sensing mechanism which is the key to explain the behavior of the gas properties of Ni-doped CCTO films is described in this thesis.

1.2 Objectives of the thesis

1. To synthesize Ni-doped $CaCu_3Ti_4O_{12}$ thin films using NiO and Nickel (II) acetate as starting materials prepared by a sol-gel method by varying nickel concentrations in the films.

2. To study the crystal structure, the surface morphology, oxidation sate and chemical structure of the prepared films by X-ray diffraction technique (XRD), field emission scanning electron microscope (FE-SEM), X-ray photo emission spectroscopy (XPS), Energy dispersive x-ray spectroscopy (EDX) and Raman spectroscopy.

3. To fabricate film gas sensors and measure their gas sensing responses towards different types of gases such as ethanol, acetylene, ammonia and hydrogen sulfide.

4. To compare the gas sensing result with undoped and Fe-doped CCTO devices.

1.3 Overview of the thesis

Chapter II: This chapter explains the crystal structure of undoped CCTO and Ni-doped CCTO, the basic principle of sol-gel method and the mechanisms of gas sensor.

Chapter III: This chapter describes the basic principles of characterization techniques (XRD, FE-SEM, XPS, Raman spectroscopy and Gas sensing measurement).

Chapter IV: This chapter explains the experiment process that consists of synthesis Ni-doped CCTO solution, spin coating technique, gas sensors fabrication and characterization of films.

Chapter V: This chapter illustrates the effect of Ni-doped concentrations on structure properties, surface morphology and gas sensing properties are shown and analyzed.

Chapter VI: It is conclusion of the thesis.

CHAPTER II

THEORETICAL BACKGROUND

2.1 Structure of calcium copper titanate ($CaCu_3Ti_4O_{12}$: CCTO) material

Calcium copper titanate ($CaCu_3Ti_4O_{12}$ or CCTO) was firstly synthesized by Alfred Deschanvres and his coworkers in 1967 [1]. CCTO is widely known to be $ACu_3Ti_4O_{12}$ (A = Ca, Sr, Ba) type oxides and the crystal structure of CCTO is pseudo cubic perovskite oxide structure as shown in Fig. 2.1. The pseudo cubic perovskite oxide structure has related cubic perovskite (ABO_3) with slightly tilted TiO_6 octahedra at which the central titanium atom is bonded to six oxygen atoms. The tilt angle of the TiO_6 octahedra is 20º with respect to the unit cell axis. Tilting of TiO_6 octahedra bring about a square-planar environment for Cu for which each copper atom is bonded to four oxygen atoms. The corner and body centered positions of pseudo cubic perovskite oxide structure are calcium atoms. Moreover, the cubic structure of CCTO is stable in the temperature range of 100 - 600 K and the lattice constant of CCTO is 7.391 Å [2].

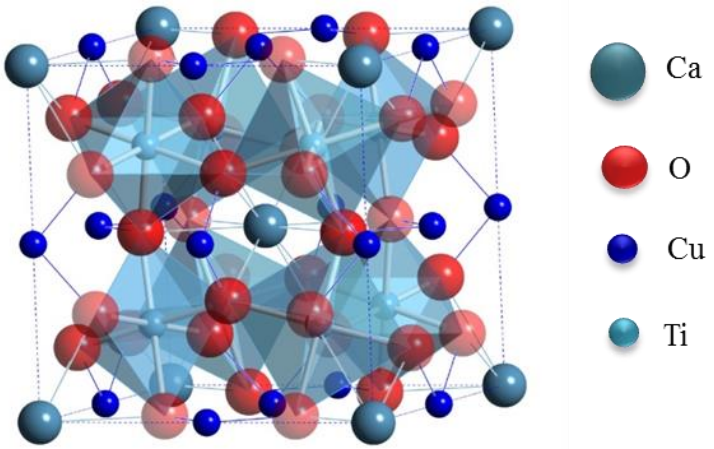

Figure 2.1: The pseudo cubic perovskite oxode structure of CCTO [8].

2.2 Dielectric properties of CCTO material

Dielectric material is an insulating material or a very poor conductor to electric current. There are two types of dielectric material; non-polar and polar dielectrics. A non-polar molecule is known to be a molecule without a per manent dipole. The charges in a non-polar molecule regularly spreads positive and negative charges as presented in Fig. 2.2 (a). When the non-polar molecule is introduced in external electric field, the electric field affects the movement of positive and negative charges in a molecule in the opposite directions. The positive charges within the molecule are moved slightly in the direction of the electric field while the negative charges are moved slightly in the direction opposite to the direction of the electric field as shown in Fig. 2.2 (b). The induced electric dipole moments are produced by the slight separation of charge. In addition, if there is no applied external electric field, the non-polar molecule loses its polarity. Then, the charges are returned to its original state.

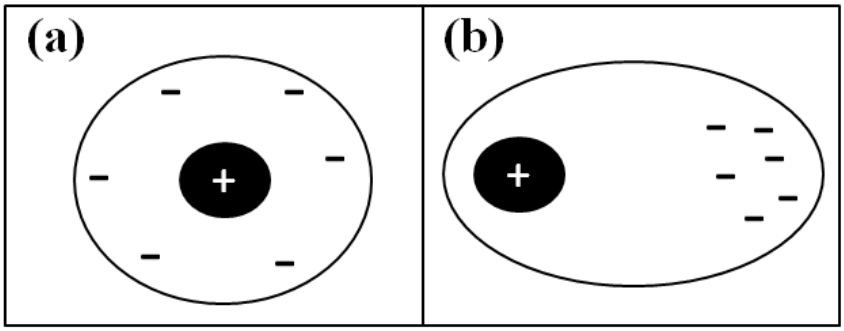

Figure 2.2: (a) a non-polar molecule of dielectric material and (b) the movement of charges under the external electric field.

In term of polar molecule, there are the permanent dipole moments in the polar molecule. The dipoles on molecule are oriented randomly in the absence of an external electric field causing a zero net dipole moment as illustrated in Fig. 1.3 (a). As an external electric field is applied, the polar molecules are regularly oriented themselves along the electric field direction as shown in Fig. 2.3 (b). The orientation of polar molecules along the electric field direction is called orientational polarization.

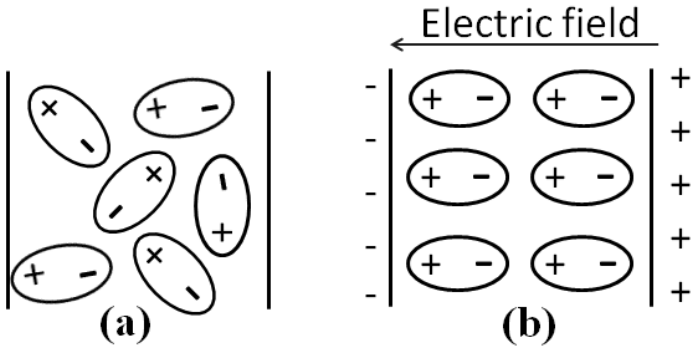

Figure 2.3: (a) and (b) The orientation of polar molecules without an applied external electric field and under an applied external electric field, respectively.

Thus, the creation of a net dipole moment is produced in the dielectric material under an applied electric field. The dipole moment per net unit volume is called polarization *($\bar{P}$)*.

$$\bar{P} = \chi_e \bar{E} \qquad (2.1)$$

where $\bar{P}$ is polarization due to the applied electric field (E).

χ_e is the electric susceptibility may be complex number.

The electric displacement field $(\bar{D})$ is defined in the following.

$$\bar{D} = \varepsilon_0 \bar{E} + \bar{P} \tag{2.2}$$

$$\bar{D} = \varepsilon_0 (1 + \chi_e) \bar{E} \tag{2.3}$$

$$\bar{D} = \varepsilon_0 \varepsilon_r \bar{E} \tag{2.4}$$

$$\bar{D} = \varepsilon \bar{E} \tag{2.5}$$

where ε_0 is the permittivity of vacuum which is 8.85×10^{-12} F/m.

$\varepsilon_r = 1 + \chi_e$ is the relative permittivity of the material which known as the dielectric constant.

$\varepsilon = \varepsilon_0 \varepsilon_r$ is the permittivity or dielectric constant of material.

The complex dielectric constant (ε^*) can also be defined as

$$\varepsilon^* = \varepsilon_0 (1 + \chi_e) = \varepsilon' + i\varepsilon'' \tag{2.6}$$

where ε' is the real part of complex dielectric constant

ε'' is the imaginary part of complex dielectric constant

The imaginary part (ε'') relates to the loss that is heat energy form in dielectric material. This loss is defined as loss tangent $(\tan\delta)$.

$$\tan\delta = \frac{\varepsilon''}{\varepsilon'} \tag{2.7}$$

$\tan\delta$ is equal to zero in lossless material which is no loss. The good dielectric material must has few loss tangents. The loss tangent of polycrystalline and single crystal CCTO is $\tan\delta > 0.05$ at 1 kHz [1]. Moreover, the dielectric constant or the

relative permittivity involves with capacitance that is ability to store opposite charges of a capacitor. The capacitors are fabricated by giant dielectric constant material, so they are able store high opposite charges. Generally, the dielectric constant of a material is always more than 1. In case of the capacitance of parallel-plates capacitor as seen in Fig. 2.4 is defined in Equation (2.8).

$$C = \frac{\varepsilon A}{d} = \frac{\varepsilon_r \varepsilon_0 A}{d} \qquad (2.8)$$

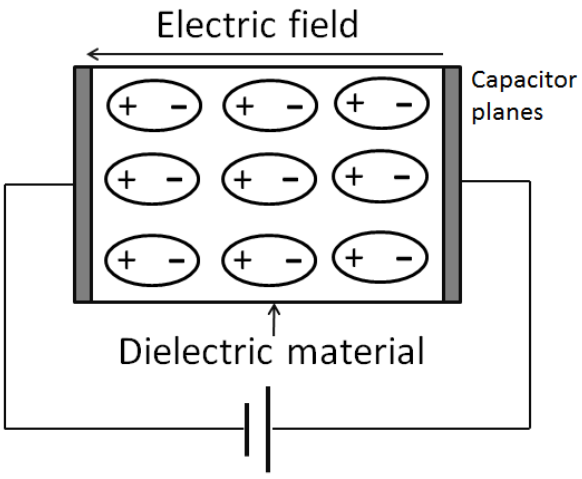

Figure 2.4: The diagram of parallel-plates capacitor.

As known, the high dielectric constant of CCTO material depends on the crystal structure form. For example, the CCTO single crystal and ceramic exhibited the dielectric constant of 10^5 and 10^4 [4, 31], respectively whereas the dielectric constant of CCTO film is 10^4 [1]. This high dielectric constant is stable in the frequency range of 10^4- 10^6 Hz and large temperature range of 100 - 600 K [4, 32]. For this reason, CCTO material have been widely attracted and used as electronic device. There are two ideas to explain the giant dielectric constant of CCTO as follows.

1. The intrinsic properties of CCTO material

Subramanian et al. reported that the giant dielectric constant of CCTO relates to the intrinsic properties of material [32]. The intrinsic properties of material is perfectly stoichiometric, no defect, and only single domain crystal structure. In structure of CCTO can be explained that the TiO_6 octahedral tilt distortions affect the occurring local dipole moments and the tension on the Ti-O bonds lead to an increase the polarization of the structure. Moreover, substitution of Ti^{4+} (acceptors) and Ca^{2+} (donors) sites with other elements lead to increasing or decreasing polarization [1].

2. The extrinsic properties of CCTO material

In the case of the giant dielectric constant of CCTO, CCTO are investigated by the extrinsic properties which are point, line, or planar defects, or other crystal imperfections or more generally, with sample microstructure, morphology, domain boundaries and boundary layers. The internal barrier layer capacitor (IBLC) model is widely accepted to explain behavior of the high dielectric constant of CCTO material and a modified model structure is illustrated in Fig. 2.5(a). CCTO grain and grain boundary behave to be n-type and p-type semiconducting carriers, respectively. Some groups suggested that the grain boundary contains CuO phase [33]. Therefore, there are a lot of grain and grain boundary in material microstructure that these structures are similar to the electrical circuit with many capacitors components. Fig.2.5 (b) shows the circuit diagram that includes a series of parallel resistors and capacitors. The RC elements are two sets of parallel resistors and capacitors and they are known as set of R_gC_g and $R_{gb}C_{gb}$. The R_g and R_{gb} refer to resistance of grain and grain boundary respectively, while C_g and C_{gb} refer to capacitance of grain and grain

boundary, respectively [34]. From Fig. 2.5(a), the capacitance (C_i) of each element can be identify as Equation (2.9)

$$C_i = \frac{\varepsilon_{gb}\,\varepsilon_0\,d_g^2}{t_{gb}} \qquad (2.9)$$

Where d_g is grain size.

t_{gb} is boundary layer thickness.

ε_{gb} is the dielectric permittivity of the grain boundary layer.

The capacitance per unit area is in the Equation (2.10)

$$C_i = \frac{\varepsilon_{gb}\,\varepsilon_0\,d_g}{t_{gb}} \qquad (2.10)$$

From $$C = \frac{\varepsilon_r\,\varepsilon_0}{t} \qquad (2.11)$$

Therefore, the dielectric permittivity (ε_r) can be defined as equation (2.12).

$$\varepsilon_r = \frac{\varepsilon_{gb}\,d_g}{t_{gb}} \qquad (2.12)$$

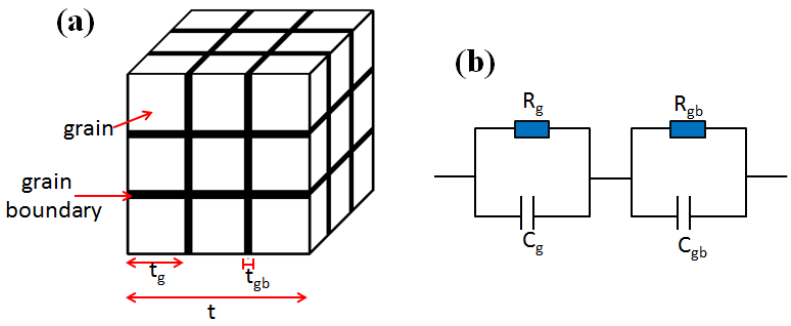

Figure 2.5: (a) Model of grain and grain boundary in material structure and (b) the circuit diagram of two sets of parallel resistors and capacitors.

2.3 The basic principle of sol-gel method

The sol-gel method is one of wet chemical method which is widely used to synthesize materials such as thin films, ceramics, and glasses because of low cost apparatus, good homogeneity, precise composition control, large area coating, complex substrate coating and low temperatures for processing [8]. The used precursors are formed a colloidal suspension or sol that is liquid containing solid particles in suspension. Then, the particles in the sol are converted to gel. The gel is state of a solid network containing liquid components. The solid network is formed agglomeration of colloidal particles. There are three reactions during sol-gel process as shown in Equations (2.10)-(2.12).

Hydrolysis: $M - O - R + H_2O \rightarrow M - OH + R - OH$ (2.10)

Water Condensation: $M - OH + HO - M \rightarrow M - O - M + H_2O$ (2.11)

Alcohol Condensation: $M - OR + HO - M \rightarrow M - O - M + R - OH$ (2.12)

where M is a metal, – OR is an alkoxyl group and – OH is hydroxyl group.

Then, the gel is heated at high temperature to obtain the final solid product. The structure and properties of synthesized material with sol-gel method depend on the potential of hydrogen ion (pH), catalyst, temperature, solvent composition and molar ratios of reactants. Therefore, the sol-gel method is used to synthesize material with a variety of shapes such as porous structures, thin fibers, dense powders and thin films. Aerogel are created by the extraction of liquid in wet gel under suitable condition resulting in the pores of solid. After the gel is heated, it will become xerogel and then later dense ceramic. Moreover, the sols can be formed to films, fibers and

uniform powders by coating, spinning and precipitation, respectively. The diagram of sol-gel process of synthesis nanoparticle is shown in Fig. 2.6.

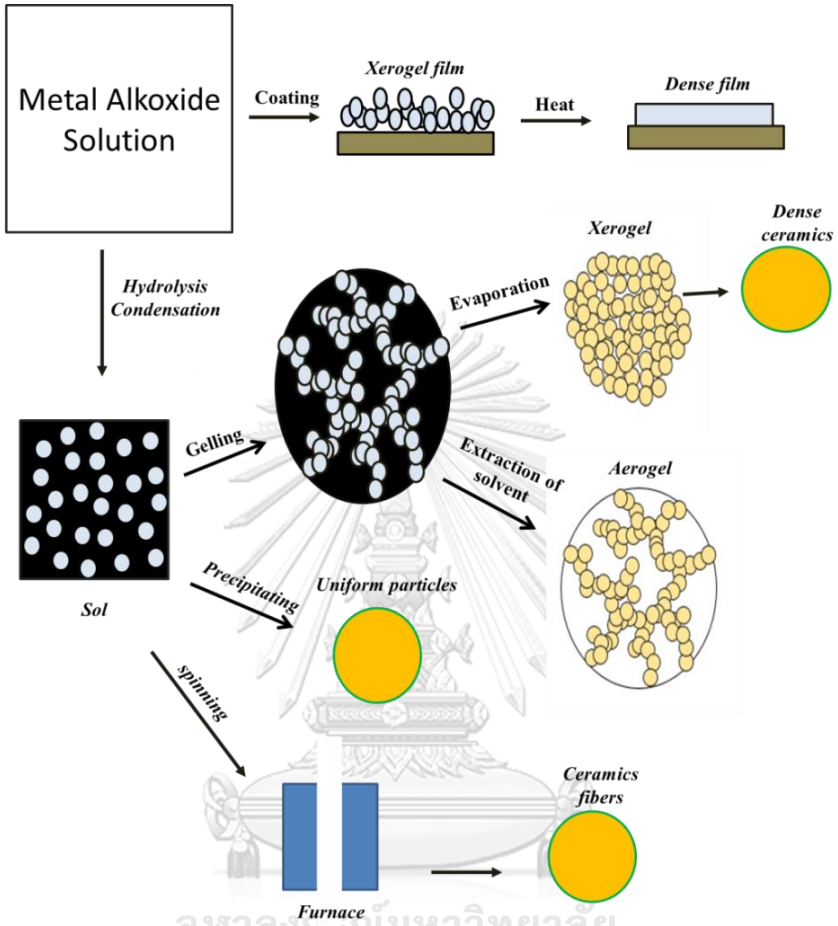

Figure 2.6: Schematic representation of various materials obtained by a sol -gel method.

In this work, the precursor Ni-doped CCTO was deposited on two types of substrates, alumina and silicon, (see details in section 4.3) by a spin coating technique. Spin coating is one of the most common techniques for applying thin films to substrates due to it is able to quickly and easily produce very uniform films, a few thickness film (a few nanometers to a few microns). The thickness of films depends on velocity and time for spinning. The thickness of films decreases with higher spin speeds and longer spin times. The process of spin coating technique can be prepared

by the following steps. Firstly, the substrate was placed on a stage in spin coater. Then, the precursor solution was dropped on substrate. In dropping process, the method to drop the precursor can be done by two ways, namely dropping precursor on substrate before spinning substrate and dropping precursor on substrate and spinning substrate together. If the solution has low viscosity, the precursor are dropped on substrate and spinning substrate together but if the solution has high viscosity, the precursor are dropped on substrate before spinning substrate. In this work, the precursor was dropped while the substrate was spinning on stage of spin coater with speed spinning 4000 rpm and time spinning 40 s. The centrifuged force results spreading of solution cover the substrate. Then, the film was heated in order to dry and extract the excess solvents from them and the film was annealed in further step.

2.4 The mechanisms of metal oxide gas sensor

Nowadays, air pollution has enhanced due to human activity and natural processes. Therefore, a clean air is an importance to our health and the environment. The our nose can detect hundreds of smells but it difficult to detect in case of toxic, combustible and inflammable gases which are low concentration, colorless and odorless. Therefore, the gas sensor has developed to use instead of our nose. The good gas sensor have to present high sensor response, high selectivity and rapid response speed, so the development of performance of gas sensor is also essential for human and environment in recently. Metal oxide is one of materials that have been widely used to apply as gas sensors due to low cost, easy production, compact size and simple measuring electronics [35]. Generally, the metal oxide gas sensor is fabricated as chemical resistance type sensors that their electrical conductivity or resistivity

changes when a target gas interact with their surface. The increase or decrease of electrical properties depends on type of gases. There are two main different models in order to explain the mechanisms of gas sensor response.

2.4.1 Oxygen-vacancy model

Oxygen-vacancy model is used to explain the physical adsorption process in the case of oxygen vacancies on the metal oxide surface. In n-type material, oxygen vacancies on the metal oxide surface consume free electrons. This process increases the resistance in n-type materials due to reducing the mobility of electrons [2]. Then, the n-type materials react with target gases and occurring chemical resistance behavior further.

$$V_O^{\bullet\bullet} + 2e^- + \frac{1}{2}O_2 \leftrightarrow O_{lattice} \qquad (2.13)$$

2.4.2 The oxygen ionosorption mechanism

The chemical adsorption process is described by the oxygen ionosorption mechanism which oxygen is the interaction between oxygen molecules and the metal oxides surface. Oxygen affects highly on the adsorption process at the metal oxides surface due to oxygen is highly able to attract [36], so the adsorbed oxygen is easily created on the surface of metal oxides. As an air in atmosphere is exposed to metal oxide surface, the oxygen molecules are absorbed on that surface. The electrons in conduction band of metal oxide will be attracted to interact with oxygen molecules leading to adsorbed oxygen species (O_2^-, O^-) on the surface [36, 37]. The oxygen species that formed depend on operating temperature in the Equations (2.14)-(2.17). It can be seen that the oxygen absorption increases with increasing the operating

temperature. From equation (2.15), O_2 is able to consume one electron from the metal oxide surface at below the temperature of 200 °C while at above the temperature of 200 °C the acceptation of oxygen (O^-_2) in equations (2.16 and 2.17) is two electrons [38]. Therefore, the numbers of electron are decreased in conduction band leading to increase the resistance as illustrated in Fig. 2.6. Then, electrical properties of sensor will change quickly when the metal oxide is exposed to other gas molecules. The change of the carrier concentration and sensor electrical properties depend on a type of target gases and metal oxide gas based sensor and they will be discussed in section 2.3.2.1 and 2.3.2.2.

$$O_{2\,(gas)} \rightarrow O_{2\,(adsorbed)} \qquad (2.14)$$

$$O_{2\,(adsorbed)} + e^-_{(conduction\ band)} \rightarrow O^-_{2\,(adsorbed)} \quad ; T < 200\ ^oC \qquad (2.15)$$

$$O^-_{2\,(adsorbed)} + e^-_{(conduction\ band)} \rightarrow 2O^-_{(adsorbed)} \quad ; T > 200^oC \qquad (2.16)$$

$$\text{Or} \quad O_{2\,(adsorbed)} + e^-_{(conduction\ band)} \rightarrow 2O^-_{(adsorbed)} \quad ; T > 200^oC \qquad (2.17)$$

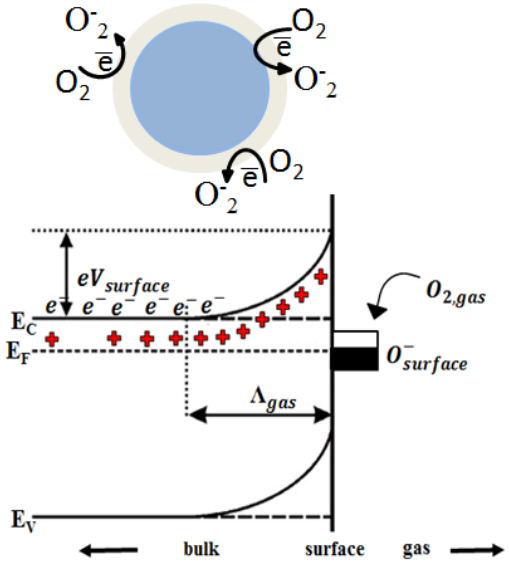

Figure 2.7: The diagram of band bending after chemisorption of oxygen species [38].

2.4.2.1 The n-type metal oxide gas sensor

The electron is majority carriers in n-type metal oxide material. As oxygen molecules are exposed to the sensor surface. The electrons in conduction band interact with oxygen molecules leading to adsorbed oxygen species on the surface. The adsorbed oxygen species affect an increasing resistance of sensor due to a decrease in amount of electron. When reducing gas (such as H_2S, NH_3 [24]) interacts with adsorbed oxygen species on the surface, the occurred chemical reaction produces an increase in amount of electrons at the conduction band. The enhancement of electron leads to an increase in conductivity or a decrease in resistance [38]. The mechanisms of n-type metal oxide material toward reducing gases can be seen in Fig. 2.8. In contrast, the target gas is oxidizing gas (such as NO [24], NO_2 [28]). The charge carriers are reduced leading to a decrease in conductivity.

2.4.2.2 The p-type metal oxide gas sensor

The mechanisms of p-type metal oxide materials toward target gases is different to n-type metal oxide material. The positive charge carriers or holes are the majority carriers in p-type materials. The oxygen molecules are absorbed on the sensor surface. The electrons from valence band are excited to conduction band and these electrons interact with oxygen molecules leading to adsorbed oxygen species on the surface. This process also increases amount of hole at valance band and affect to the reduction in resistance of sensor. Then, target gas (reducing gas) is exposed to the surface sensor and affects to interaction with the absorbed oxygen species on the surface. Therefore, the electrons are released from chemical reaction at the conduction band. The released electrons fall down into the valence band and recombine with the holes or neutralize the holes in the p-type material; thereby the numbers of hole are

decreased. This leads to an increase in resistance of such p-type sensor. The mechanisms of p-type metal oxide material toward reducing gases are presented in Fig. 2.8. In contrast, if target gas is oxidizing gas, the chemical reaction of oxidizing gas increases the hole concentration or decrease the resistance [37, 38].

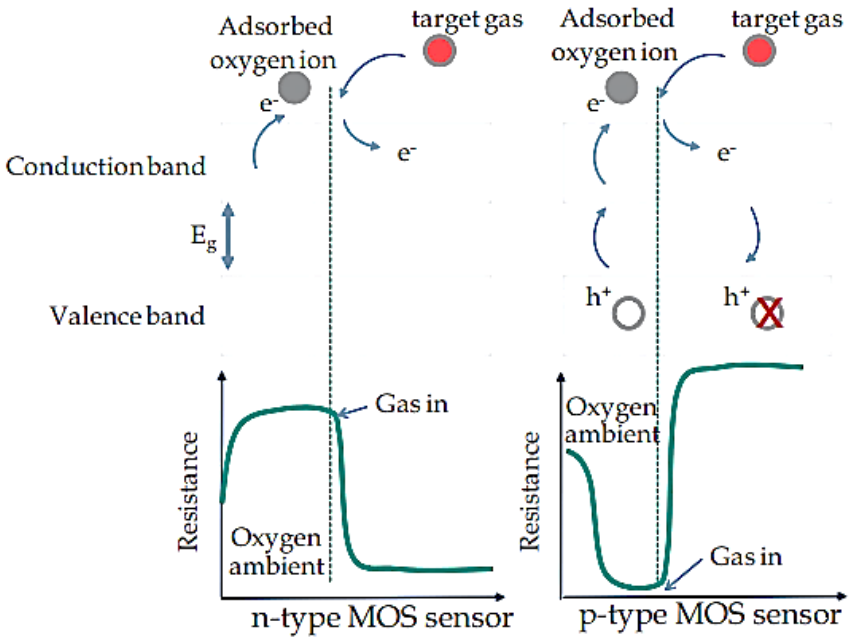

Figure 2.8: Schematic representation of gas mechanism of n-type and p-type metal oxide sensor towards reducing gas [39].

Moreover, a change of resistance under target gases can be calculated as sensor *(R)* of sensor for n- type material [24].

$$S = \frac{R_a}{R_g} \quad \text{for reducing gas} \qquad (2.18)$$

$$S = \frac{R_g}{R_a} \quad \text{for oxidizing gas} \qquad (2.19)$$

where R_a is the resistance of the sensor measured in the dry air atmosphere.

R_g is the resistance of the sensor measured in tested gases.

In case of CCTO, the CCTO sensor will behave n-type or p-type conductivity dependent on the synthesis methods and experimental conditions [8]. In previous research, Parra et al. reported that the CCTO thin film which was prepared by the sol-gel method exhibited n-type semiconducting behavior [7]. Therefore, the mechanism of CCTO can be explained in section 2.3.2. Moreover, many researchers have found that point defects, vacancies and interstitials can affect to gas adsorption and conductivity properties of CCTO. Ponce et al. have reported that the generation of oxygen vacancy in lattice of CCTO structure also affects to conductivity properties of CCTO [39]. An increase in oxygen vacancies in structure increase resistance of CCTO. Moreover, copper ions in CCTO film can interact with H_2S gas by itself and affect to the change of electrical properties as reported in previous work in our laboratory [22].

2.4.2.3 Effect of doping of the metal Oxide sensor

Doping of metal oxide film improve electrical properties of sensor. The dopant is catalytic to increase catalytic activity and modify electrical resistance of the intrinsic metal oxide [36]. As the target gas interacts with metal oxide sensor, the chemical reaction occurs on surface can be describe in the following.

$$A(gas) \underset{k_{-1}}{\overset{k_1}{\Leftrightarrow}} A(adsorbtion) \overset{k_2}{\Leftrightarrow} Products \qquad (2.20)$$

In case of unimolecules, the surface region exposes and absorb target gas that it is called the surface coverage. The surface coverage of A is defined as Θ_A and the rate of adsorption is defined as $\frac{d\Theta_A}{dt}$.

$$\Theta_A = \frac{\text{Number of adsorption sites occupied}}{\text{Number of adsorption sites available}} \quad (2.21)$$

$$\frac{d\Theta_A}{dt} = k_A P_A (1 - \Theta_A) \quad (2.22)$$

where k_A is the rate constant for adsorption and P_A is partial pressure.

Θ_A can be solved from the rate of adsorption and the obtained Θ_A is determined with Langmuir adsorption isotherm form [40].

$$\Theta_A = \frac{k_A P_A}{1 + k_A P_A} \quad (2.23)$$

Therefore, the rate of surface reaction (k_r) of unimolecules is written in the following.

$$k_r = k_2 \Theta_A = \frac{k_2 k_A P_A}{1 + k_A P_A} \quad (2.24)$$

The rate of surface reaction (k_r) is considered in two cases.

1. One case is low pressure ($P_A \to 0$), so Θ_A is small. The rate of surface reaction (k_r) will be written in equation (2.25).

$$k_r = k_2 \Theta_A = k_2 k_A P_A \quad (2.25)$$

2. In case is high pressure ($P_A \to \infty$), so Θ_A is approximately zero. The rate of surface reaction (k_r) will be be written in equation (2.26).

$$k_r = k_2 \quad (2.26)$$

For reaction between different gases types and adsorbed oxygen species, the chemical reaction occurs on surface can be explained in the following.

$$A(\text{adsorbtion}) + O_2^- \xrightarrow{k_2} \text{Products} \qquad (2.27)$$

The rate of surface reaction can be written in the following.

$$k_r = k_2 \Theta_A \Theta_{O_2^-} = k_2 \left(\frac{k_A P_A}{1 + k_A P_A}\right)\left(\frac{k_{O_2^-} P_{O_2^-}}{1 + k_{O_2^-} P_{O_2^-}}\right) \qquad (2.28)$$

$$k_r = (\text{const.}) k_2 \Theta_A \qquad ; \ \Theta_{O_2^-} \text{ is constant} \qquad (2.29)$$

$$k_r = k_{eff} \Theta_A \qquad ; \ k_{eff} \text{ is the effective response rate} \qquad (2.30)$$

$$k_r = k_{eff} \Theta_A \qquad (2.31)$$

It can be seen that Equation (2.31) is linear equation. Therefore, the effective response rate is slope of this equation. The strain line of relation between the effective rate and doping concentration represent the first reaction order on catalyst in chemical kinetic sense.

CHAPTER III

CHARACTERIZATION TECHNIQUES

In this chapter explains the basic principles of the characterization techniques which consist of X-ray diffractometer (XRD), Field emission scanning electron microscopy (FESEM), Energy dispersive X-ray spectroscopy (EDX), X-ray photo emission spectroscopy (XPS) and Raman spectroscopy. The crystal structures and phase compositions of undoped and Ni-doped CCTO films were examined by XRD while vibrational, rotational, and other low-frequency modes in the films were characterized by Raman spectroscopy. The surface morphologies and thicknesses of the films were analyzed by FE-SEM. Moreover, the chemical compositions in the films and the oxidation state of each element were examined by energy dispersive X-ray spectroscopy (EDX) and X-ray photo emission spectroscopy, respectively.

3.1 X-ray diffraction technique

X-ray diffraction technique is used to characterize the crystal structure, phase composition, cell parameter, and particle size of materials. These characterizations do not damage the surface of material and X-ray diffraction technique can characterize different types of sample such as thin films, powders, ceramics, thick films, and etc. Crystal structure of material consists of plane of regular arrays atoms. X-rays in the wavelength range of 10^{-8} - 10^{-10} m are in similar order to the spacing *d* between planes in the crystal, so they could be used to produce the diffraction pattern. Generation and type of X-rays is explained in section 3.1.2.

3.1.1 Generation and types of X-rays radiation

X-rays were discovered by Willhelm Conrad Poentgen who was a German physicist. The diagram in Fig. 3.3 shows a common X-ray tube. It is composed of a vacuum tube, a cathode (filament) which mostly is produced by tungsten, a high voltage and an anode (target). When anode and cathode are operated at high voltage, tungsten is heated by the electrical current which flows through in cathode. If high voltage is sufficient, electrons flow from the cathode to anode with very high velocity. When an incoming electron hits the atom of target which generally are made of copper or molybdenum, many interactions occur. If that incoming electron has kinetic energy more than the binding energy of the inner electron in the atom of metal target, it can kick out the inner electron to remove it from the atom. These processes leave a hole or electron vacancy in the atom target, and an electron from the higher energy level moves down to fill the vacancy causing characteristic X-ray radiation. For material characterizations in the thesis, the characteristic X-ray is used via X-ray diffraction technique. The details of characteristic X-ray are explained in section 3.1.1.1 – 3.1.1.2.

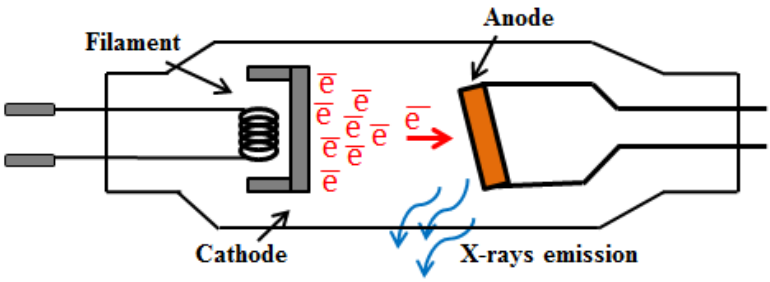

Figure 3.3: X-rays tube.

3.1.1.1 Continuous X-rays or Bremsstrahlung

As the high energy electron moves closely the nucleus of a heavy metal. The velocity of electron is decelerated suddenly as shown in Fig. 3.4. This process produces a range of X-ray radiations which are continuous X-rays or it is called Bremsstrahlung radiation. The wavelength of continuous X-rays is in the range of 0.1 – 100 Å and the intensity of X-ray increases with increasing atomic number of target.

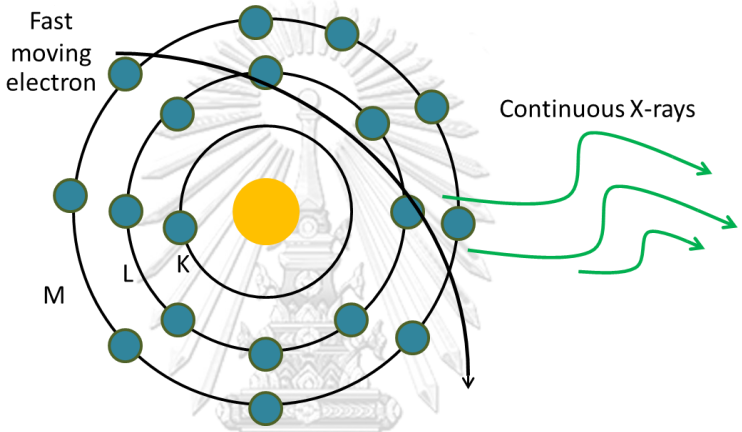

Figure 3.4: Generation of continuous x-rays.

3.1.1.2 Characteristic X-rays

As the metal target is bombarded with electrons, an electron from the inner shells of the atoms of the metal target can be dislodged by the incident electron. The electron in higher energy level substitute at position of scattered electron in atom of target. Characteristic x-rays are emitted due to transitions energy levels of electron. Characteristic x-rays are specific energy depending on used element as target and electron shell in the atoms of the metal target. Fig. 3.6 presents the inner shell of electron in atom that is composed of *K*-shell, *L*-shell and *M*-shell, respectively. If an electron in *K*-shell is scattered from the atom, the electron in another shell from higher level fill in the vacancy. An electron from *L*-shell to *K*-shell produces K_α X-

ray. In contrast, the transition of an electron from *M*-shell to *K*-shell produces K_β X-ray as shown in Fig. 3.5. Similarly, the transition of an electron from *M*-shell to *L*-shell produces L_α X-ray. The transition of an electron from *N*-shell to *L*-shell produces L_β X-ray [40], etc. Fig. 3.6 shows the difference between the intensity versus wavelength of characteristic X-rays and continuous X-rays that the characteristic X-rays are sharp peak.

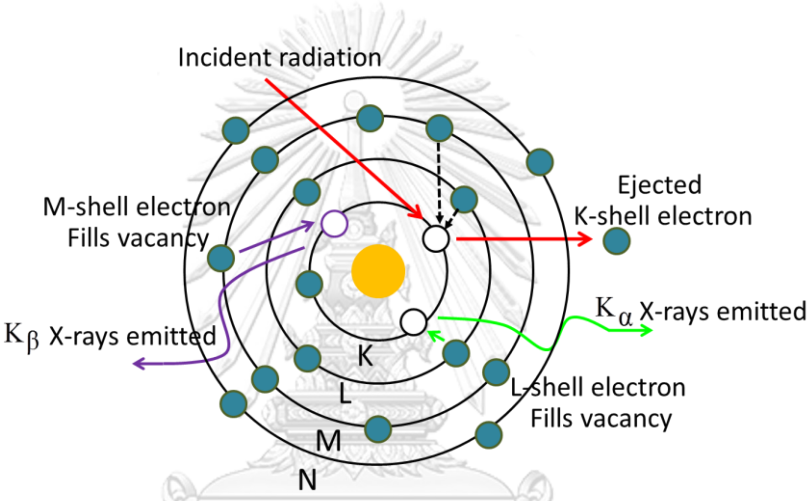

Figure 3.5: Generation of Characteristic x-rays.

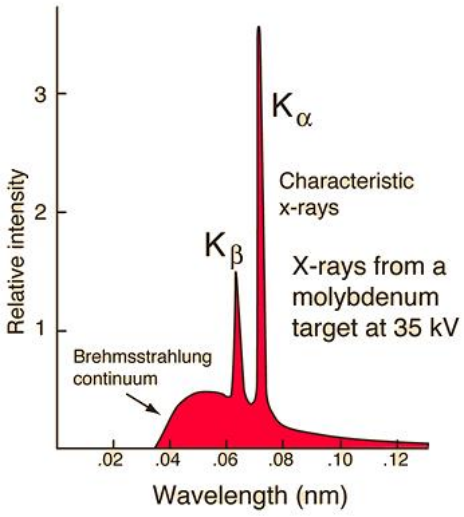

Figure 3.6: Characteristic X-rays and continuous X-rays intensities vs. wavelength [41].

3.1.2 Bragg's law

In this thesis work, the characteristic X-rays is used in X-ray diffraction technique that copper is target of generation X - rays. X-ray diffraction in crystal can be described by Bragg's law [41]. As the incident beam of characteristic X-rays hits atom plane in crystal, X - rays is reflected from crystal plane. The scattering between planes of atoms is shown in Fig. 3.7.

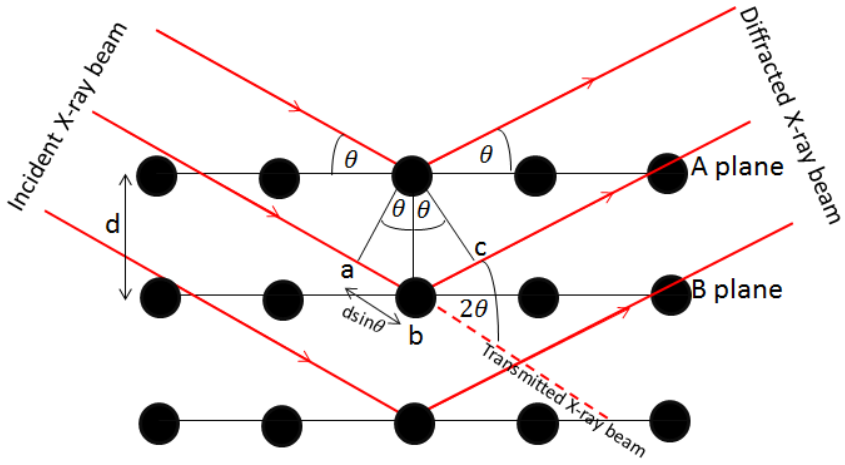

Figure 3.7: X-ray diffraction in crystal.

In Fig. 3.7, the path difference of the closely atomic planes can be written as following.

$$ab + bc = d\sin\theta + d\sin\theta = 2d\sin\theta \qquad (3.3)$$

The path difference between the closely atomic planes is related to constructive interference of X-ray as shown below.

$$2d\sin\theta = n\lambda \quad \text{(Bragg's law)} \qquad (3.4)$$

where d is the spacing between planes.

θ is angle of incident X-ray beam.

λ is wavelength of X-ray beam.

n is integer number.

In addition, position of diffraction peak associate plane of regular arrays atoms that Miller indices (hkl) are used to identify atomic plane. Each crystal produces a unique diffraction pattern that is a fingerprint of material, so diffraction pattern is used to identify crystal structure type and phase composition. Then, Bragg 's law equation can be calculated to obtain the spacing d between planes in the crystal that the spacing *d* relate to lattice parameters and plane of diffraction (hkl). For example,

Table 3.2: The relation between the spacing *d*, lattice parameter and plane of diffraction with different crystal structure types [42].

crystal structure	Relation of the spacing *d*, lattice parameter and plane of diffraction
Cubic	$\frac{1}{d^2}=\frac{h^2+k^2+l^2}{a^2}$
Tetragonal	$\frac{1}{d^2}=\frac{h^2+k^2}{a^2}+\frac{l^2}{c^2}$
Orthorhombic	$\frac{1}{d^2}=\frac{h^2}{a^2}+\frac{k^2}{b^2}+\frac{l^2}{c^2}$
Hexagonal	$\frac{1}{d^2}=\frac{4}{3}(\frac{h^2+hk+k^2}{a^2})+\frac{l^2}{c^2}$
Monoclinic	$\frac{1}{d^2}=\frac{1}{\sin^2\beta}(\frac{h^2}{a^2}+\frac{k^2\sin^2\beta}{b^2}+\frac{l^2}{c^2}-\frac{2hl\cos\beta}{ac})$

3.2 Field emission scanning electron microscopy

The principle of field emission scanning electron microscope (FESEM) and scanning electron microscope (SEM) techniques are similar but they differ in the emitter type and the resolution. FESEM technique achieves better lateral spatial resolution providing higher magnifications compared with SEM technique. FESEM could characterize a point resolution of 0.8-1.5 nm while a point resolution characterization of SEM is 3-3.5 nm. Even the Resolution at low accelerating voltages of FESEM is much better. Moreover, thermionic emitters are used in SEM. In thermionic emitters, a filament is heated by electrical current. The electron can dislodge from a filament material when the heated is higher more than the work function of the filament material. However, there are many disadvantages of thermionic sources such as relative low brightness, evaporation of cathode material and thermal drift during operation. These problems can be avoided when field emission is used (or it is also called cold cathode field emitter) in FESEM. The filament mainly used is a metal with high melting point such as tungsten which has a tip with radius about 100 nm. The filament is placed in a large electrical potential gradient without heating. The high sufficient electric field affects the electron emission from tip at anode. The generating electron of FESEM can produce a cleaner image, less electrostatic distortions and spatial resolution 0.8-1.5 nm that are better than SEM. Main components of FESEM are electron source (electron gun), electrostatic lenses, electromagnetic lenses, sample state, detector and data output device as shown in Fig. 3.8. In this thesis, the surface morphology and the thickness of resulting films were characterized by (FESEM).

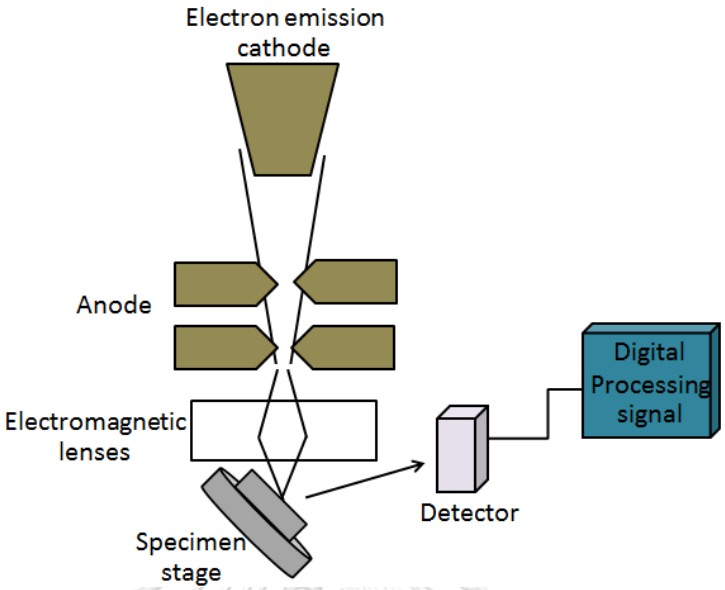

Figure 3.8: Diagram of field emission scanning electron microscopy.

The generating electron of FESEM is produced at the cold cathode field emitter. Electrostatic lenses affect escaped electron as the electron beam and the electron beam is accelerated to electromagnetic lenses. The electron beam is focused to sample by the electromagnetic lenses. The surface of sample is bombarded with the incident electrons. This leads to the interaction between incident electron beam and sample. A variety of signals are detected and presented with data output device. The sample image can be produced with secondary electrons (SE) and backscattered electrons (BSE). Secondary electrons are produced when the electron beam hits an electron in the sample and the energy transfers from the electron beam to the atoms in the sample. As electrons in the sample obtain enough energy, they strike the sample. These electrons are called secondary electrons that these signals are produced as morphology and topography surface image. However, backscattered electrons are the incident electron beam which comes close to the nucleus and they are scattered after

they loses some energy to electron in the sample. Backscattered electrons can be used to generate an image in the microscope that shows the contrasts in composition in multiphase samples. Moreover, the interaction of incident electron beam and sample can generate other signals such as diffracted backscattered electrons (EBSD) that are used to determine crystal structures and orientations of minerals, photon that are used for elemental analysis and continuum X-rays, auger electron and heat. A variety of signals from interaction between incident electron beam and sample is illustrated in Fig. 3.9.

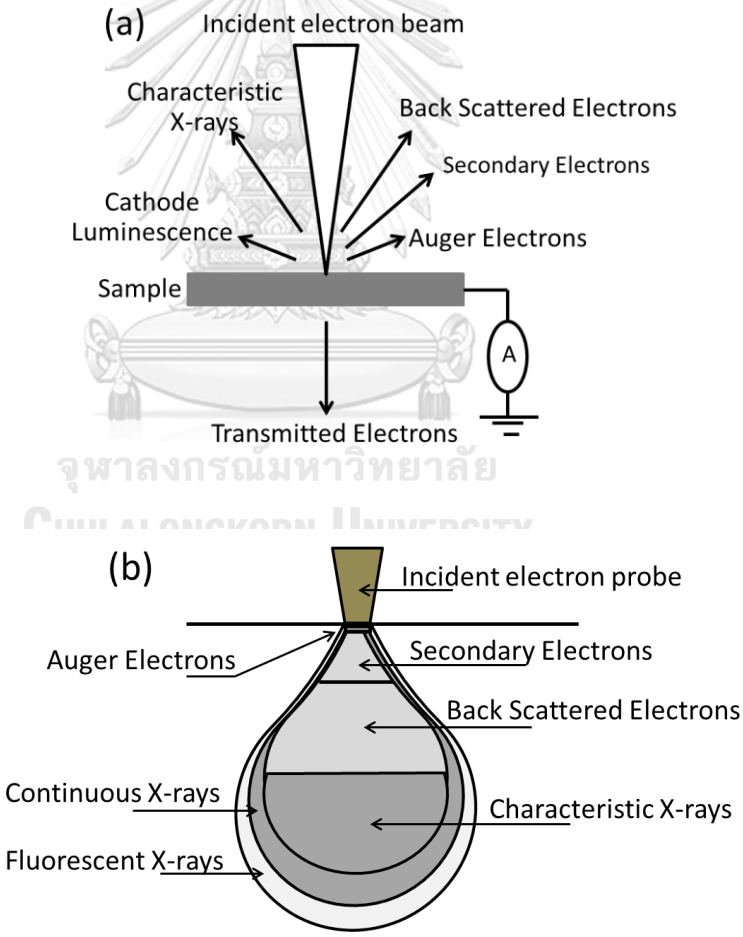

Figure 3.9: (a) Type of signals and (b) volume within a sample of interactions between electrons and a sample.

3.3 Energy dispersive X-ray spectroscopy

Energy dispersive X-ray spectroscopy (EDS or EDX) is one of the analytical technique used for the elemental analysis or chemical characterization materials. Most of the time EDX equipment is attached to FESEM equipment. In this case, electrons in the atoms comprising the surface of sample are excited with energy from bombardment of the electron beam until they are ejected from the surface of sample. This process leads to an inner-shell vacancy of an atom and then an electron transfers from outer shell to inner shell to fill the vacancy. Emitted X-rays is produced with some fixed wavelengths for each element. Each element has a unique atomic structure allowing a unique set of X-ray emission peaks. Thus, the detector can detect the intensity for each wavelength and then used that information to characterize the elemental composition of material.

3.4 X-ray photoelectron spectroscopy

X-ray photoelectron spectroscopy (XPS) is also known as Electron Spectroscopy for Chemical Analysis (ESCA). XPS is a surface analysis technique that is used for investigating the elemental composition, empirical formula, chemical state and electronic state of the elements from the surface of the material. The depth of analysis for an XPS measurement is from the top of the surface to ~10 nm from the surface. These characterizations can be done by using photoelectric phenomenon [43]. As x-ray photon bombards the atom in sample and the energy (E) of incident photon is in equation (3.6).

$$E = h\nu \qquad (3.6)$$

where h is Planck constant of 6.623×10^{-23} J·s

ν is frequency of x-ray photon

The atoms in the sample absorb energy from x-ray photon. Here in the thesis study, a mono-energetic Al K_α x-rays is used to excite the sample. After electrons absorb energy from x-ray photon, some again energy more than their work function of atom in sample, so they are excited and escape the atom of material. These ejected electrons are called photoelectron carrying their kinetic energies as shown in Fig. 3.10 (a). These photoelectrons originate from a depth of <10 nm. The relation between the binding energy (BE) and kinetic energy can be calculated as follows.

$$BE = h\nu - KE \qquad (3.7)$$

Then, the kinetic energy (*KE*) of the electron depends on the x-ray photon energy ($h\nu$) and the binding energy (*BE*) of the electron in material. The energy of the emitted photoelectrons from the sample are detected by an electron energy analyzer. The kinetic energies and the numbers of emitted photoelectrons are recorded as presented in Fig. 3.10 (b). The binding energy, intensity of a photoelectron peak with precise position in XPS spectra, and peak shape are analyzed to identify and determine the characterization of elemental, the concentrations, and chemical state for the elements.

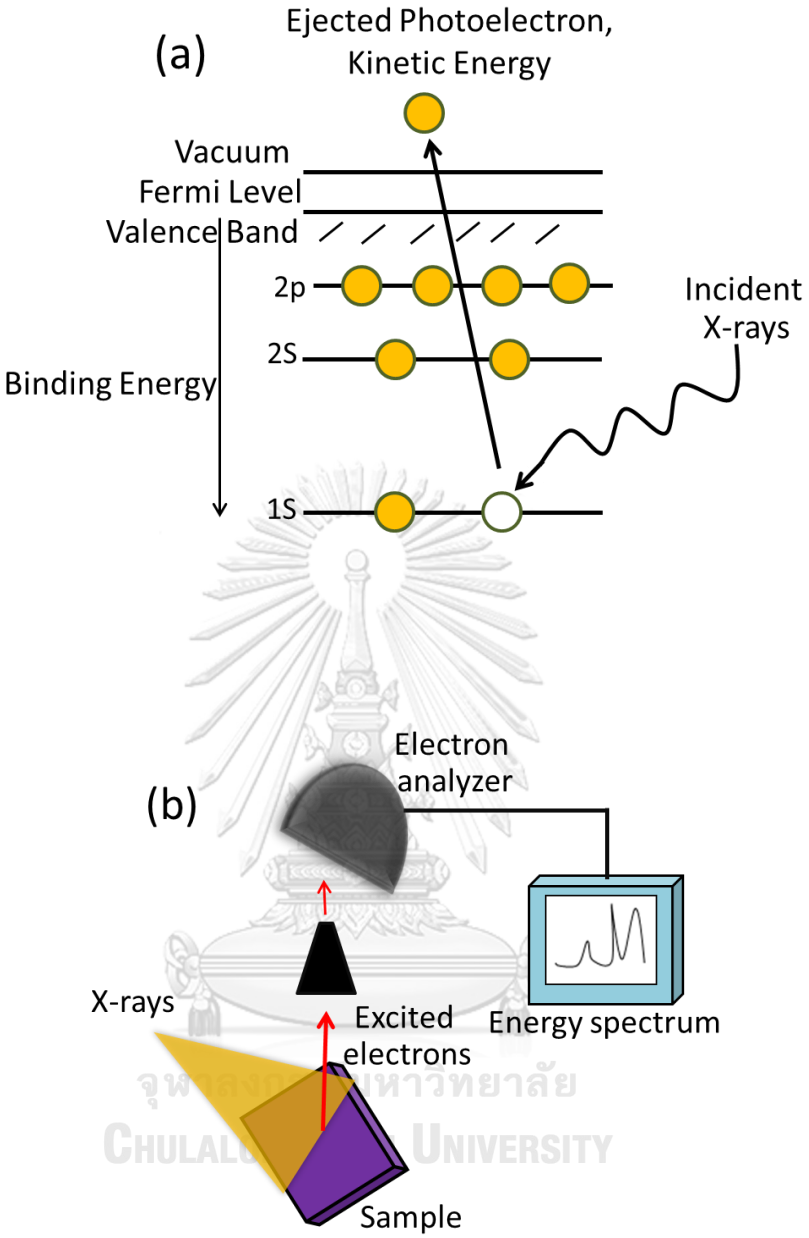

Figure 3.10: (a) Generation of photoelectron and (b) diagram of XPS.

3.5 Raman spectroscopy

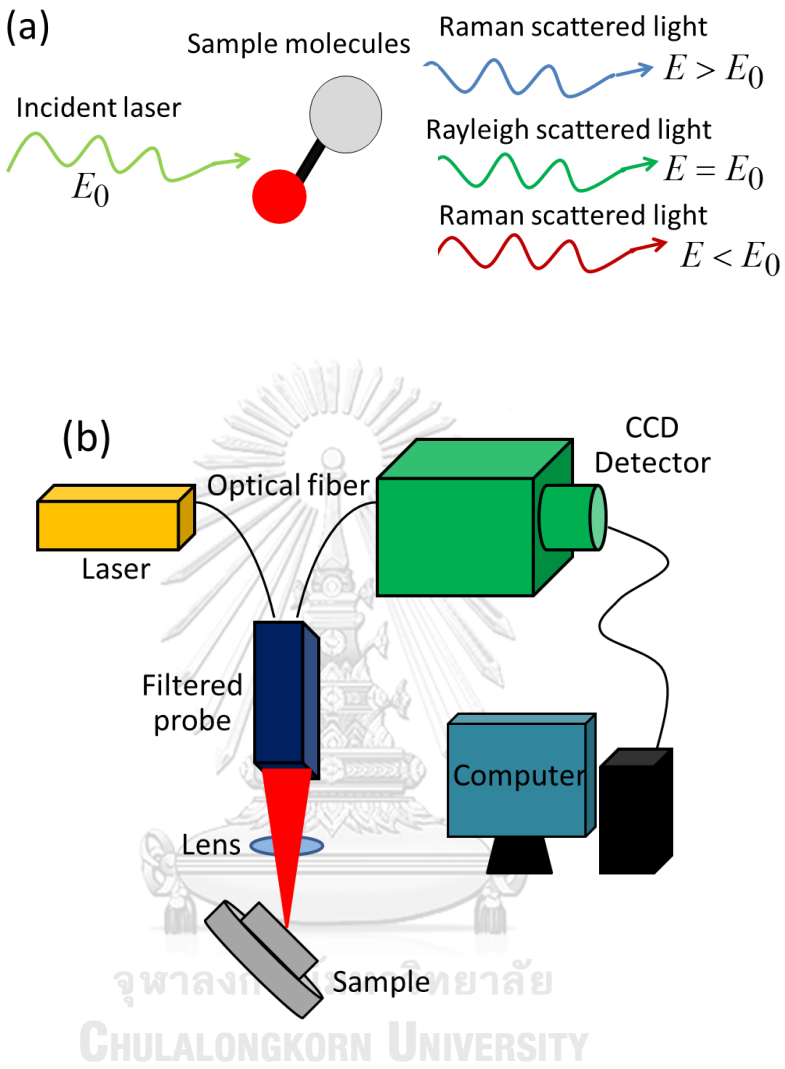

Figure 3.11: (a) Types of scattering between laser light and molecules and (b) diagram of Raman spectroscopy.

Raman spectroscopy technique is used to examine information on molecular vibrations and crystal structures. Each vibrational energy level corresponds to unique molecule and the ejected photons have unique wavelength shifts. Vibrational spectroscopy is used to identify molecules in a sample. As laser light which is monochromatic light hits molecules in the sample, the interaction between light and molecules in sample are occurred in the sample. They consist of reflecting, absorbing,

transmitting or scattering. In case of scattered light, there are 2 types of scattering as shown in Fig. 3.11 (a). Elastic process (Rayleigh scattering, $E = E_0$) is one of the scattering that does not lose energy. The scattered light has energy similar to incident laser light. Moreover, one of the scattering is an inelastic process that transfers energy between light and molecular vibrations in sample. The wavelength of the scattered light is changed. The changed wavelength of the scattered light is also called that Raman scattering ($E > E_0$ or $E < E_0$). The energy of scattered light depends on the vibrational state of the molecule. When the scattered light has energy less than incident laser light, then it is called Stokes Raman scattering. In other hand, if the scattered light has energy more than incident laser light then it is called anti-Stokes Raman scattering. The wavelengths of these Raman scattering are detected by using a CCD camera and it is shown as Raman spectrum. The Raman spectrum provides the chemical composition and structural information. The diagram of Raman spectroscopy is illustrated in Fig. 3.11 (b)

CHAPTER IV

EXPERIMENTAL METHODS

In this chapter the synthesis of undoped and Ni-doped $CaCu_3Ti_4O_{12}$ (CCTO) thin films with using nickel oxide (NiO) and nickel (II) acetate by a sol-gel method is explained. In terms of characterizations, the undoped and Ni-doped CCTO were analyzed with X-ray diffraction technic (XRD), field emission scanning electron microscope (FE-SEM), Energy dispersive x-ray spectroscopy (EDX), Raman spectroscopy and X-ray photo emission spectroscopy (XPS). The photo-lithography process and the gas sensing measurement is also described.

4.1 Synthesis undoped and Ni-doped $CaCu_3Ti_4O_{12}$ solution with using NiO

The undoped and Ni-doped $CaCu_3Ti_4O_{12}$ (CCTO) thin films were synthesized by a sol-gel method using acetic acid as dissolution. Calcium acetate hydrate ($Ca(C_2H_3O_2)_2 \cdot xH_2O$, Sigma, 99%), copper (II) acetatemonohydrate ($Cu(II)(C_2H_3O_2) \cdot H_2O$, Fluka, 99%), titanium (IV) isopropoxide ($Ti(OCH(CH_3)_2)_4$, Sigma, 97%), and nikel oxide (NiO, Company) were used as starting materials. Ni doping concentrations were doped with 0, 1, 4, and 7 wt% (0, 16.3, 45.6 and 76.0 mol%) into the precursors. For preparing Ni doping precursor, the calculated NiO (0.0598 g) was dissolved with 25 g of acetic acid at 120 °C until it was completed dissolved. After that 0.855g of $Ca(C_2H_3O_2)_2$ and 2.943 g of $Cu(CO_2CH_3)_2$ were added into NiO solution, and the mixture was placed on the plate of a magnetic stirrer for 24 hr at room temperature. The amount of $Ti(OCH(CH_3)_2)_4$ has to be controlled by decreasing the starting amount for more Ni-doping concentrations as shown in Table

4.1. Ethylene glycol (3 mL) and formamide (3 mL) were added together into each mixture and the solution was placed on a hot plate at 120 °C for 3-5 hr until homogeneous solution was obtained. For undoped CCTO precursor could be prepared similarly to above descriptions without adding NiO into the precursor by adding 6.130 g of $Ti(OCH(CH_3)_2)_4$ instead. Moreover, the 7 wt% Ni-doped CCTO solution is maximum that can be achieved. If Ni-doping concentration is more than 7 wt%, NiO is not completely dissolved. The process of synthesis Ni-doped $CaCu_3Ti_4O_{12}$ solution can be seen in Fig. 4.1.

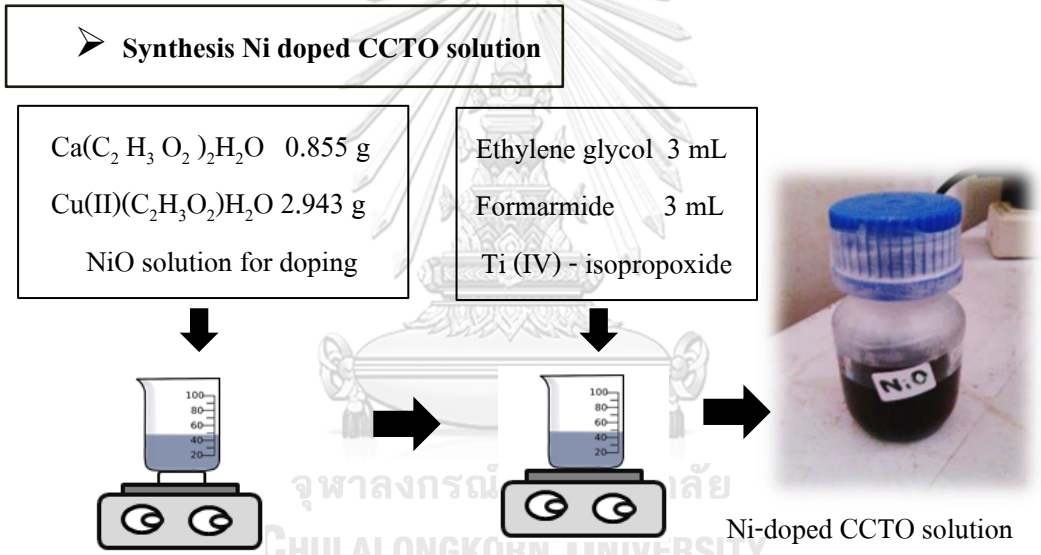

Figure 4.1: Diagram of undoped and Ni-doped CCTO solution synthesis.

Table 4.1: Ni-doping concentrations (wt%) including the weights of nickel oxide (NiO) and titanium IV isopropoxide needed to dissolved in 25 g of acetic acid.

Ni-doping concentrations (wt%)	Weights (g) of NiO in 25 g of acetic acid	Titanium IV isopropoxide (g)
undoped	0	6.1300
1	0.0598	6.0687

Ni-doping concentrations (wt%)	Weights (g) of NiO in 25 g of acetic acid	Titanium IV isopropoxide (g)
4	0.1795	5.9460
7	0.2992	5.8235

4.2 Synthesis undoped and Ni-doped $CaCu_3Ti_4O_{12}$ films with using Nickel (II) acetate

The undoped and Ni-doped $CaCu_3Ti_4O_{12}$ films prepared by nickel (II) acetate can be done with similar process to Ni-doped CCTO films prepared by NiO as described in section 4.1. However, the difference is the amount of Nickel (II) acetate used in the experiment. The calculated weight presents of Ni-doping concentrations including the amounts of Nickel (II) acetate and titanium IV isopropoxide in grams are shown in Table 4.2.

Table 4.2: Ni-doping concentrations (wt%) including the weights of nickel (II) acetate and titanium IV isopropoxide needed to dissolved in 25 g of acetic acid.

Ni-doping concentrations (wt%)	Weights (g) of nickel (II) acetate in 25 g of acetic acid	Titanium IV isopropoxide (g)
0	undoped	6.1300
1	0.0598	6.0687
2	0.1795	5.9460
3	0.2992	5.8235
4	0.4188	5.7009
5	0.5385	5.5783

4.3 Spin coating technique

The undoped and Ni-doped CCTO films were deposited on two types of substrates which are alumina and silicon substrates. Silicon and alumina were used as a substrate for different proposes. For gas sensor fabrications, a set of films was cast on alumina while for some material characterizations, a set of films was cast on silicon substrates. This could be because alumina substrate has oxygen atoms in it, and that could interfere with the interpretation in some of the characterizations. Alumina substrates used in this thesis are made from alumina powders that were compact to be dense substrates with the thickness of ~ 0.5 mm. As know alumina substrates are good insulator and good thermal conductivity, they normally are used to fabricate as substrates for gas sensors. Moreover, they are low cost and can be purchased easily from many companies.

Alumina and silicon substrates were cut into small pieces approximately 2.5x2.5 and 1x1 cm^2, respectively. They were cleaned in acetone and isopropanol bottles with the help of an ultrasonic cleaner device. Each condition of CCTO precursors was coated on the cleaned substrate with the spinning speed of 1500 rpm for 40 s using a spin coater (model P6700 series) as shown in Fig. 4.2. Then, the films were preheated at 120 °C for 20 min on a hot plate in order to dry the gel and remove remaining organic compounds, and the films were annealed at 800 °C for 1 hr in air atmosphere in the convection oven for each layer. This whole process one-layered film was obtained while the thickness of films was controlled by the number of the depositing film layer. Thus, this thesis work I repeated 4 times to obtain four-layered films.

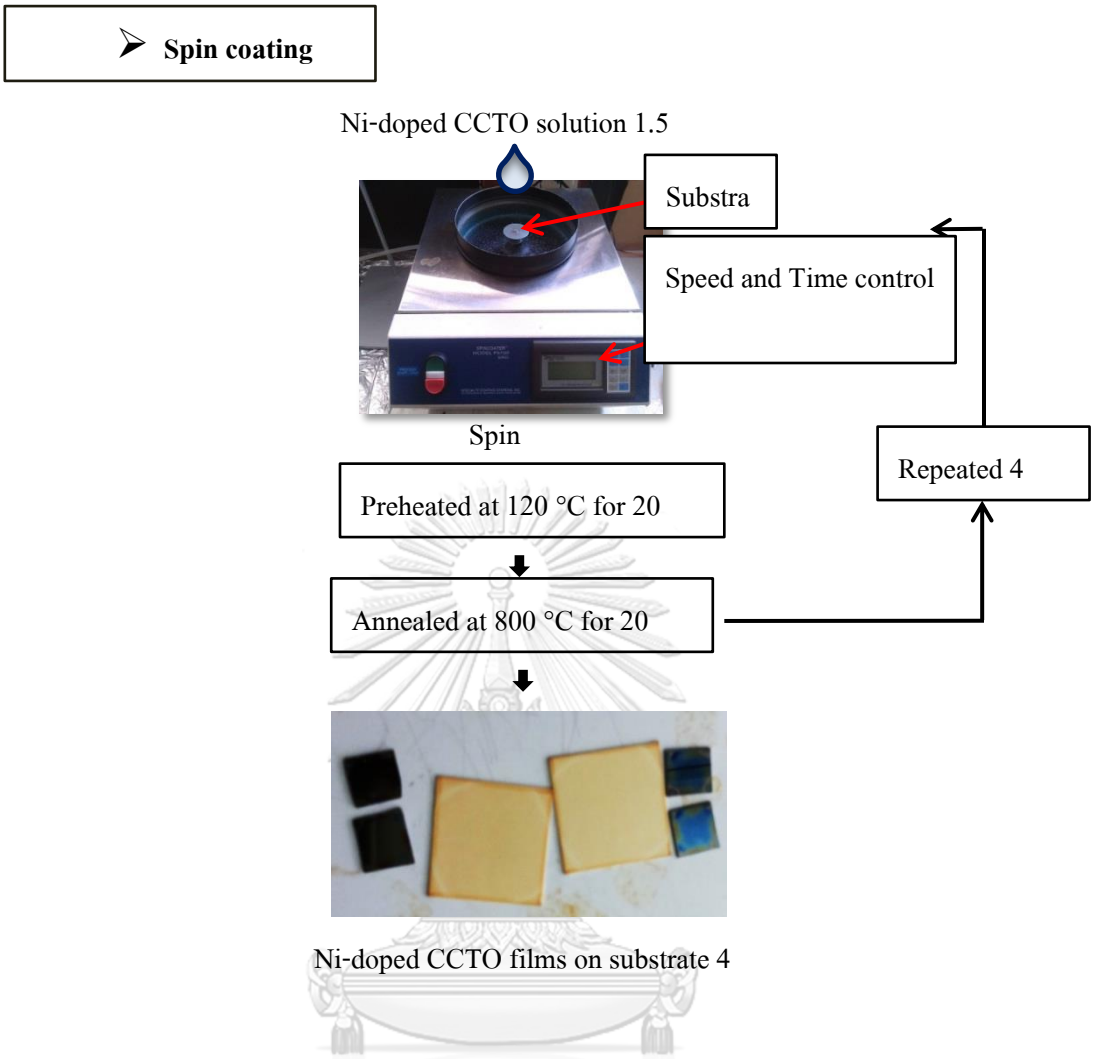

Figure 4.2: Diagram of synthesis undoped and Ni-doped CCTO thin films.

4.4 Characterization of films

4.4.1 Crystal structure and phase composition of the CCTO thin films

The crystal structure and phase composition of the CCTO thin films deposited on two types of substrates, silicon and alumina substrates were examined by X-ray diffraction technique (BRUKER model D8-Discover) (see Fig. 4.3) at Scientific and Technological Research Equipment Centre Chulalongkorn University (STREC). The target of X-ray source is made of copper the wavelength of X-ray used in this thesis work is Cuk_{α} (λ = 1.5406 Å) radiation with 40 KV and 40 mA. The X-ray data was collected in the 2θ range of 20°- 80º with scan step about 0.02 º.

Figure 4.3: The D8-Discover X-ray diffractometer [44].

4.4.2 The surface morphology and thickness of the CCTO thin films

Field emission scanning electron microscope (FESEM) was used to characterize the surface morphology and thickness of CCTO thin films. FESEM equipment used in this study is located at Thai Microelectronics Center (TMEC), Mueang Chachoengsao District. Here in this equipment tungsten is used as the

electron source. The voltage used to accelerate electrons to generate electron beam was 40 KV and the induced current was 40 mA. After the films were placed on a stub with carbon tapes, the surface of CCTO films were coated with gold by sputtering technique to avoid electron charging effect on the film surface. Moreover, the film thicknesses were approximately determined from the film cross sections.

4.4.3 The chemical composition of the CCTO thin films

The energy dispersive X-ray spectroscopy was used to investigate the elemental composition of the CCTO films on silicon substrate. This characterization can be done by energy dispersive x-ray spectroscopy detector used in conjunction with Field emission scanning electron microscope (HITACHI SU8030) (see Fig 4.4) located at National Nanotechnology Center. The elemental composition of the CCTO films was analyzed at 10 KV energy.

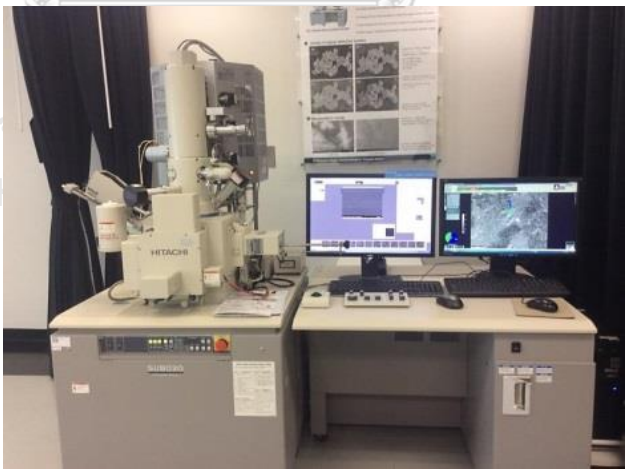

Figure 4.4: Energy dispersive x-ray spectroscopy detector used in conjunction with Field emission scanning electron microscope (HITACHI SU8030).

4.4.4 The chemical state of Ni-doped CCTO thin films

X-ray photo emission spectroscopy (XPS: AXIS Ultra DL) was used to examine the chemical state of Ni-doped CCTO thin films on silicon substrate with using mono-energetic Al K_α x-rays radiation. X-ray photoelectron (XPS) machine can be seen in Fig 4.5. The chemical state of Ni-doped CCTO thin films were characterized at Thailand Center of Excellence in Physics and Petroleum and Petrochemical College (PPC) Chulalongkorn University. The 3 wt% and 7 wt % Ni-doped CCTO with using NiO and 5wt % Ni-doped CCTO with using nickel (II) acetate were examined by X-ray photo emission spectroscopy at Thailand Center of Excellence in Physics but the XPS spectra signal of 3 wt% and 7 wt % Ni-doped CCTO with using NiO isn't clear. Therefore, the samples were analyzed again to confirm chemical state of Ni-doped CCTO thin films by -ray photo emission spectroscopy at Physics and Petroleum and Petrochemical College (PPC) Chulalongkorn University.

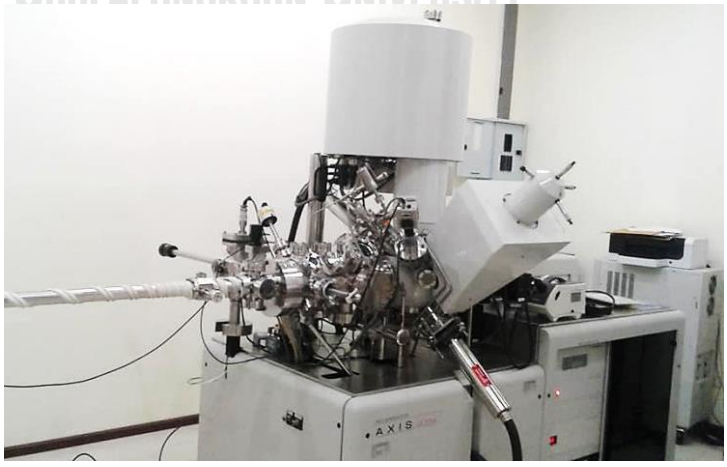

Figure 4.5: X-ray photoelectron (XPS) measurement**.**

4.4.5 Vibrational, rotational, and other low-frequency modes of the CCTO thin films

Vibrational, rotational, and other low-frequency modes of undoped and Ni-doped CCTO thin films deposited on silicon substrate were characterized by Raman spectrometer (RENISHAW Qontor) at Thailand National Nanotechnology Center as shown in Fig. 4.6. The obtained Raman shifts were examined with a laser source (λ = 532 nm) in the frequencies of the Raman shift range of 100-1000 cm^{-1}.

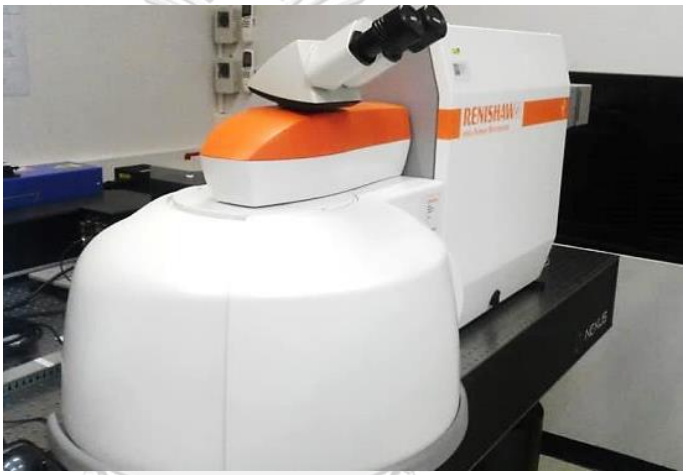

Figure 4.6: Raman spectrometer (RENISHAW Qontor).

4.5 Gas sensing measurements

4.5.1 Fabrication as gas sensor

The four-layers films on alumina substrates were patterned with Au/Cr electrode to apply as gas sensor devices by photolithography process. In this work, we used positive photoresist as connection between films and Au/Cr electrode. When this photoresist is exposed with the UV light, it changes the chemical structure of the

photoresist so that it becomes more soluble in the developer. The unexposed portion of the positive photoresist remains insoluble to the photoresist developer.

Firstly, the undoped and Ni-doped CCTO films on alumina substrate were coated with positive photoresist (S1805) by spin coating technique with the spinning speed of 3000 rpm for 90 s as seen in Fig. 4.7. Then, the photoresist was baked at 115 °C for 60 s on a hot plate in order to hardening the resist. The coated films with photoresist were exposed with the UV light for 35 s after the mask was place above the film as seen in Fig. 4.8. The exposed films were removed with developer before it was baked to dry at 115 °C for 60 s. Then, all films were coated with a thin layer (50 nm) of Cr electrode and followed by a thicker layer (300 nm) Au electrode by sputtering technique, and the coated films were clean again by acetone in ultrasonic. The acetone treatment in ultrasonic affected the removed Cr/Au electrode on film surface but the electrode on photoresist remained on film surface as shown in Fig. 4.9. Then, the cleaned films were beaked at 400 ºC to remove remaining organic compounds on film surface. Then, they were cut to small individual sensor devices as shown in Fig. 4.10 and the area of sensor is 2 x 3 mm^2 and the area of gab film is 100 μm.

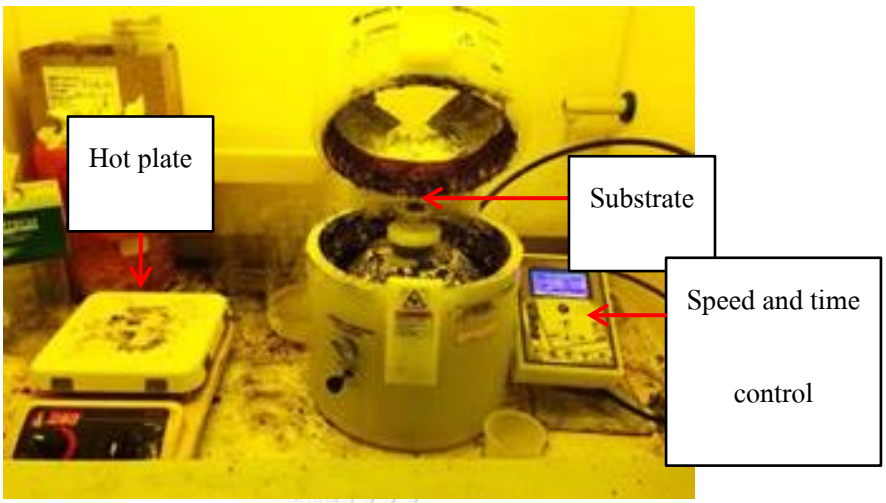

Figure 4.7: Spin coating photoresist.

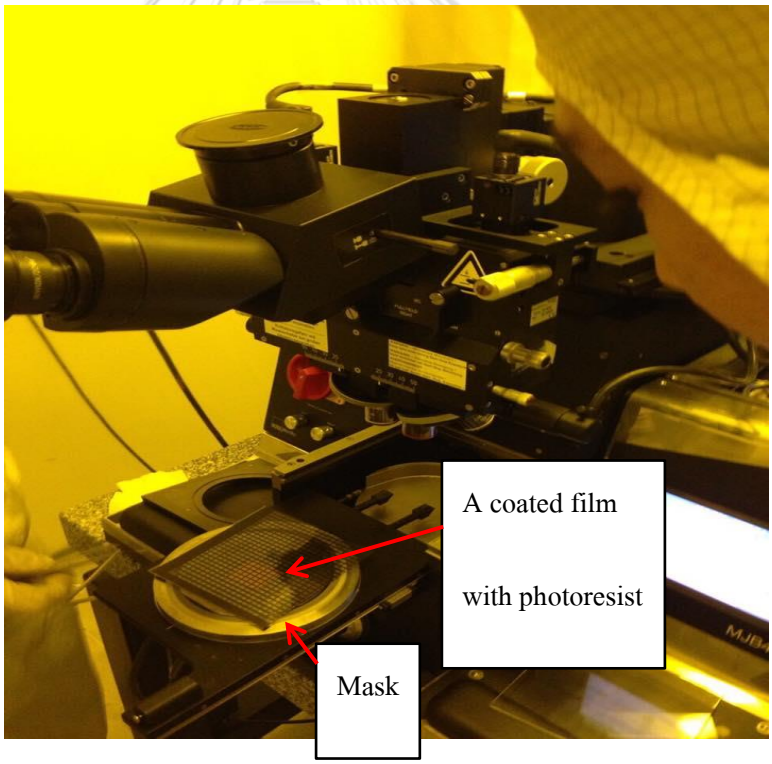

Figure 4.8: Exposure to the UV light using a mask aligner.

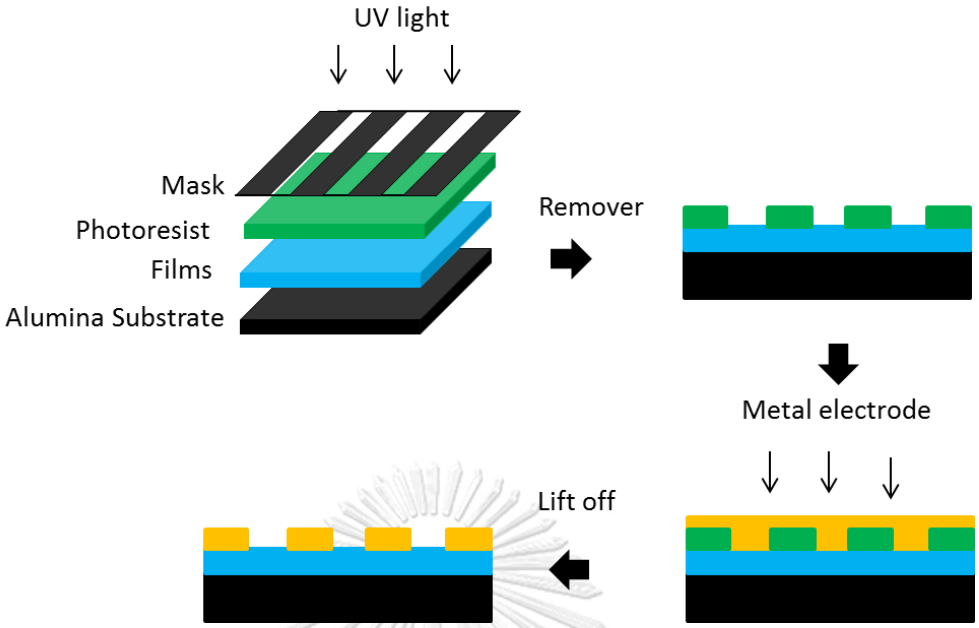

Figure 4.9: The diagram of photolithography.

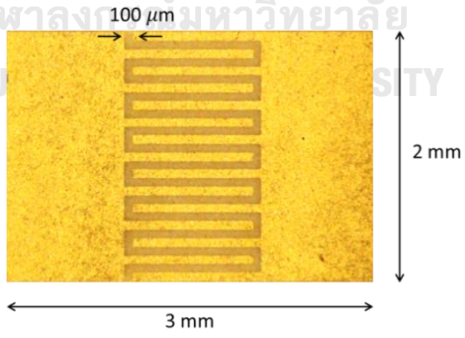

Figure 4.10: Gas sensor device.

4.5.2 Gas sensing properties measurements

Study the gas sensing properties of undoped and Ni-doped CCTO sensors were characterized at Thailand National Nanotechnology Center and the measurement machine of gas sensing properties is presented in Fig. 4.11.

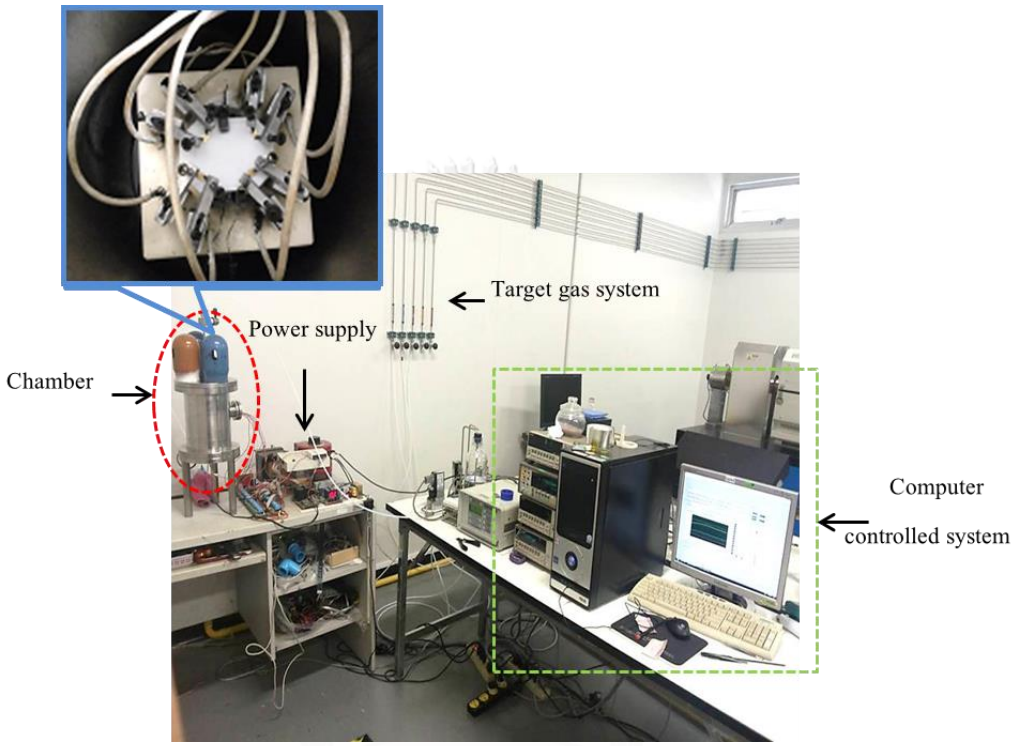

Figure 4.11: Gas sensing measurement.

The sensors were placed into chamber under the dry air atmosphere and heated with the different operating temperature from 150 to 350 ºC in order to obtain the optimum operating temperature. Then, the tested gas was injected inside the chamber and the changed resistance of sensor was measured with computer controlled system. In this thesis work, the target gases contained NO_2, H_2, NH_3, H_2S and ethanol gas. The gas sensing properties of undoped and Ni-doped CCTO sensors were characterized in terms of sensor response, response time and recovery time. In

addition, Sensor response of undoped and Ni-doped CCTO sensors can be calculated in equation (4.1) – (4.2) that are equation for n – type material.

$$S = \frac{R_a}{R_g} \quad \text{for reducing gas} \qquad (4.1)$$

$$S = \frac{R_g}{R_a} \quad \text{for oxidizing gas} \qquad (4.2)$$

where R_a is the resistance of the sensor measured in the dry air atmosphere.

R_g is the resistance of the sensor measured in tested gases.

In term of response and recovery times, the response time was defined as the time reached to 90% of the final signal when exposure to target gas. The recovery time of the sensor was determined similar to response time but it was measured time when exposure to air atmosphere as seen in Fig. 4.12.

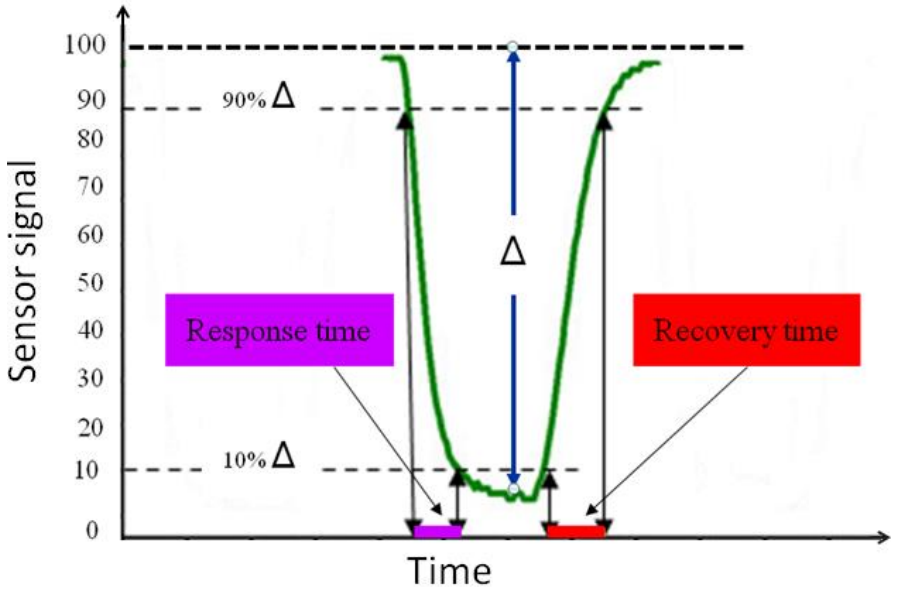

Figure 4.12: A typical signal of a sensor made from n-type semiconductor under reducing gas as a function of time.

CHAPTER V

RESULTS AND DISCUSSION

5.1 The characterization of crystal structure of undoped CCTO film and Ni-doped CCTO films prepared by NiO

The undoped CCTO films and Ni-doped CCTO films prepared by NiO were synthesized by a sol-gel method. The films were deposited on substrates for four layers and each layer was annealed at 800 °C. The X-ray diffraction (XRD) technique was used to study the crystal structure and phase composition of undoped and Ni-doped CCTO thin films. Fig. 5.1(a) shows XRD patterns of undoped and Ni-doped CCTO thin films on silicon substrate. It can be seen that all the films have similar diffraction patterns which indicate that all films are polycrystalline. The dominant diffraction peaks of silicon substrates were detected in XRD analysis on (200) and (400) planes. Moreover, there are the main diffraction peaks of CCTO at 2θ = 34.27º, 49.26º and 61.39º corresponding to the (220), (400) and (422) planes, respectively. The main diffraction peaks of CCTO are agreed well with the cubic perovskite CCTO (JCPDS 21-0140). The lattice parameter of CCTO thin films is 7.324 Å which can be calculated by Bragg's law equation on (220) plane. This lattice parameter is slightly lower than that of bulk CCTO (7.391 Å). In addition, XRD patterns can be seen the impurity phase of TiO_2 rutile at 2θ = 27.4º corresponding to the (110) TiO_2 plane. Overall undoped CCTO film shows the good sharpness of the CCTO peaks compared to those of Ni-doped CCTO films.

Furthermore, the crystal structure and phase composition of CCTO films deposited on alumina substrates were examined by XRD technique. The XRD patterns of undoped and Ni-doped CCTO thin films on alumina substrates are shown in Fig. 5.1(b). The diffraction peaks of polycrystalline CCTO films on alumina substrates can be observed in XRD patterns which is consistent with that of CCTO films on silicon substrates. The unknown peaks of XRD patterns of 1 and 4 wt% Ni-doped CCTO films are observed at 2θ = 21.26º and 23.69º. Because alumina substrates were used, the appearance of most diffraction peaks is from Al_2O_3 polycrystalline phases. Also, XRD patterns present the dominant diffraction peaks of gold (Au) electrode which is used to coat on the films.

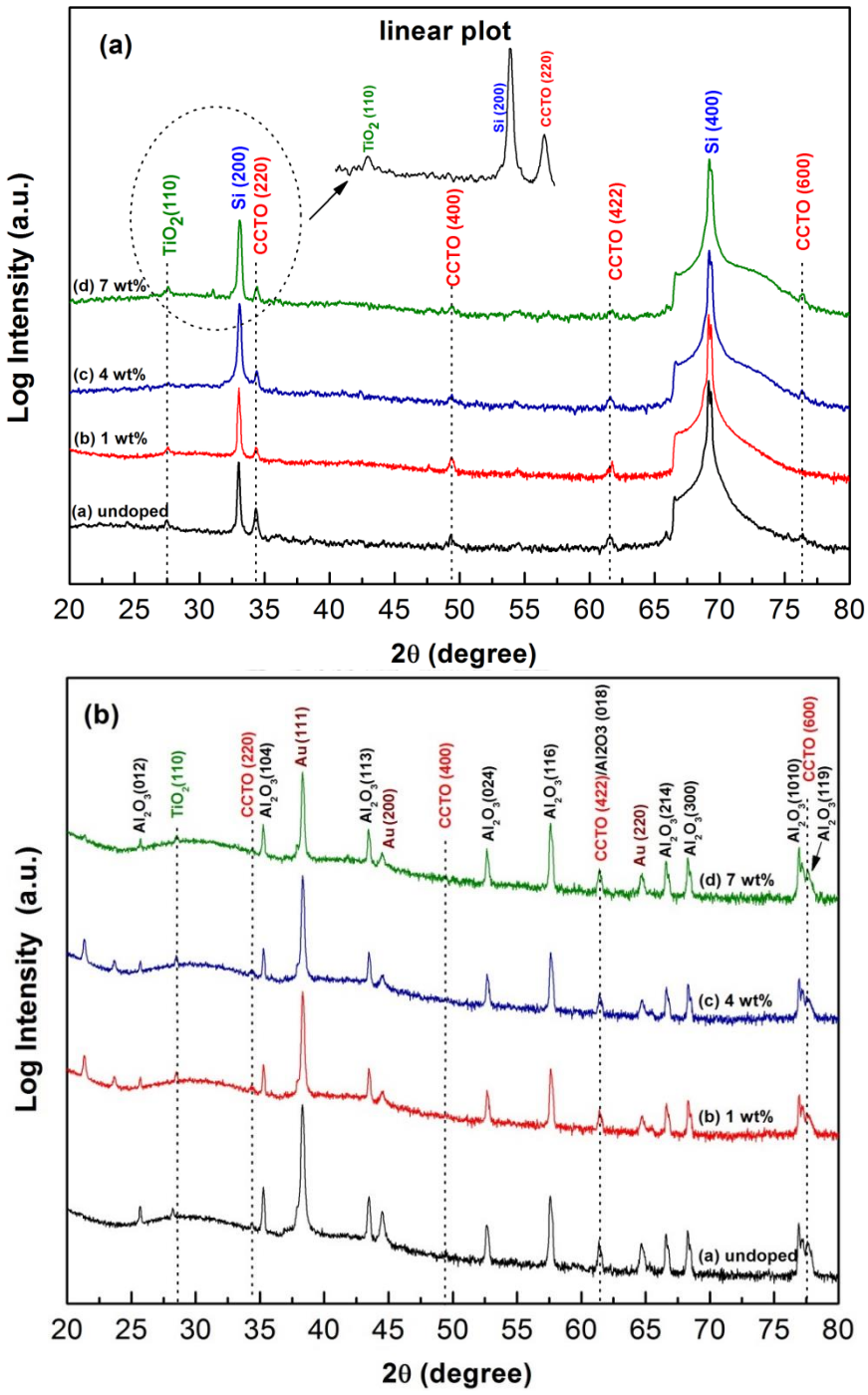

Figure 5.1: (a) XRD patterns of undoped CCTO films and Ni-doped CCTO films prepared by NiO on silicon substrates and (b) on alumina substrates annealed at 800 °C.

5.2 The characterization of surface morphology and thickness of undoped CCTO films and Ni-doped CCTO films prepared by NiO

Surface morphologies and film thickness of undoped and Ni-doped CCTO thin films annealed at 800 °C on silicon and alumina substrates are shown in Fig. 5.2 and 5.3, respectively. In Fig. 5.2(a)-(d), it could be observed that the size of granular particles is smaller as the doping level is higher. The granular particles for undoped CCTO are about 110 nm which are randomly distributed through the surface besides some big rods with the length of 480 nm. The average diameters of granular particles for Ni-doped CCTO are approximately 60 nm. Moreover, surface morphologies of 7 wt% Ni-doped CCTO exhibited the highest porosity compared to that of undoped, 1 wt% and 4 wt% Ni-doped CCTO film. The film thickness of each film was examined from the cross section images shown on the right side in Fig. 5.2(a)-(d). The interface between bottom film layer and silicon substrate top layer is quite clear. The thickness of four-layered films of undoped and 1 wt% Ni-doped CCTO on silicon substrates is approximately 540-600 nm whereas that of 4 wt% and 7 wt% Ni-doped CCTO is approximately 400 nm. This could be because 4 wt% and 7 wt% Ni-doped CCTO films have smaller grains and more pores. With the process of depositing layer by layer, when the next precursor was deposited on to the previous film surface it tends to cover pores as well as the whole surface. Fig. 5.3(a)-(d) also shows cross section images of the film on alumina substrate. It can be seen clearly that the surface of alumina substrates is very rough and the obtained four-layered film thickness range is very wide (~200-700 nm). In the case of surface morphologies of the films on alumina substrates, granular particles on the surface were observed as well but the film surface is more rough than in the case of the films on silicon substrates. The

roughness on the surface may be come from clusters aggregated on the film surface. This could be due to depositing only few layers on rough alumina substrates. The cluster forms can be seen clearly on the surface of Ni-doped CCTO films with smaller thickness especially for 4 wt% and 7 wt% Ni-doped CCTO films as shown in Fig. 5.3(b) and (c), respectively. The 7 wt% Ni-doped CCTO thin film on alumina substrate exhibited the highest film porosity and smallest film thickness ~ 300 nm. An average size of clustered particles is approximately 350 nm. The size of granular particles on the film surface deposited on alumina substrates is smaller with increasing Ni doping concentrations in the film. Also the granular particles are slightly smaller than those found in the films on silicon substrates. The average diameters of granular are approximately 45 nm.

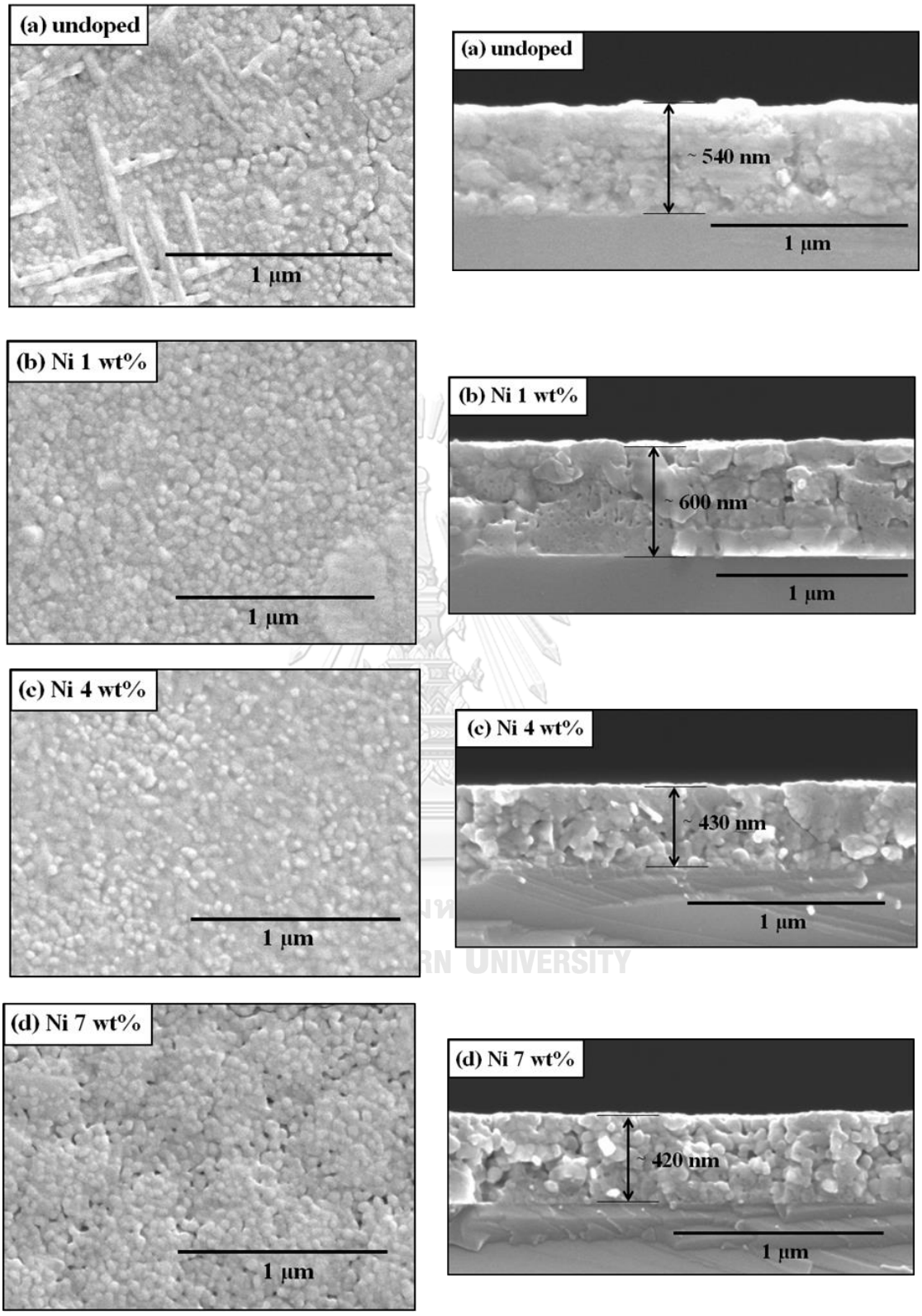

Figure 5.2: The FESEM images of undoped and Ni-doped CCTO thin films prepared by NiO on silicon substrates.

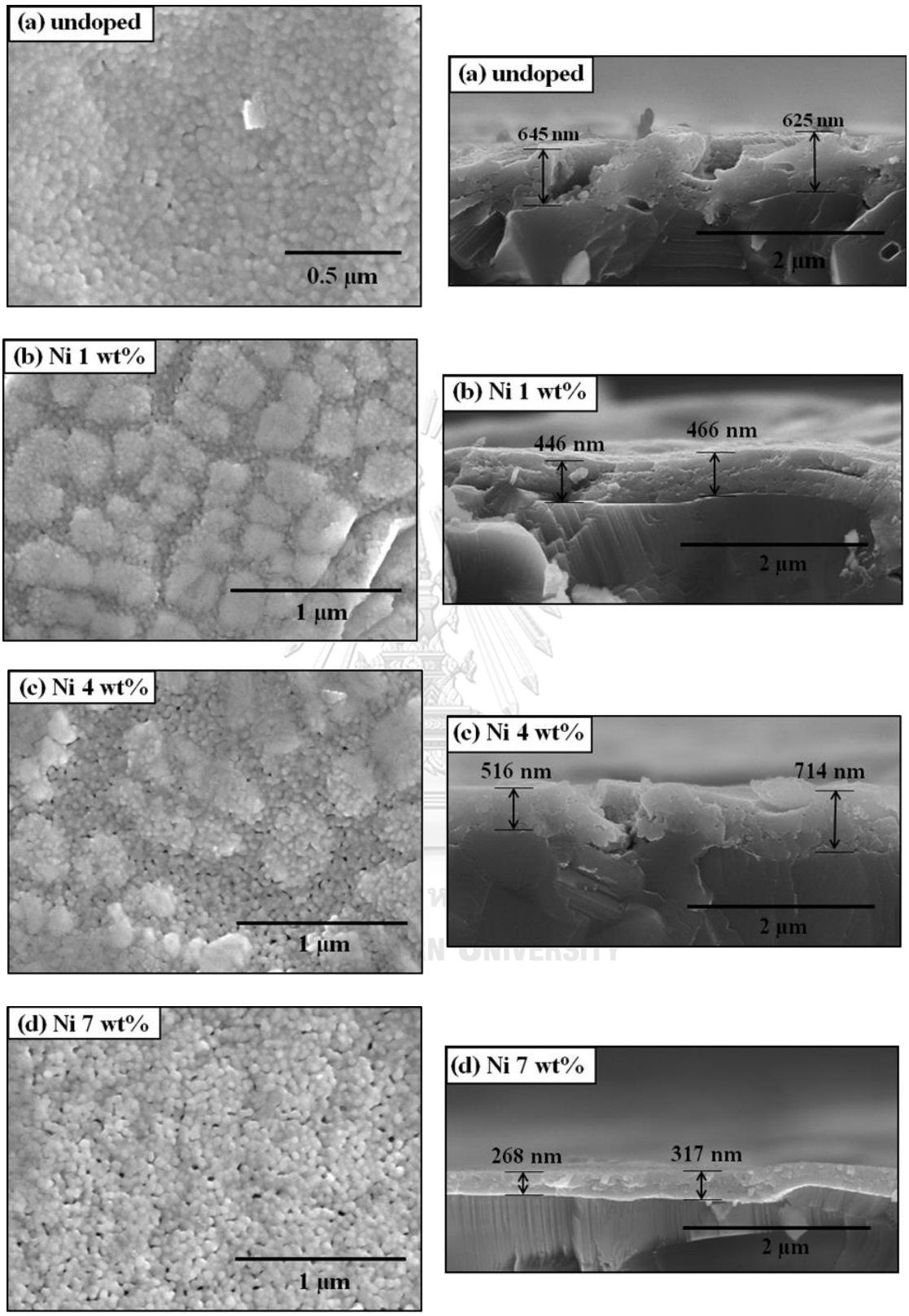

Figure 5.3: The FESEM images of undoped and Ni-doped CCTO thin films prepared by NiO on alumina substrates.

5.3 The characterization of elemental composition of undoped and Ni-doped CCTO films prepared by NiO

Fig. 5.4(a) and (b) show the EDX spectra of undoped and 7 wt% Ni-doped CCTO film, respectively. Chemical elements in both undoped and 7 wt% Ni-doped CCTO film were confirmed by EDX spectra. Table 5.1 presents the data base for the element types and energy of X-ray emission lines of each element. Calcium (Ca), copper (Cu), titanium (Ti), and oxygen (O) in films are present in both films. Signal due to nickel (Ni) was only observed in Ni-doped CCTO films. In addition, Ni signal in 7 wt% Ni-doped CCTO film appeared nearby Cu signal and the intensity of Ni signal is quite strong, almost equal to Cu signal. Moreover, the concentrations both by weight % and atomic % of each elemental composition in undoped and Ni-doped CCTO films were analyzed by EDX technique and these values are shown in Table 5.2. Figure 5.5(a) shows the plot of measured Ni doping concentrations and the calculated concentration of Ni added in precursor solutions. The measured Ni doping concentrations increase with increasing the Ni-doping concentration in precursor solutions. A linear trend with the slope equal to 0.68 ± 0.04 which is nearly one is obtained. Moreover, the measured Ti concentrations decrease linearly with increasing the concentrations of Ni in precursor solutions as presented in Fig. 5.5(b). This suggested that some Ti atoms were replaced by Ni atoms due to the atomic radius of Ni (149 pm) is near to the atomic radius of Ti (176 pm). In addition, the substitution of Ni into Ti sites increases with increasing Ni-doping concentrations. From these results, they can be confirmed that Ni is doped into the Ni-doped CCTO films.

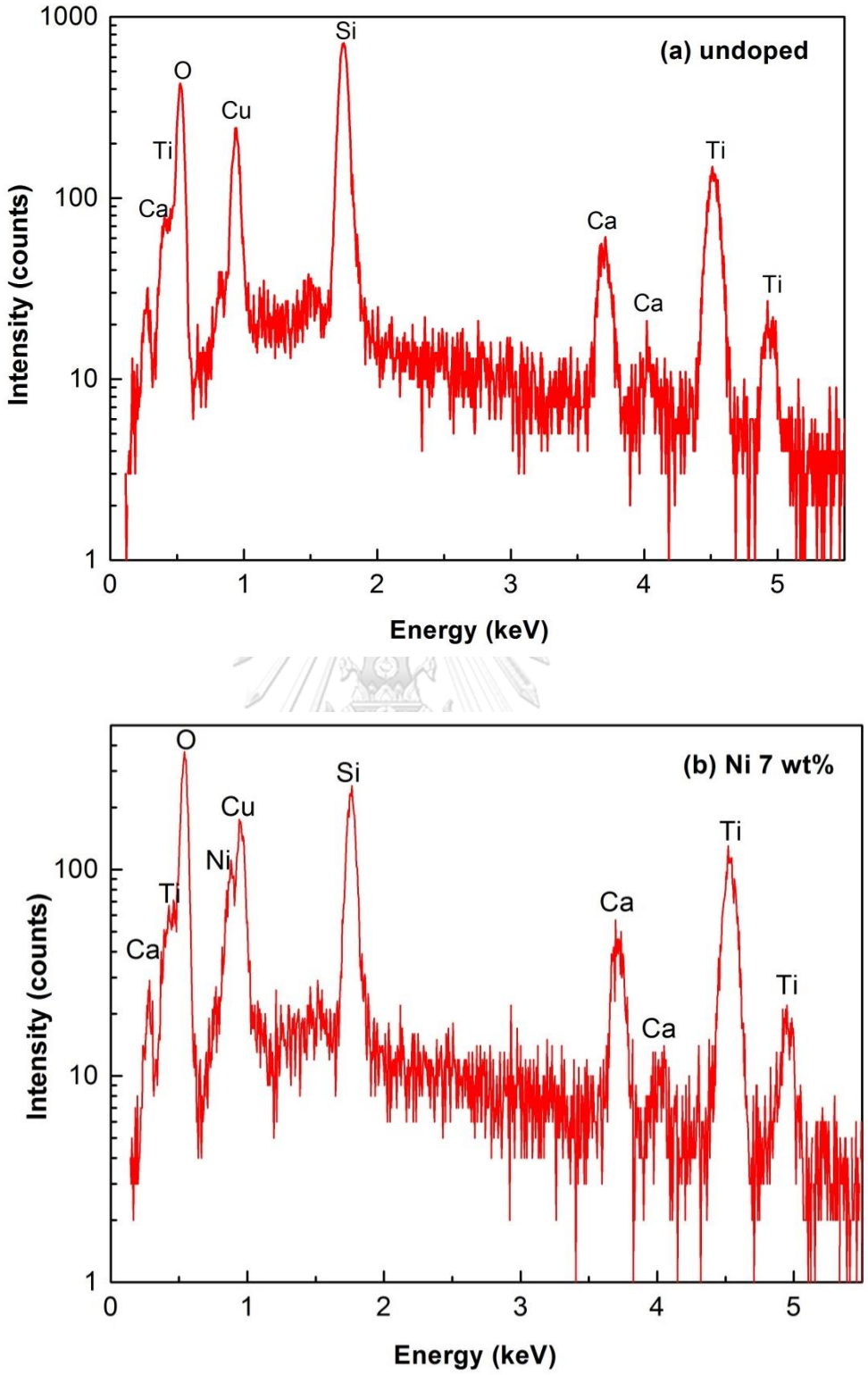

Figure 5.4: EDX spectra of (a) undoped CCTO thin film and (b) 7 wt% Ni-doped CCTO thin film.

Table 5.1: Database of EDX spectra between element types and energy of X-ray emission lines.

Element	$k_{\alpha 1}$ (keV)	$k_{\beta 1}$ (keV)	$L_{\alpha 1}$ (keV)
Ca	3.69168	4.0127	0.3413
Cu	8.04778	8.90529	0.9297
Ti	4.51084	4.93181	0.4522
O	0.5249	-	-
Ni	7.47815	8.26466	0.8515
Si	1.73998	1.83594	-

Table 5.2: The concentrations of elemental composition by weight% and atom% of undoped and Ni-doped CCTO films on silicon substrate prepared by NiO.

Element	undoped CCTO (Weight%)	1 wt% Ni-doped CCTO (Weight%)	4 wt% Ni-doped CCTO (Weight%)	7 wt% Ni-doped CCTO (Weight%)
Ca	9.01	8.25	8.29	7.65
Cu	11.95	11.18	10.09	14.24
Ti	43.38	41.03	40.16	36.74
O	35.65	38.55	38.23	36.59
Ni	0	0.99	3.23	4.78

Table 5.2: The concentrations of elemental composition by weight% and atom% of undoped and Ni-doped CCTO films on silicon substrate prepared by NiO. (cont)

Element	undoped CCTO (Atomic%)	1 wt% Ni-doped CCTO (Atomic%)	4 wt% Ni-doped CCTO (Atomic%)	7 wt% Ni-doped CCTO (Atomic%)
Ca	6.34	5.61	5.67	5.38
Cu	5.3	4.8	4.35	6.31
Ti	25.53	23.38	22.98	21.16
O	62.82	65.75	65.49	64.42
Ni	0	0.46	1.51	2.29

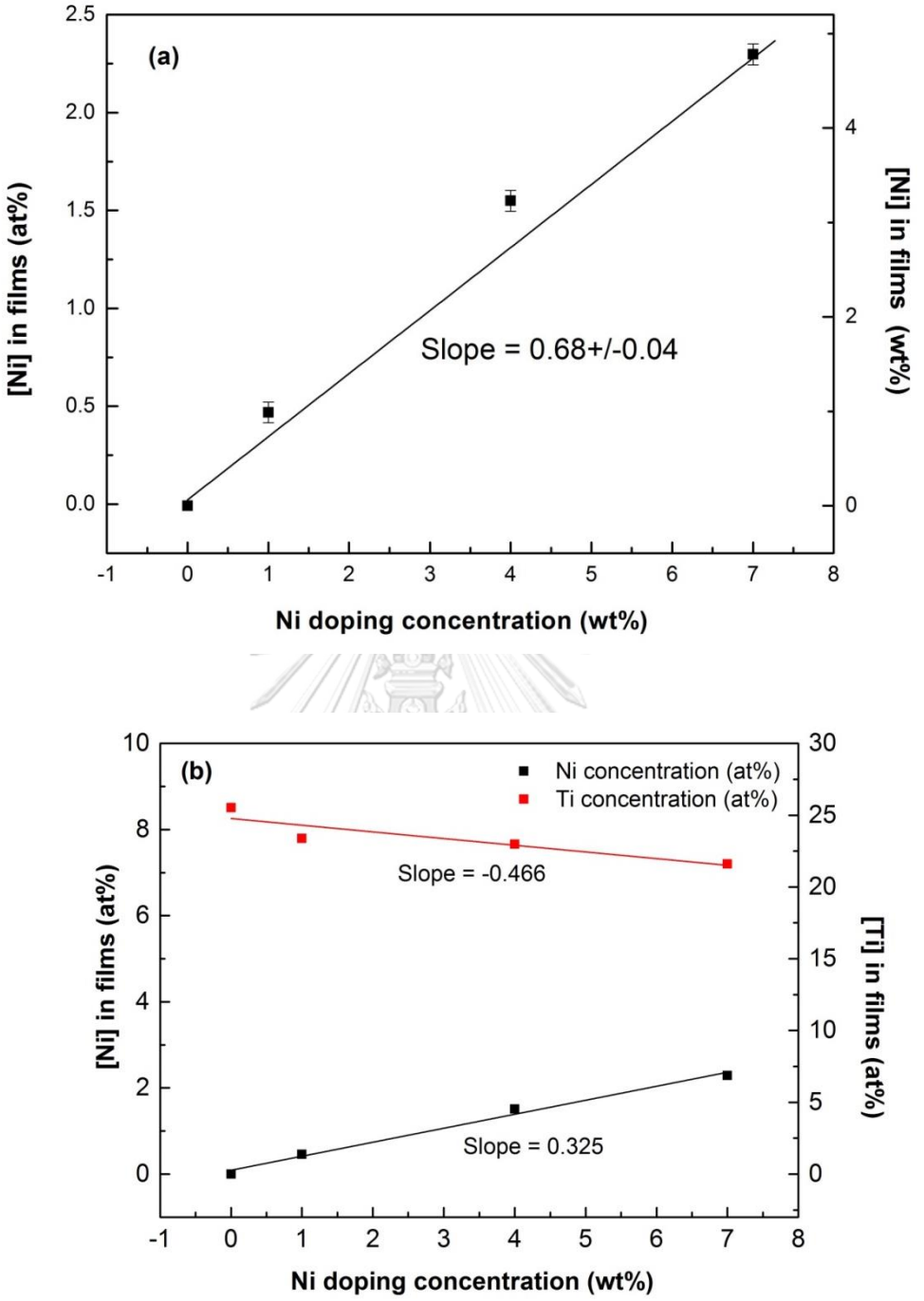

Figure 5.5: EDX spectra of (a) the plot of measured Ni-doping concentrations and the concentration of Ni in precursor solutions and (b) the correlation between the concentration of Ni atom percent and Ti atom percent.

5.4 The characterization of information on molecular vibrations and crystal structures of undoped and Ni-doped CCTO films prepared by NiO

The Raman spectroscopy was used to analyze the vibrational, rotational, and other low-frequency modes of undoped and Ni-doped CCTO thin films. The set of CCTO films used in this study was grown on silicon substrates. The Raman spectra in the Raman shift range of 100-1000 cm^{-1} for the CCTO films are shown in Fig. 5.6(a). It can be observed that the intensity signal of undoped CCTO film is much stronger than that of Ni-doped CCTO films. Figure 5.6(b) presented the comparison of Raman spectra of all Ni-doped CCTO films. It can be seen that the frequencies of the Raman bands at 445 and 509 cm^{-1} are associated to TiO_6 rotation-like modes, whereas Ti–O–Ti antistretching vibrations of TiO_6 octahedra shows at 577 cm^{-1} [7]. The bending vibration mode of (O-Ti-O) in $CaTiO_3$ presents at 246 cm^{-1} [22]. Moreover, the frequencies of the Raman bands for rutile TiO_2 are at 145, 417 and 608 cm^{-1} [45, 46]. The frequencies of the Raman bands at 288 cm^{-1} are associated to CuO phase [7]. The new frequencies of the Raman bands were found specifically in Ni-doped CCTO films are at 345, 395 and 709 cm^{-1} [46]. The intensity of Ni signals at 345, 395 and 709 cm^{-1} increase with increasing Ni doping concentration. These signals are suggested that is the breathing mode of the NiO_6 octahedral units. Therefore, it is supporting the hypothesis of Ti substitution upon Ni-doping based on the EDX results.

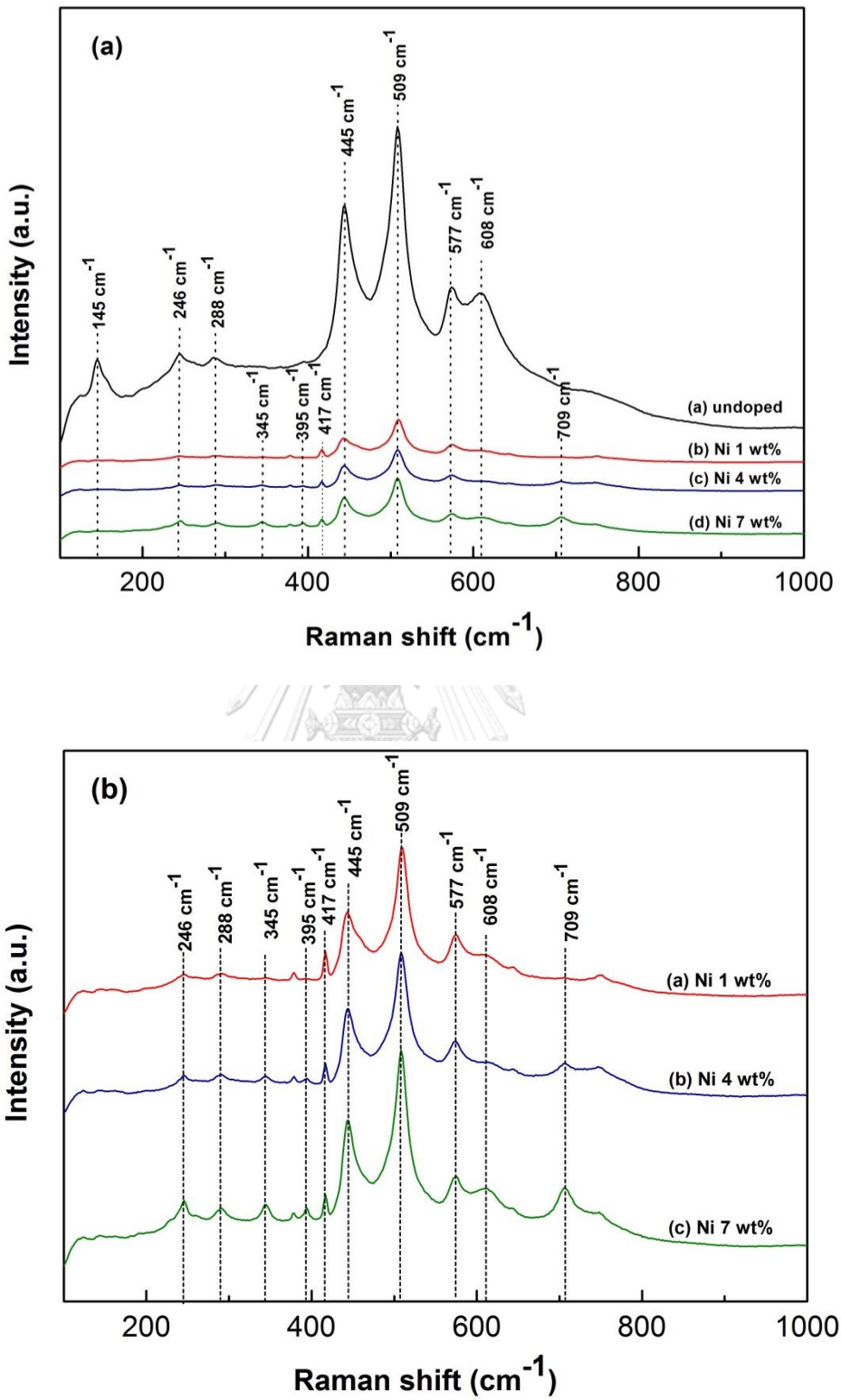

Figure 5.6: (a) Raman spectra of undoped and Ni-doped CCTO films and (b) Raman spectra of Ni-doped CCTO films annealed at 800˚C on silicon substrate.

5.5 The characterization of oxidation state of 7 wt% Ni-doped CCTO films prepared by NiO

The chemical state of Ni-doped CCTO thin films were identified by X-ray photoelectron (XPS) measurement located at Petrochemical College (PPC) Chulalongkorn University. The XPS survey spectrum or full spectrum is illustrated in Fig. 5.7(a) presenting five elements (O, Ca, Cu, Ti and Ni) in the Ni -doped CCTO films. As shown in Fig. 5.7(b) displaying XPS spectra of O 1s, the main peak of O 1s is at 529.6 associated to substitutional oxygen atoms and the second main peak is at 531.6 eV associated to chemiabsorbed oxygen atoms [22]. As presented in Fig. 5.7(c), the Ca 2p XPS spectrum show the binding energies at 350.0 and 346.5 eV for Ca $2p_{1/2}$ and Ca $2p_{3/2}$, respectively. These peaks can be assigned to calcium in +2 oxidation state [47, 48]. The presence of copper in 2+ oxidation state in the films is evidenced from the binding energy of the Cu $2p_{1/2}$ and Cu $2p_{3/2}$ at 954.0 eV and 933.9 ev, respectively as shown in Fig. 5.7(d) [49, 50]. Their satellite peaks of the Cu $2p_{1/2}$ and Cu $2p_{3/2}$ can be also observed at binding energy at 962.2 and 942.2 eV, respectively [51]. The binding energies of Ti $2p_{1/2}$ and Ti $2p_{3/2}$ are at 463.9 and 458.2, respectively as shown in Fig. 5.7(e). Both Ti 2p binding energies show the oxidation state of Ti^{4+} that agrees with the report by Haoa, W. et.al [52]. In the case of core level Ni 2p, Ni $2p_{1/2}$ peak is located at 873.1 eV and Ni $2p_{3/2}$ peak is located at 855.5 eV corresponding to nickel in +2 oxidation state [24, 53, 54] as presented in Fig. 5.7(f). Moreover, the satellite peaks of Ni can be seen at binding energies at 879.6 and 861 eV for Ni $2p_{1/2}$ and Ni $2p_{3/2}$, respectively [56, 25]. The oxidation state of Ni can be confirmed that a chemical state of Ni is only 2+ not 3 + and 0.

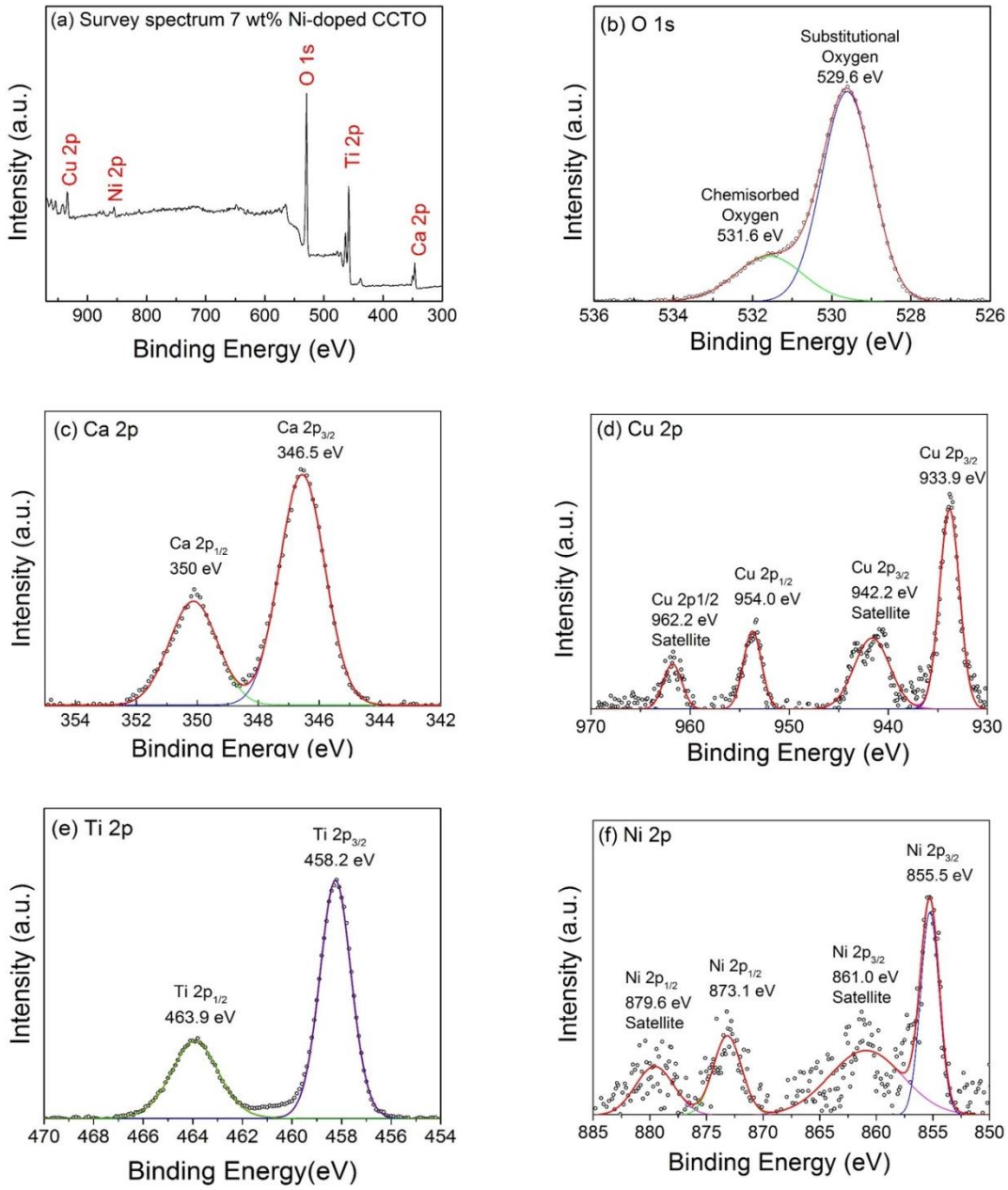

Figure 5.7: XPS spectra of (a) survey spectrum, (b) O 1s, (c) Ca 2p, (d) Cu 2p, (e) Ti 2p, and (f) Ni 2p core levels for 7 wt% Ni-doped CCTO films.

5.6 Characterization of the gas sensor properties of undoped CCTO films and Ni-doped CCTO films prepared by NiO

The undoped and Ni-doped CCTO gas sensor films were fabricated and their gas sensing properties were characterized. For gas sensing measurements, the target gases are H_2S, NO_2, H_2, NH_3 and ethanol gas testing in the operating temperature range of 150 to 350 °C. Based on the previous study in our laboratory, first I will focus on testing the sensor response towards H_2S in the 0.2-10 ppm concentration range [22].

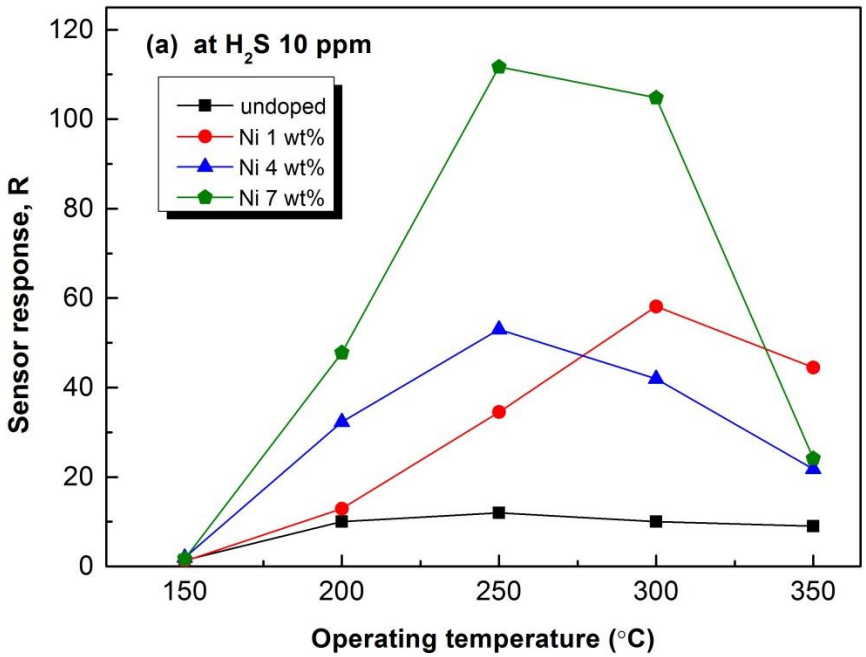

Figure 5.8: Sensor response of of Ni-doped CCTO sensors prepared by NiO as a function of temperature towards 10 ppm H_2S.

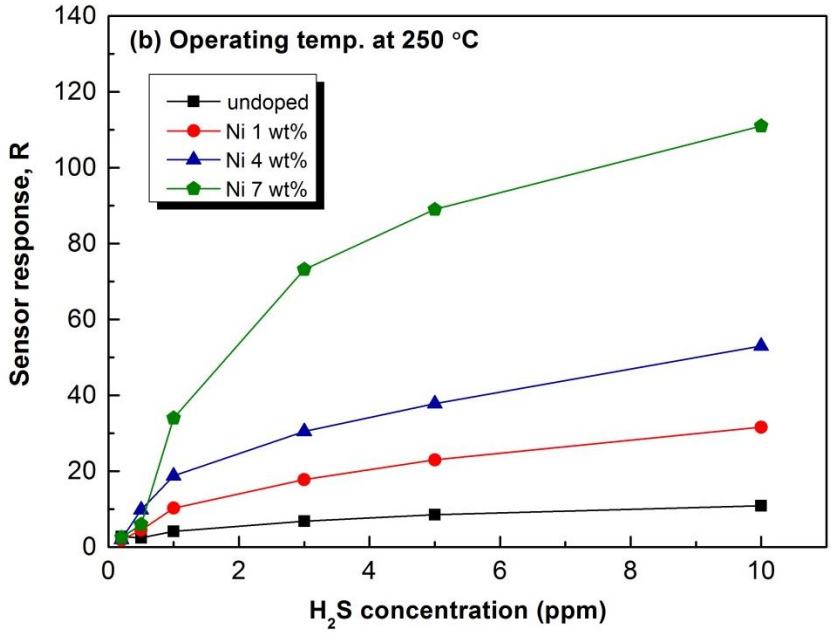

Figure 5.9: Sensor response of Ni-doped CCTO sensors prepared by NiO as a function of H_2S concentrations at 250 ºC.

The sensor response for reducing gas was calculated by using $S = R_a/R_g$ ratio, where R_a is the resistance value under the air atmosphere and R_g is the resistance value under the injection of the target gas. Generally, it is well known that the optimum temperature highly affects the sensor response. Fig. 5.8 shows the sensor response towards H_2S as a function of operating temperature in the temperature range of 150-350 ºC. It can be seen that the sensor response of undoped, 4 wt% and 7 wt% Ni-doped CCTO films increases with increasing the operating temperature up to 250 ºC while for that of 1 wt% Ni-doped CCTO increases up to 300 ºC, and then decreased. The highest sensor response at 250 ºC of undoped, 4 wt% and 7 wt% Ni-doped CCTO films is 12, 53 and 112, respectively but the highest sensor response of 1 wt% Ni-doped CCTO film is 35 at 300 ºC. The varying optimum temperature of films can be described with the relation between the temperature and the speed of chemical and diffusion reactions. The speed of chemical reaction affects the sensor

response that will be limited at low operating temperature. For high temperature, the speed of diffusion of the target gas molecules is low which is a limitation for the sensor response. Therefore, the sensor response is the maximum at the intermediate optimum temperature when the speed of diffusion of the target gas molecules is equal to the speed of chemical reaction [28]. However, the undoped and Ni-doped CCTO films were suggested that the optimum temperature for H_2S detection is 250 °C. The 7 wt% Ni-doped CCTO film presented the best sensor response that the sensor response was twelve times better than that of undoped CCTO film. Moreover, it can be seen that the sensor response depends on H_2S concentration as presented in Fig. 5.9. The sensor response increases with increasing H_2S concentration. The highest sensor response of undoped and Ni-doped CCTO films is at 10 ppm H_2S and the 7 wt% Ni-doped CCTO film show the excellent sensor response of 112 towards 10 ppm of H_2S at 250 ºC.

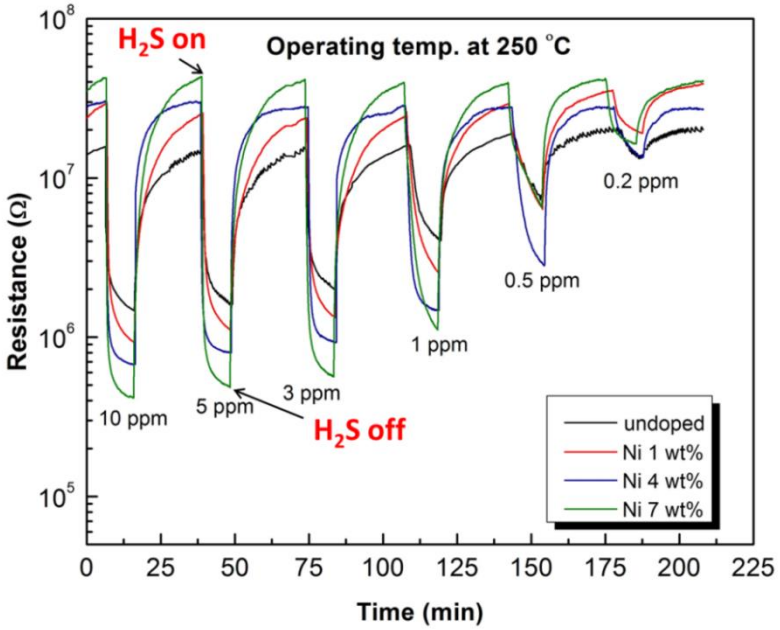

Figure 5.10: Resistance curve of Ni-doped CCTO sensors prepared by NiO as a function of time under 0.2-10 ppm H_2S concentrations.

The dynamic resistance curve of undoped and Ni-doped CCTO films under exposure to varying H_2S concentrations at 250 ºC are shown in Fig. 5.10. The sensor exhibited best sensor response in this temperature due to it was suggested to the optimum temperature. It can be seen that the resistance of films is 10^7-10^8 Ω under an air atmosphere. As H_2S (reducing gas) was injected into the chamber, the resistances of sensor were decreased. This can be explained by the reactions between the oxygen species and a reducing gas (see the explanation in the gas mechanism later on). The reduction of resistance is a behavior towards a reducing gas so this can be confirmed that undoped and Ni-doped CCTO films are n-type semiconductor that agrees with previous work [22]. In addition, when the sensor is exposed to H_2S the resistance of undoped CCTO sensor change less than that of Ni-doped CCTO sensor. The changing resistance of Ni-doped CCTO increases with increasing Ni-doping concentrations and H_2S concentrations. The 7 wt% Ni-doped CCTO presented highest changing in resistance.

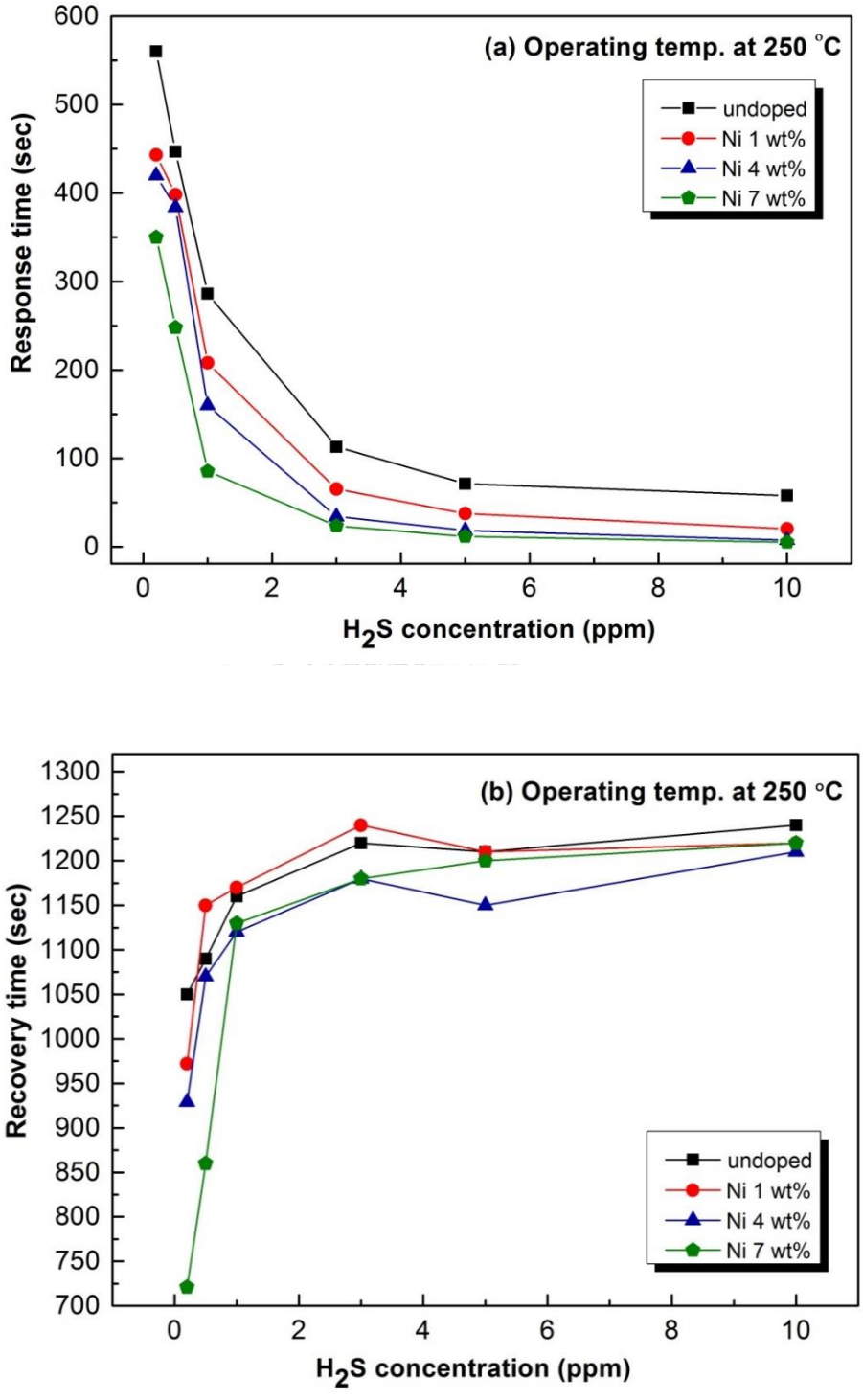

Figure 5.11: (a) Response time curve and (b) recovery time curve of Ni-doped CCTO sensors prepared by NiO sensor in the range of 0.2 to 10 ppm H_2S concentrations.

Other important gas sensing properties are the response time and the recovery time. The good sensor exhibits a small value of the response and recovery times. The response and recovery characteristics of the Ni-doped CCTO films as a function of 0.2-10 ppm H_2S concentrations at 250 °C is shown in Fig. 5.11. In Fig. 5.11(a), it can be observed that the response time of undoped and Ni-doped CCTO films decreases with increasing H_2S concentrations. The minimum response times are at 10 ppm of H_2S which is the maximum H_2S concentration used in this study. The response time for 10 ppm H_2S of undoped CCTO is 58 s while the response time of Ni-doped films drop to 20, 7 and 5 s for 1, 4 and 7 wt% Ni-doping concentration, respectively. Moreover, it can be seen that the undoped CCTO film showed the response time more than ten times that of Ni-doped CCTO sensor. The 7 wt% Ni-doped CCTO sensor exhibited the minimum response time. The recovery time under various H_2S concentration at 250 °C is presented in Fig. 5.11(b). The recovery time of undoped and Ni-doped CCTO sensors increases strongly with increasing H_2S concentrations up to 1 ppm. After that the recovery time increase gradually with increasing H_2S concentrations up to 10 ppm H_2S. The recovery time of 7 wt% Ni-doped CCTO sensor operated at 10 ppm H_2S is the maximum at ~1220 s.

As mention earlier, the undoped and Ni-doped CCTO films were tested towards different types of gases such as H_2S, NO_2, H_2, NH_3 and ethanol gas at 250 ºC. Table 5.3 shows the sensor response of undoped and Ni-doped CCTO films toward different types of gases. The response as a function of Ni-doping concentration were plotted as linear and log scales as shown in Fig. 5.12. It can be seen that the sensor response of films exposed to NH_3 at 2000 ppm and ethanol gas at 2000 ppm is less than 2 exhibiting poor sensor response towards these two gases. For H_2 testing to be

detectable, the H_2 concentration needs to be very high about 30000 ppm. As espected, the undoped and Ni-doped CCTO sensor illustrated the best sensor response towards H_2S. However, the undoped and Ni-doped CCTO sensor showed a moderate sensor response under NO_2 at 5 ppm as seen in inset Fig. 5.14. This result is similar to Wang, Y. research [28].

Table 5.3: Sensor response of undoped and Ni-doped CCTO sensor towards various gases.

Ni-doping concentration (wt%)	Sensor response, R				
	H_2S (10 ppm)	NO_2 (5 ppm)	H_2 (30000 ppm)	NH_3 (2000 ppm)	Ethanol (2000 ppm)
undoped	12	1.30	1.1	1.2	1.7
1	35	5.03	2.29	1.21	1.29
4	53	4.33	2.23	1.25	1.07
7	112	5.54	3.93	1.11	1.96

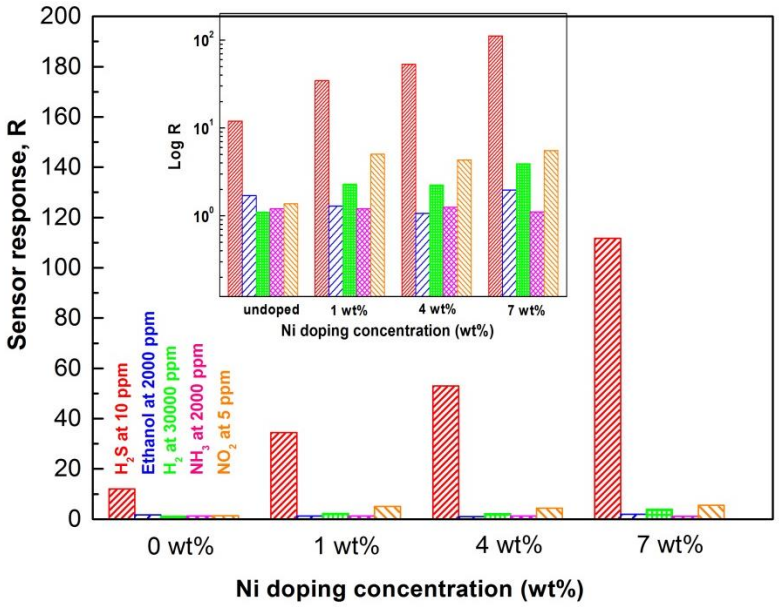

Figure 5.12: Selectivity of undoped and Ni-doped CCTO sensors prepared by nickel oxide towards H_2S, NO_2, H_2, NH_3 and ethanol gas.

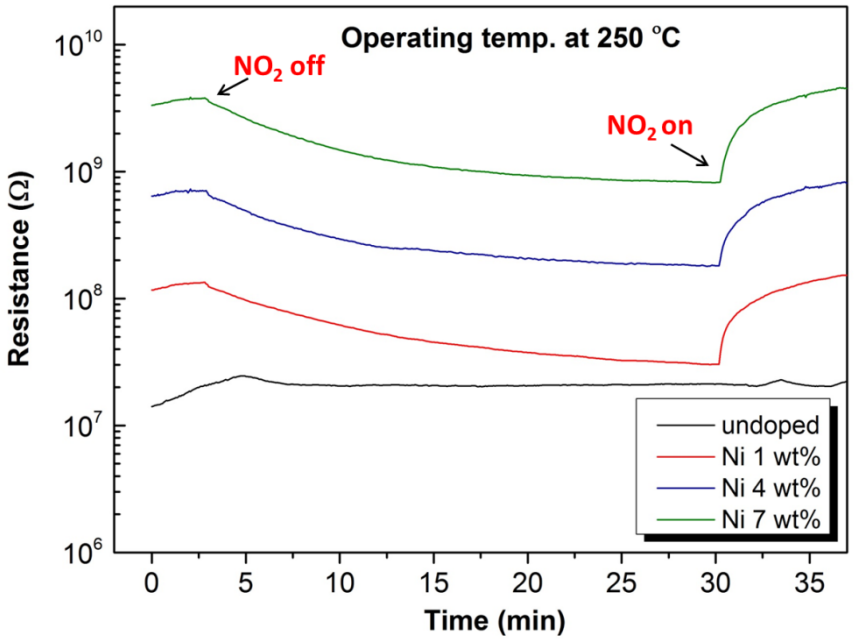

Figure 5.13: Resistance curve as a function of time under 5 ppm NO_2 concentrations.

Undoped and Ni-doped CCTO film sensors were exposed to NO_2 and the resistance curve as a function of time under 5 ppm NO_2 was obtained as shown in Fig. 5.13. It can be seen that the resistance of Ni-doped CCTO sensor increases when NO_2 was absorbed on sensor surface. However, the undoped CCTO sensor exhibited a smaller increase in resistance. The enhancement in resistance can be described with gas mechanism of the film and NO_2 gas as explained in the section 5.11. The increase in resistance towards an oxidizing gas like NO_2 of the films represented n-type semiconductor behavior of undoped and Ni-doped CCTO films. Even though I did not test the optimum temperature for NO_2. In comparison with the results from Y. Wang et al. [28], the optimum operating for NO_2 is expected to be lower than 250 ºC and this could lead to enhance the response about two times.

5.7 The characterization of crystal structure of undoped CCTO films and Ni-doped CCTO films prepared by nickel (II) acetate

The XRD patterns of Ni-doped CCTO thin films with using nickel (II) acetate which were prepared by sol-gel method are shown in Fig. 5.14. XRD patterns of undoped and Ni-doped CCTO thin films on silicon substrate are illustrated in Fig. 5.14(a). It can be seen that all films have similar diffraction patterns and it is also similar to XRD patterns of undoped and Ni-doped CCTO thin films prepared by NiO. The presence of dominant diffraction peaks are silicon substrate at 2θ = 33.03º and 69.18º associated with (200) and (400) planes. Moreover, the XRD patterns indicate that the films are cubic perovskite CCTO structure (JCPDS 21-0140) due to the main diffraction peaks of CCTO appear at 2θ = 34.27º, 49.26º and 61.39º corresponding to the (220), (400) and (422) planes, respectively. The lattice parameter of CCTO thin film is 7.351 Å that it is slightly lower than that of bulk CCTO (7.391˚A). In addition, the impurity phase of TiO_2 also appear at 2θ = 27.44º corresponding to the (110) plane of TiO_2 rutile. The appeared impurity phase is similar to XRD patterns of undoped and Ni-doped CCTO thin films using NiO as a dopant material. Fig. 5.14(b) shows the XRD patterns of undoped and Ni-doped CCTO thin films on alumina substrate. It can be seen that XRD patterns is similar to XRD patterns of undoped and Ni-doped CCTO thin films prepared by NiO. It was observed that the diffraction peaks of undoped and Ni-doped CCTO films deposited on alumina substrates are the same as seen in that of the films grown on silicon substrates. Thus, the crystal structure of CCTO films are independent of the types of substrates used in this study. Moreover, the most dominant diffraction peaks are from gold (Au) electrode and Al_2O_3 substrates.

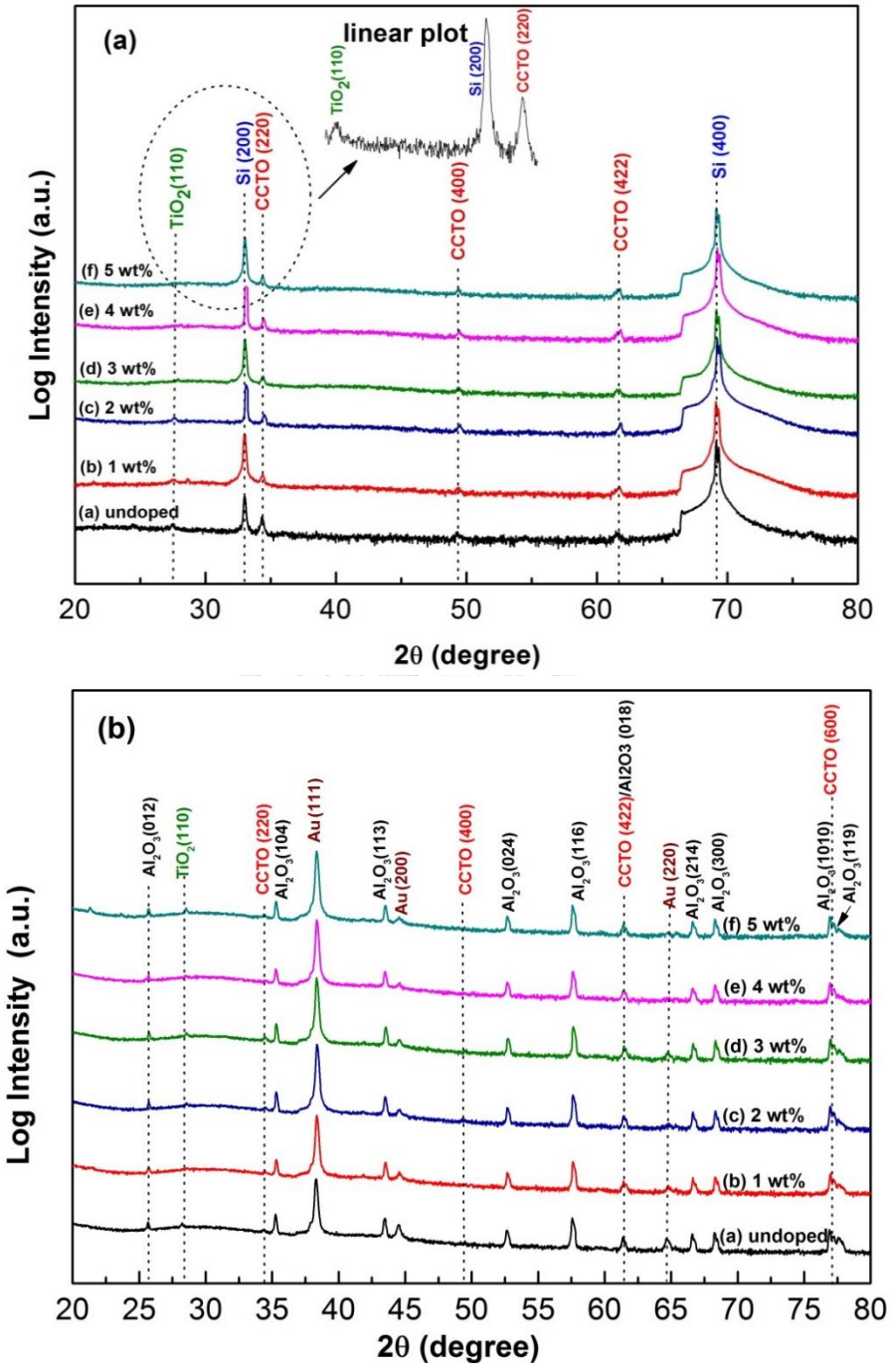

Figure 5.14: XRD patterns of (a) undoped and Ni-doped CCTO thin films prepared by nickel acetate on a silicon and (b) alumina substrate annealed at 800 °C.

5.8 The characterization of surface morphology and thickness of undoped CCTO films and Ni-doped CCTO films prepared by nickel acetate

Figure 5.15 shows surface morphologies and film thickness of films prepared by nickel (II) acetate on silicon substrate. In Fig. 5.15(a), the surface morphologies of undoped CCTO films displayed both the granular and rods which are about 110 and 480 nm, respectively. While Ni-doped CCTO films exhibited the granular particles which are approximately 64 nm in Fig5.15(b) - (f) and it can be seen some clustered forms of the granular with the average diameters ~ 325 nm in 4 wt% Ni-doped CCTO film. The porosity can be also observed on surface of film. The porosity of Ni-doped CCTO films is higher than the undooped CCTO and the 4 wt% Ni-doped CCTO films shown the highest porosity. Moreover, the thickness of films could be observed from the cross section images on the right side in Fig. 5.15 – 5.16. It is about 540 nm for undoped CCTO film whereas that the obtained four-layered thickness ranges of Ni-doped CCTO films is approximately 350 – 450 nm. The 4 wt% Ni-doped CCTO is the least thickness due to it is the highest porosity. For films on alumina substrate as shown in Fig. 5.16, the surface morphologies of undoped films shown granular particles and rods similar to surface morphologies of films on silicon substrate but the granular and rods is smaller size. The Ni-doped CCTO films displayed the granular and clusters particles and the average size are approximately 44 and 305 nm, respectively. Fig. 5.16 also shows cross section images of the film on alumina substrate. It can be seen that the film surface and alumina substrate are rough similar to Ni-doped CCTO films prepared by NiO. The thickness of undoped CCTO films is higher than Ni-doped CCTO films. The obtained thickness of undoped CCTO films is

approximately 630 nm and Ni-doped CCTO in the range is 320 -520 nm.

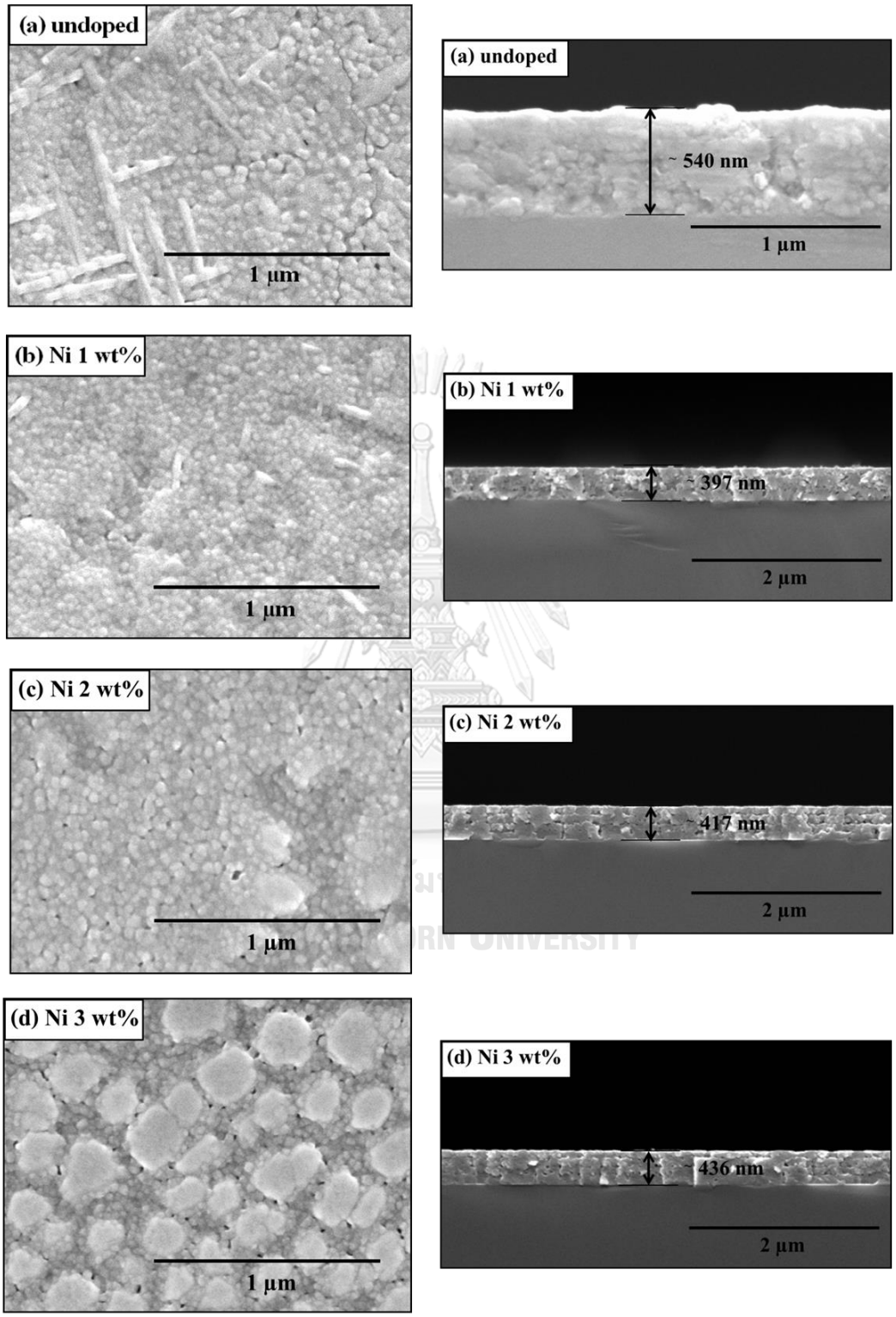

Figure 5.15: The FESEM images of undoped and Ni-doped CCTO thin films prepared by nickel acetate on silicon substrate.

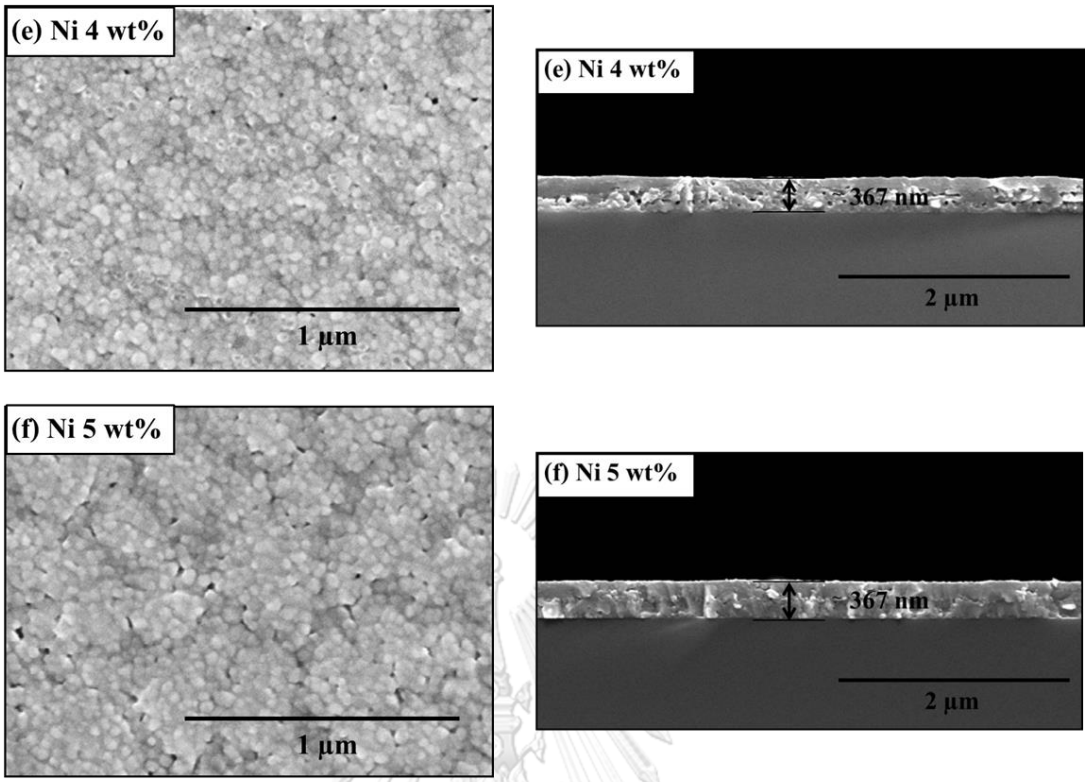

Figure 5.15: The FESEM images of undoped and Ni-doped CCTO thin films prepared by nickel acetate on silicon substrate. (cont)

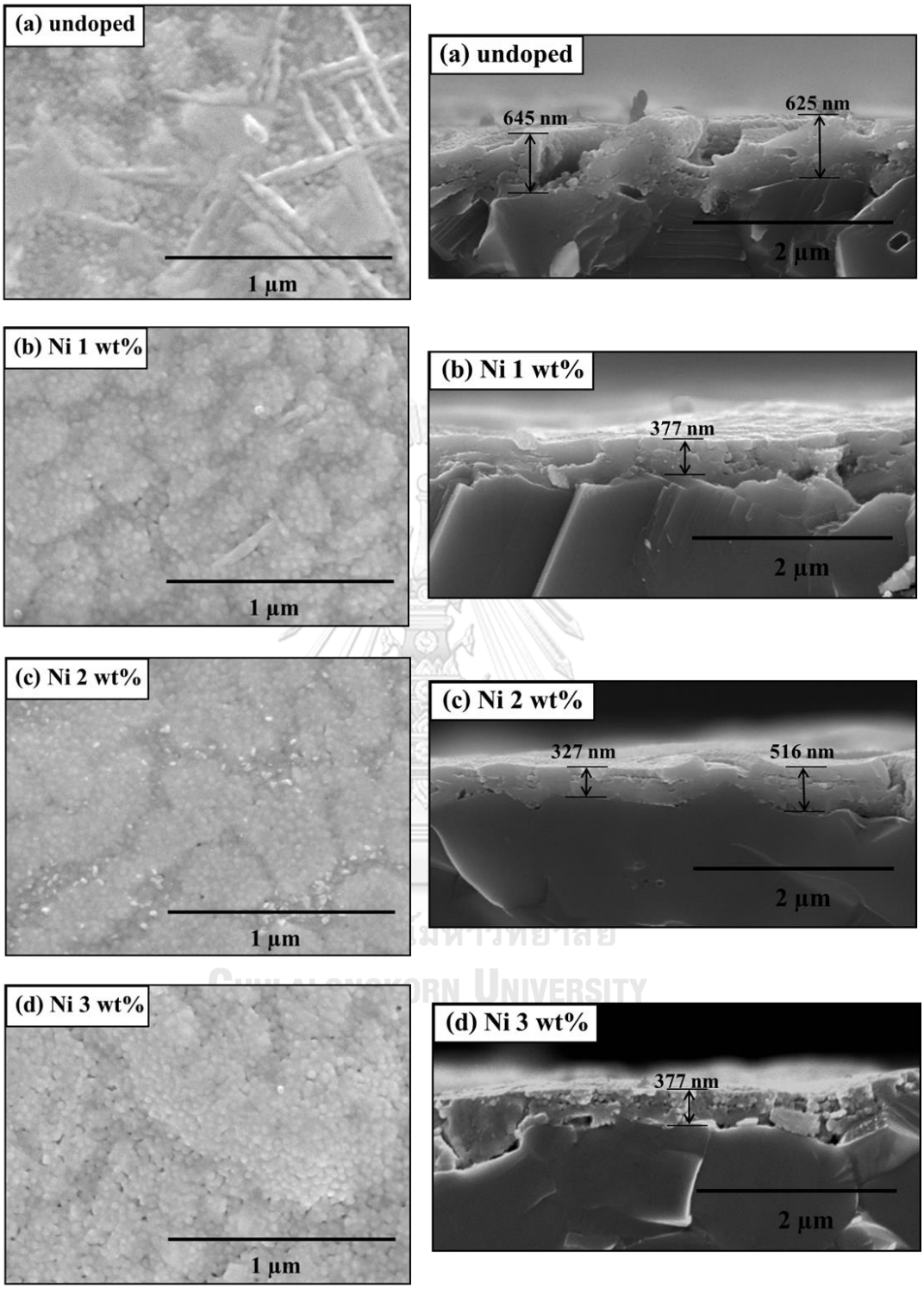

Figure 5.16: The FESEM images of undoped and Ni-doped CCTO thin films prepared by nickel acetate on alumina substrate.

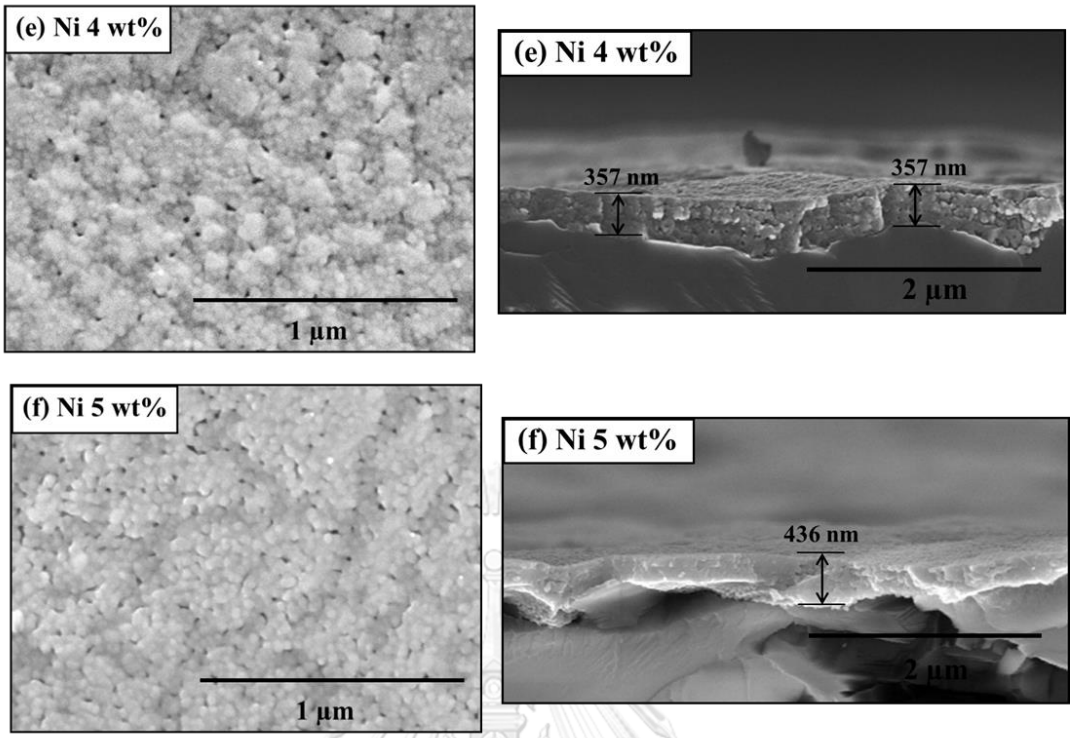

Figure 5.16: The FESEM images of undoped and Ni-doped CCTO thin films prepared by nickel acetate on alumina substrate. (cont)

5.9 The characterization of elemental composition of undoped CCTO films and Ni-doped CCTO films prepared by nickel (II) acetate

We will do the same analysis with the resulting Ni-doped CCTO films prepared by nickel acetate on characterizing the chemical elements as in Ni-doped CCTO films prepared by nickel oxide. Here 5 wt% Ni-doped CCTO thin film prepared by nickel acetate is used for this analysis. The spectra confirm the presence of calcium (Ca), copper (Cu), titanium (Ti), and oxygen (O) in films and nickle (Ni) signal is only observed in the doped film as presented in Fig. 5.15(a) and (b). Fig. 5.16 shows plot of measured Ni doping concentrations obtained by EDX measurement and the concentration of Ni in precursor solutions prepared by nickel acetate**.** The measured Ni doping concentrations increase with increasing the concentration of Ni in precursor solutions yielding a slope of 0.73 ± 0.05 which is very close to 1. The substitution of Ni into Ti sites is still in the argument because the measured Ti concentrations do not decrease linearly with increasing Ni-doping concentrations. However, in some chosen data set, the measured Ti concentrations decrease linearly with increasing Ni-doping concentrations. It could be conclude that Ni is doped into the Ni-doped CCTO films prepared by nickel acetate as well as the films prepared by nickel oxide.

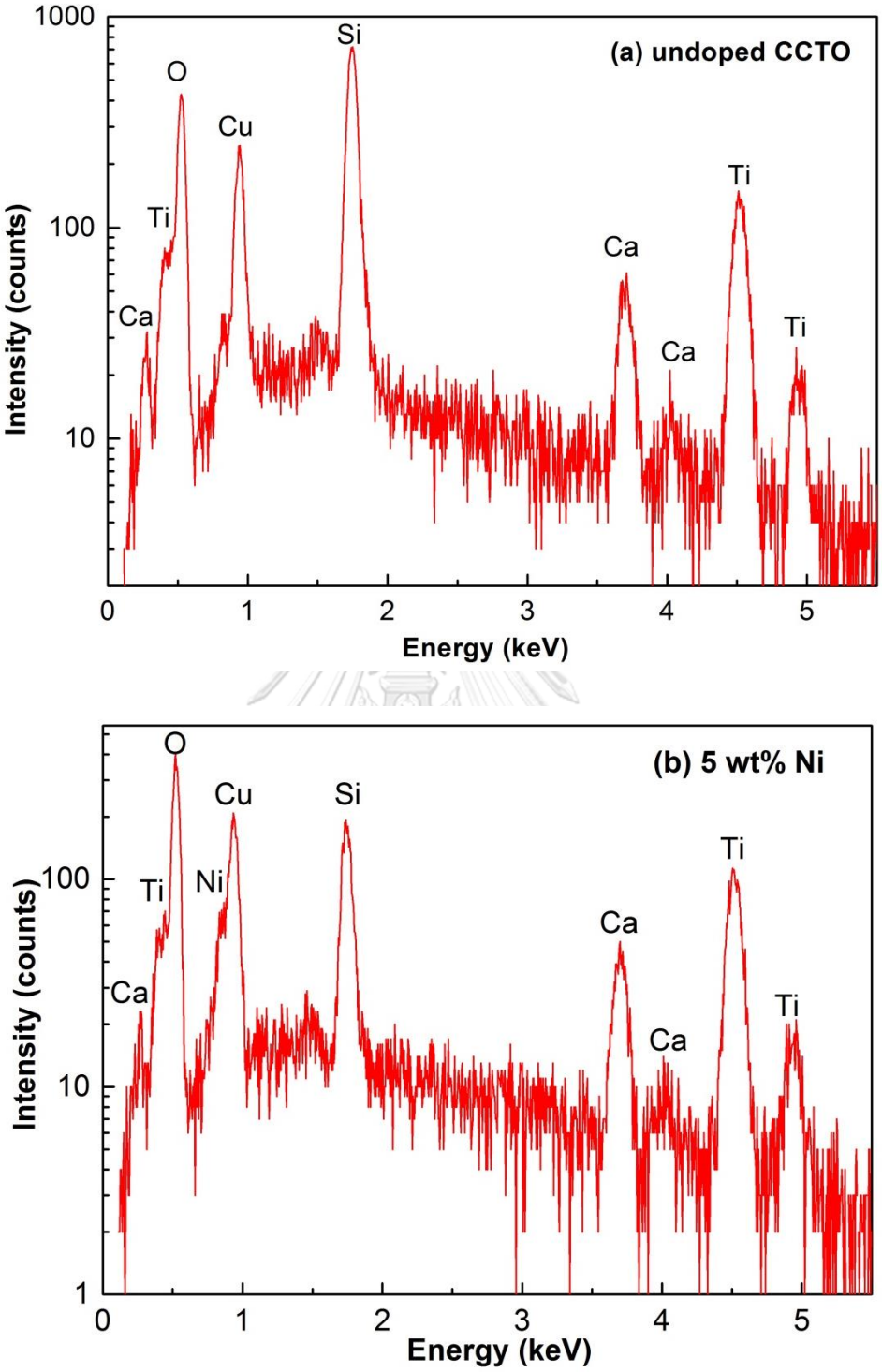

Figure 5.17: EDX spectra of (a) undoped CCTO thin film and (b) 5 wt% Ni-doped CCTO thin film prepared by nickel acetate.

Table 5.4: The concentrations of elemental composition by weight% and atom% of undoped and Ni-doped CCTO films on silicon substrate prepared by nickel (II) acetate.

Element	undoped CCTO (Weight%)	1 wt% Ni-doped CCTO (Weight%)	2 wt% Ni-doped CCTO (Weight%)	3 wt% Ni-doped CCTO (Weight%)	4 wt% Ni-doped CCTO (Weight%)	5 wt% Ni-doped CCTO (Weight%)
Ca	9.01	7.48	7.18	7.92	7.5	8.69
Cu	11.95	14.3	12.38	21.69	18.35	17.77
Ti	43.38	40	42.01	35.08	37.12	35.31
O	35.65	37.48	37.17	32.85	33.46	34.34
Ni	0	0.74	1.26	2.46	3.56	3.89

Element	undoped CCTO (Atom%)	1 wt% Ni-doped CCTO (Atom%)	2 wt% Ni-doped CCTO (Atom%)	3 wt% Ni-doped CCTO (Atom%)	4 wt% Ni-doped CCTO (Atom%)	5 wt% Ni-doped CCTO (Atom%)
Ca	6.34	5.18	4.98	5.87	5.5	6.29
Cu	5.3	6.25	5.42	10.14	8.49	8.12
Ti	25.53	23.19	24.39	21.76	22.78	21.39
O	62.82	65.04	64.61	60.99	61.45	62.28
Ni	0	0.35	0.59	1.25	1.78	1.92

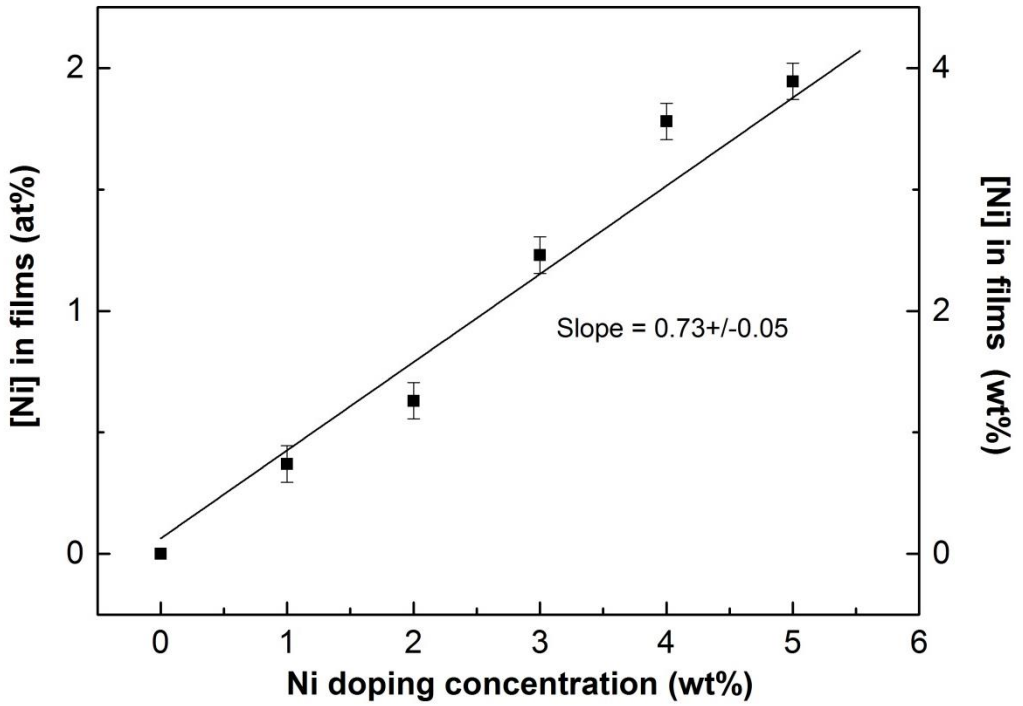

Figure 5.18: The plot of measured Ni doping concentrations obtained by EDX measurement and the concentration of Ni in precursor solutions prepared by nickel (II) acetate.

5.10 The characterization of oxidation state of 5 wt% Ni-doped CCTO films prepared by nickel (II) acetate

X-ray photoelectron (XPS) spectra of 5 wt% Ni-doped CCTO thin film on silicon substrate are presented in Fig. 5.17. XPS measurements were done in the laboratory sponsored by Thailand Center of Excellence in Physics. Different elements namely O, Ca, Cu, Ti and Ni were found in XPS survey spectra in Fig. 5.17(a). In Fig. 5.17(b), O 1s core level spectra consist of substitutional oxygen and chemisorbed oxygen at 529.6 and 531.6 eV, respectively [22]. The Ca 2p XPS spectrum of the film are shown in Fig. 5.17(c). The binding energies of Ca $2p_{1/2}$ and Ca $2p_{3/2}$ are 350 eV at 346.5 eV, respectively and these peaks are assigned to Ca^{2+} in the films [47, 48]. For the core level of Cu 2p, there are four binding energies observed shown in Fig. 5.17(d). The Cu $2p_{1/2}$ and Cu $2p_{3/2}$ peaks located at 954.0 and 933.9 eV, respectively are corresponded to copper in 2+ oxidation state and an appearance of satellite peaks are at 962.2 and 942.2 eV, respectively [49, 50]. In case of titanium spectrum, Ti $2p_{3/2}$ and Ti $2p_{1/2}$ peaks from the spin orbit doublets are at 458.4 eV and 464.2, respectively for which Ti is present in a chemical state of 4+ as seen in Fig. 5.20(e) [52]. Finally, core level of Ni 2p can be observed four peaks shown in Fig. 5.17(f) at which the main peaks are Ni $2p_{1/2}$ and Ni $2p_{3/2}$ [25, 53, 54]. The Ni $2p_{1/2}$ and Ni $2p_{3/2}$ peaks are located at 873.1 eV and 855.5 eV, respectively along with their satellite peaks at 879.6 and 861 eV, respectively [25, 53]. These peaks are attributed to Ni^{2+} in the film. It could be concluded that XPS results confirm the evidence of Ni atom presence in the doped films similar to EDX results.

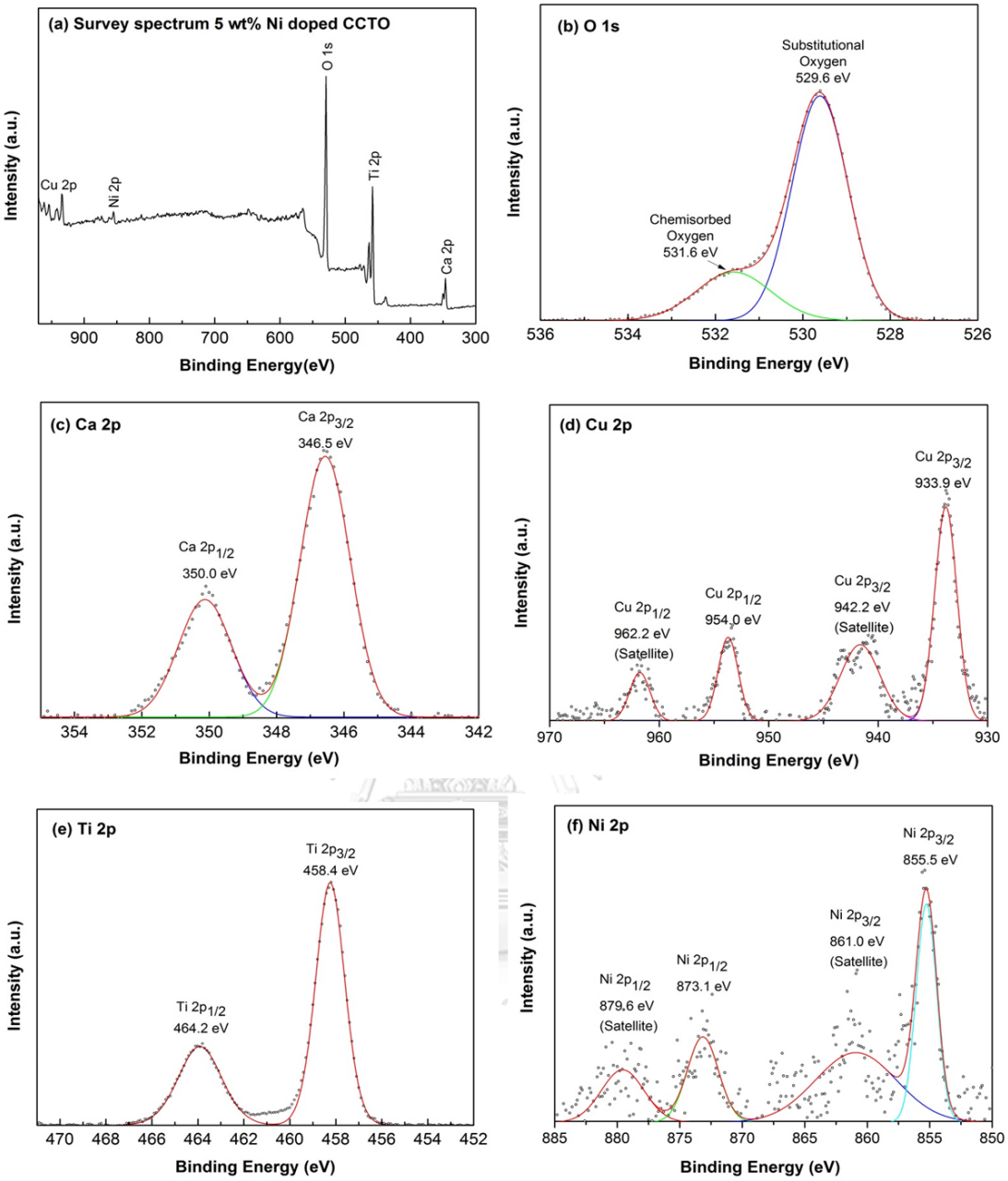

Figure 5.19: XPS spectra of 5 wt% Ni-doped CCTO film on silicon substrate.

5.11 Characterization of the gas sensor properties of undoped CCTO films and Ni-doped CCTO films prepared by nickel (II) acetate

Fig. 5.18(a) shows the sensor response towards H_2S dependent on the operating temperature range of 150-350 °C. It can be seen that the sensor response of films increases with the operating temperature up to 300 °C. Then, the sensor response is reduced after 300 °C. From the sensor curve of H_2S, the undoped and Ni-doped CCTO films were suggested that the optimum temperature for H_2S detection is 300 °C. This operating temperature is slightly higher than that of the results obtained from the CCTO films prepared by NiO (operating temperature at 250 °C.). In addition, it can be seen that the sensor response increases with increasing H_2S concentration as presented in Fig. 5.18(b). However, the increasing of the response for this set of films is more dramatic than that of the films prepared by NiO. The 5 wt% Ni-doped CCTO film presented the maximum sensor response of 175 at 10 ppm H_2S while the undoped CCTO exhibited the sensor response of 10.

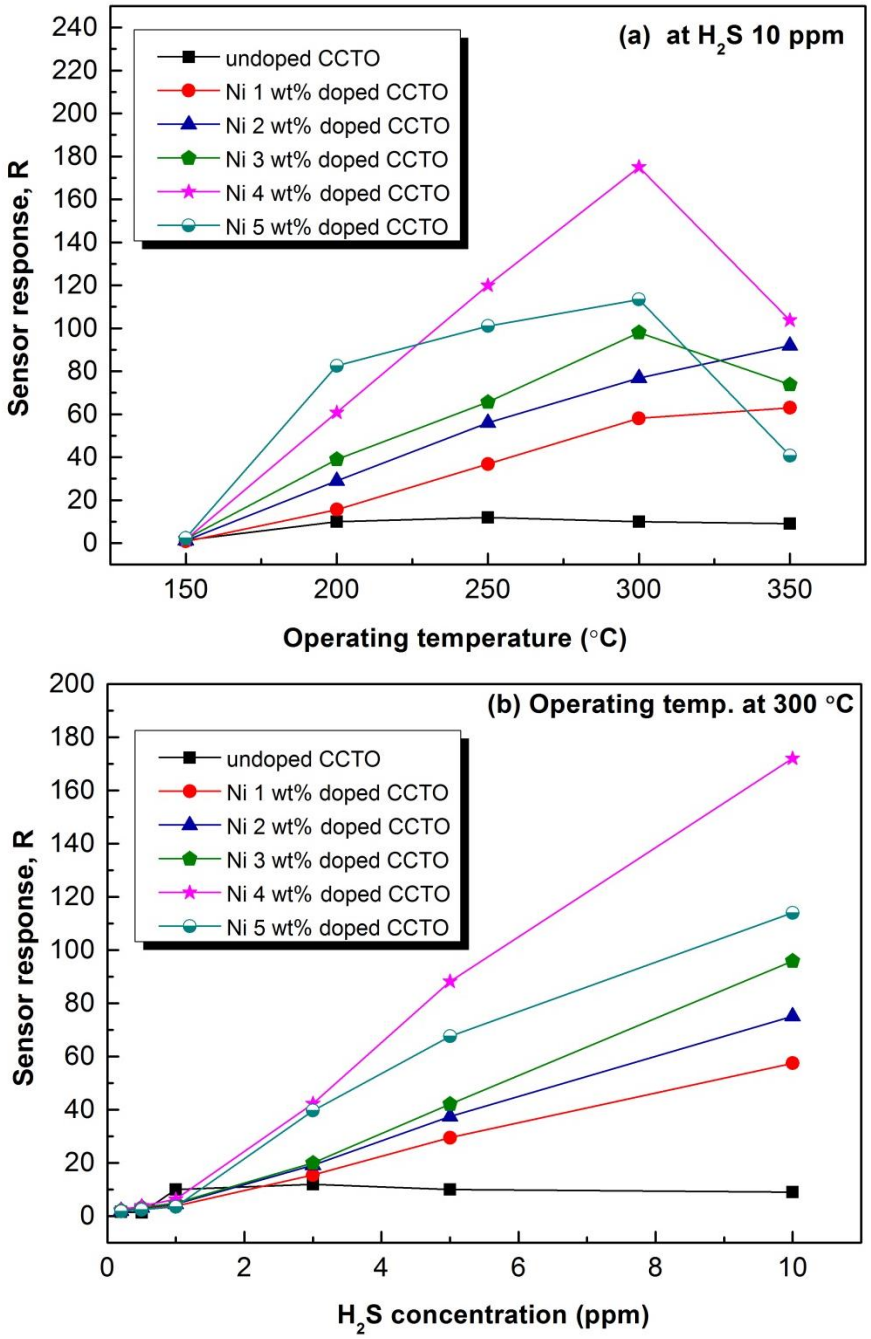

Figure 5.20: (a) Sensor response of films as function of temperature towards10 ppm H_2S and (b) sensor response as function of H_2S concentrations at 300 °C.

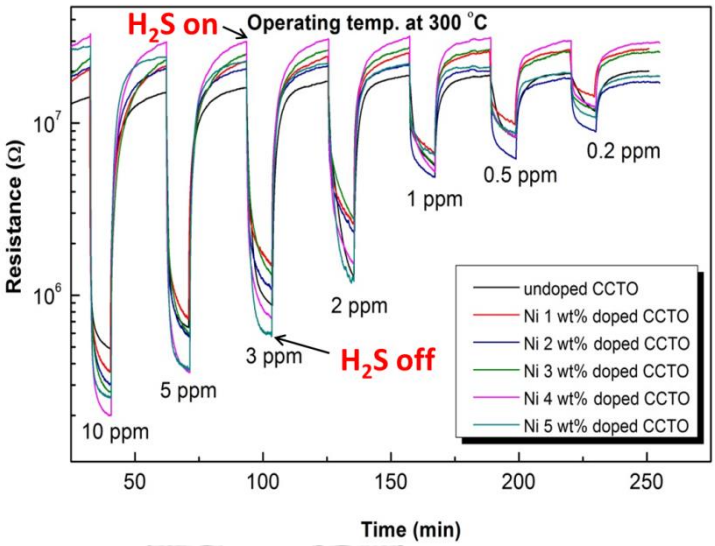

Figure 5.21: Resistance curve of Ni-doped CCTO sensors prepared by nickel acetate as function of time under exposure to 0.2-10 ppm H_2S concentrations at 300 ºC.

Fig. 5.19 shows resistance curve of undoped and Ni-doped sensors exposure to H_2S at different concentrations at 300 ºC. Under air atmosphere, the resistance of undoped and Ni-doped CCTO sensors prepared by nickel acetate is 10^7-10^8 (Ω) and it was reduced when H_2S was flown into the chamber. Therefore, the behavior of these films behaves like an n-type semiconductor. Furthermore, Ni-doping concentration affects the changing in resistance. The reduction in the resistance is more seen in the films with more Ni doping concentrations. Surprisingly, a maximum change of resistance was observed for 4 wt% Ni-doped CCTO under 10 ppm H_2S.

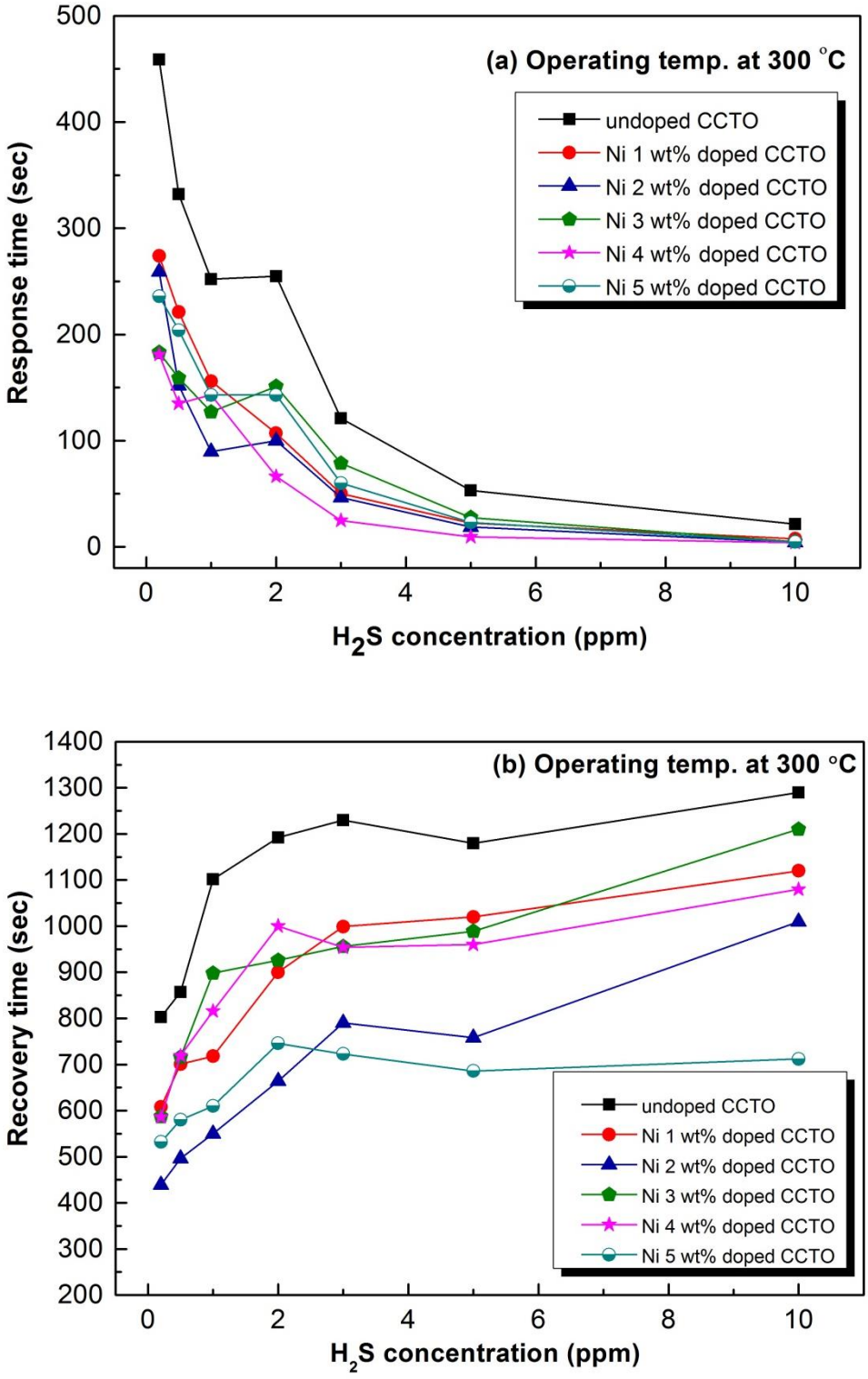

Figure 5.22: (a) Response time curve and (b) recovery time curve of Ni-doped CCTO sensors prepared by nickel acetate in the range of 0.2 -10 ppm H_2S concentrations at 300 °C.

The dependence of the response time of undoped and Ni-doped CCTO films and H_2S concentrations is shown in Fig. 5.20(a). It can be observed that the response time of the films shows the decreasing as increasing H_2S concentrations up to 10 ppm H_2S. Firstly, the response time shows a dramatic drop up to 5 ppm and then shows a slow drop up to 10 ppm due to the saturation of gas absorption dynamic at high H_2S concentration. Moreover, it can be seen that the Ni-doped CCTO films showed the response time smaller than that of undoped CCTO film. For example, the response time of the 4 wt% Ni-doped CCTO operated at 300 °C to 10 ppm H_2S presented highest sensor response was found to decrease to 4 s from ~ 20 s which is the response time of the undoped film operated at the same gas testing conditions. Fig. 5.20(b) shows the recovery time of the film sensors under various H_2S concentration at 300 °C. The recovery time increases with increasing H_2S concentrations. The undoped CCTO and the 4 wt% Ni-doped CCTO exhibited recovery time of ~1300 and ~1000 s, respectively. The desorption of H_2S from the CCTO film surface is quite slow yielding the large recovery time after the exposure to NO_2 gas. The recovery time of Ni doped CCTO is less than that of undoped CCTO. Therefore, it could be concluded that Ni doping using nickel acetate in the Ni-doped CCTO film preparation improves both recovery and response times of the sensors.

Table 5.5: The sensor response of films under tasted different gases namely, H_2S, NO_2 H_2, NH_3 and ethanol gas.

Ni-doping concentration (wt%)	Sensor response, R				
	H_2S (10 ppm)	NO_2 (5 ppm)	H_2 (30000 ppm)	NH_3 (2000 ppm)	Ethanol (2000 ppm)
undoped	10	1.26	1.5	1.27	1.6
1	58.1	4.98	1.6	1.16	3.99
2	76.8	10.4	1.06	2.6	4.58
3	98	2.83	1.43	1.41	4.11
4	175	3.48	1.04	1.62	2.18
5	113.4	3.05	1.45	1.18	4.2

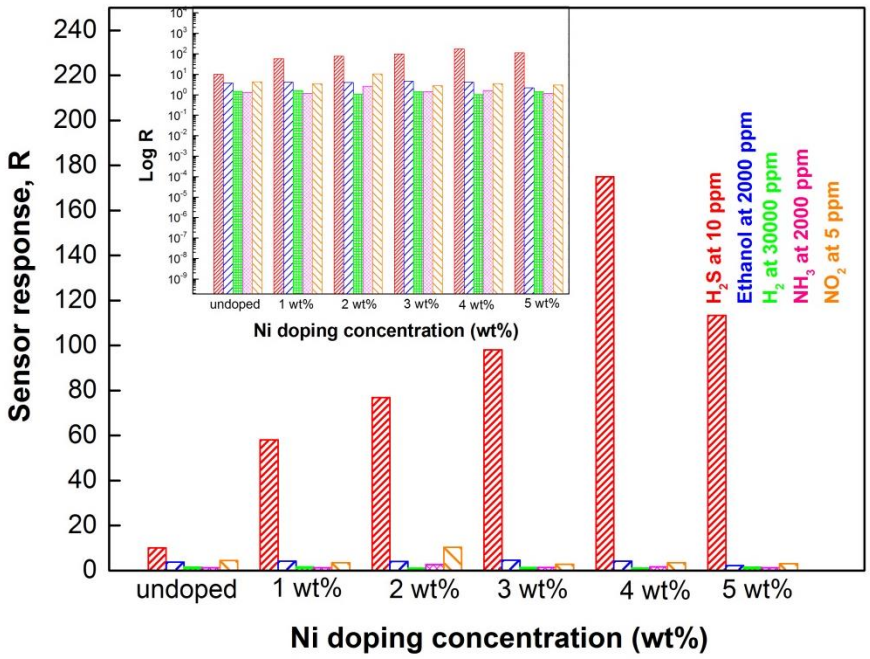

Figure 5.23: Selectivity of undoped and Ni-doped CCTO sensors prepared by nickel acetate towards various tested gases.

The gas sensor response to various tested gases (NO_2, H_2, NH_3, H_2S and ethanol gas) at 300 ºC is compared as seen Fig. 5.21. The undoped and Ni-doped CCTO films appeared poor sensor response towards NO_2, H_2, NH_3 and ethanol gas but they performed the best sensor response towards H_2S. The trend of H_2S concentrations is clear that the sensor response increase with increasing H_2S concentrations except for 5 wt%. The 4 wt% Ni-doped CCTO sensors exhibit the highest response of 175 under 10ppm H_2S, while the sensor response towards NO_2, H_2, NH_3 and ethanol gas is 3, 1, 2 and 2, respectively. It is clearly to conclude that Ni-doped CCTO film sensors prepared by nickel acetate illustrated better sensor response than that of the films prepared by nickel oxide whereas the selectivity towards H_2S is not better (see the comparison between Fig. 5.12 and Fig. 5.21). As seen in Fig. 5.22, the resistance changes of undoped and Ni-doped CCTO films prepared by nickel acetate after exposure to NO_2 is not that much. Therefore, the result from Y. Wang et al. [28] and the undoped and Ni-doped CCTO films prepared by nickel oxide is better.

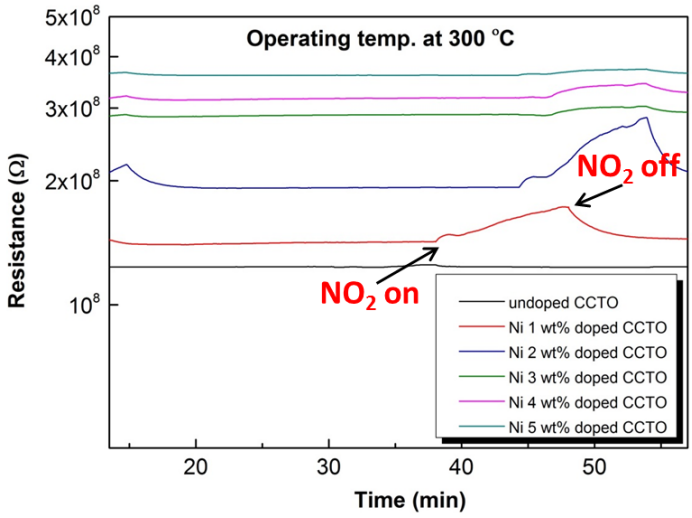

Figure 5.24: The resistance change of undoped and Ni-doped CCTO films prepared by nickel acetate exposed to 5 ppm NO_2 concentration.

5.11 Gas sensing mechanism for H_2S and NO_2

In this section, I will explain gas sensing mechanism of Ni-doped CCTO sensors upon the exposure to H_2S and NO_2. Undoped CCTO and Ni-doped CCTO films prepared by NiO and Ni acetate are n-type semiconductor oxide. As known H_2S is the reducing gas while NO_2 is the oxidizing gas. Their gas sensing mechanisms are discussed as the following:

1. The effect of surface reactions between adsorbed oxygen and tested gas

The principle of metal oxide gas sensor depends upon the oxygen concentration and its rate of adsorption and desorption. Oxygen molecules from the atmosphere are absorbed on the surface of the sensor and act as an electron acceptors and then get ionized to become adsorbed oxygen species (O_2^-, O^-) on the surface. Below the temperature of 200 °C, O_2 can accept one electron from the metal oxide surface to become O^-, and above 200 °C, it can accept two to become O^- according to Equation (2.14)-(2.17) in section 2.3.2. In this case, the sensor response of CCTO sensor was measured at 150-250 ºC. Therefore, the absorbed oxygen in ionic forms on the film surface become both types of oxygen species (O_2^-, O^-). During the adsorption process, the width of space charge region increases and hence the height of potential barrier increases. This reduces the conduction of electron between the grains.

As described in section 2.3.1, Equation (2.13) describes the adsorption process in the case of oxygen deficient sites on the metal oxide surface. Oxygen molecules from the ambient diffuse to the oxygen vacant sites in metal oxide surface by extracting free electrons. Thus, the chemisorption of oxygen molecules reduces the mobility of electrons leading to reduction in conductance in n-type materials

As the sensor is exposed to H_2S, the adsorbed oxygen species react with H_2S. The reaction between adsorbed O^{2-} and H_2S are shown in Equation (5.1) – (5.2) [18]. The reaction releases a large number of electrons into the conduction band along with the bi-product of sulfur dioxide (SO_2) and water vapor (H_2O), so the enhancements of electron into conduction lead to the reduction of resistance. This reaction often happens in dense oxygen atmosphere.

$$2H_2S_{adsorbed} + 3O^-_{2\ adsorbed} \xrightarrow{k_1} 2SO_2 + H_2O + 3e^- \quad (5.1)$$

$$H_2S_{adsorbed} + 3O^{2-}_{adsorbed} \xrightarrow{k_2} SO_2 + H_2O + 6e^- \quad (5.2)$$

$$5O^x_{lattice} + H_2S_{adsorbed} \xrightarrow{k_3} SO_4^{2-} + H_2O + 3V_O^{\bullet\bullet} + 6e^- \quad (5.3)$$

At low partial pressure of oxygen, H_2S directly reacts with electrically neutral oxygen atoms in their lattice (O_O^x) to form SO_4 and produces the oxygen vacancy ($V^{\bullet\bullet}$) in the surface of the metal oxide which leads to increase in the conductance seen in Equation (5.3).

Nitrogen dioxide (NO_2) which is a highly toxic and strong oxidizing gas can react with metal oxide surface both in the presence and absence of oxygen as seen in Equations (5.4)-(5.6). In the presence of oxygen, the absorption of oxygen from the air atmosphere on the film surface creates the absorbed oxygen species (O_2, O_2^-). Then, NO_2 (oxidizing gas) was injected into chamber and the adsorbed oxygen species react with NO_2 on films surface as presented in Equations (5.4)-(5.5) [28]. In addition, NO_2 can be directly interacted with electron from conduction band of film as shown in Equation (5.3) [27, 55]. The reaction between O_2^- and NO_2 and the interaction between NO_2 and the electron from conduction band lead to the reduction of conduction electrons in the conduction band. The reduction of electron affects the increasing in the resistance of film.

$$NO_{2\,(g)} + e^-_{(surface)} \rightarrow NO^-_{2\,(adsorbed)} \quad (5.3)$$

$$NO_{2\,(adsorbed)} + O^-_{2\,(adsorbed)} + 2e^-_{(surface)} \rightarrow NO^-_{2\,(adsorbed)} + 2O^-_{(adsorbed)} \quad (5.4)$$

$$NO_{2\,(adsorbed)} + O^- \rightarrow NO^+_{(adsorbed)} + 2O^-_{(adsorbed)} \quad (5.5)$$

The desorption of NO_2 is limiting at the decomposition of the NO_2 on the film surface, which is determined by the large recovery time (~ 720 s) after the exposure to NO_2 gas and the response time is approximately 510 s.

2. The effect of reaction between Ni-dopant and H_2S gas.

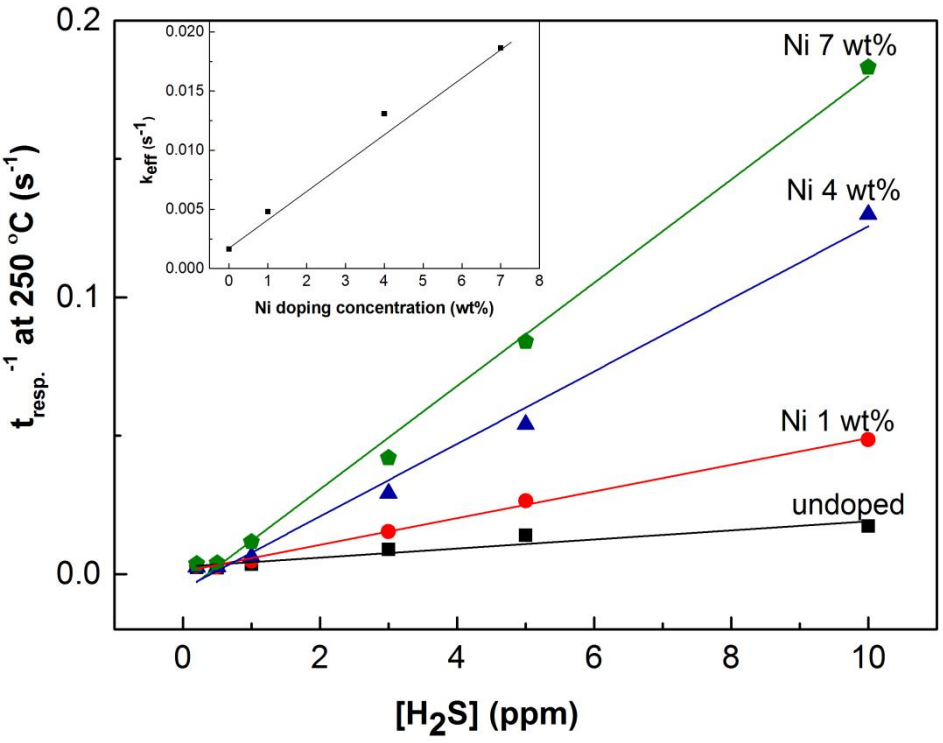

Figure 5.25: Specific response rate of undoped and Ni-doped CCTO films prepared by NiO as a function of H_2S concentrations at 250 ºC and inset; the linear fit of the specific response rate as function of Ni-doping concentrations.

Figure 5.27 shows that the response rates are approximately linear functions of the H_2S gas concentration at all Ni-doping levels, which suggests that a first order kinetics on H_2S dominates the 10/90% portion of the sensing response. This representation allows identifying the specific dependence of the response rate on the Ni-doping. Thus we refer to the slopes of the linear functions in Fig. 5.37 as the effective response rates (k_{eff}). A plot of k_{eff} versus the Ni-doping concentration allows us to estimate the reaction order in the catalyst as shown in the inset on Fig. 5.27. The observed linear dependence on the Ni-doping is indicative of a first order catalytic effect. In the light of the reactions stated in Eqs. (5.1)-(5.3), Fig. 5.27 suggests that in the rate limiting step an H_2S molecule interacts with a single Ni^{2+} ion. The six-electron oxidation of a single H_2S molecule necessarily occurs sequentially on going from S^{2-} , passing through S^0 and continuing all the way to S^{4+} before desorption of the final product SO_2 gas. Since the oxidation of S^0 into SO_2 is a very exothermic process it is not likely to be the rate limiting step. Instead, the formation of elementary sulfur from H_2S is far more likely to become the rate limiting process. Thus, a possible mechanistic explanation for these results is represented on Fig. 5.27. The first step represents the sensor in the standby situation, under air atmosphere. Upon introducing H_2S gas, steps 2-5 take place. In step 2, H_2S molecules adsorb on the Ni-doped CCTO surface at sites where Ni^{2+} ion is present, possibly by substitution of one of the oxygen ligands and forming a sulfide ion plus a water molecule. At this point, two electrons are transferred from the sulfide ion to the Ni^{2+} ion which becomes formally a Ni^0 state and producing an adsorbed sulfur atom.

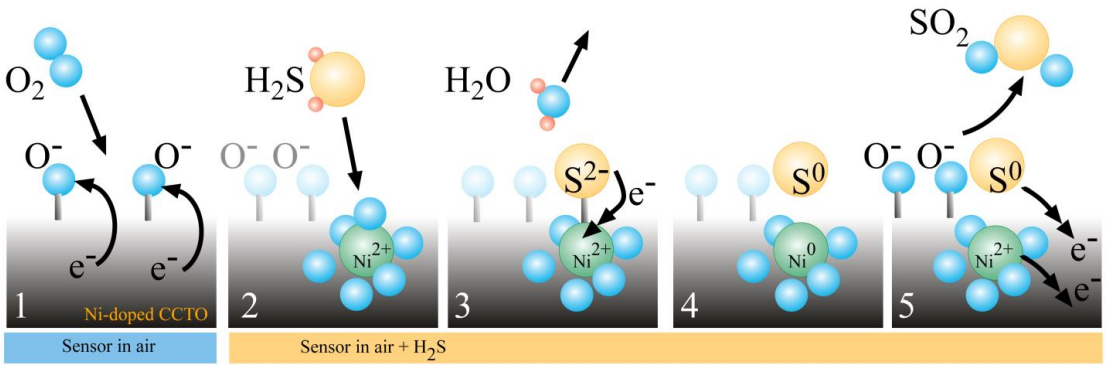

Figure 5.26: Schematic representation of the proposed operation mechanism of the Ni-doped CCTO gas sensor.

Subsequently charge injection into the conduction band restores the Ni^{2+} state. The final stage of oxidation of elemental sulfur into SO_2 gas further contributes with electron injection. The electrons transferred to the conduction band of the CCTO neutralizes the charge depletion caused initially by reactions stated in Eqs. (2.13) and (2.16) and rise the Fermi level in the material, resulting in higher conductivity of the gas sensor. Being a relatively noble metal, Ni supports the +2 and 0 oxidation states which can interconvert relatively easily, thus facilitating the 2-electron oxidation of H_2S as well as the return to the +2 state while the sensor is in the standby condition under air. The small response of undoped CCTO towards H_2S is likely due to a similar role played by copper. A hint to a likely explanation of the higher ability of nickel in the sensing response may be found in the free energies of formation of the oxides and sulfides of copper and nickel. On one hand, copper has more tendency to become oxidized, being the formation of CuO more exergonic (ΔG^0_f = -372 kJ/mole) than that for NiO (ΔG^0_f = -213 kJ/mole). On the other hand, sulfide is more stable than copper sulfide ($\Delta G^0_{f(NiS)}$ = -90 kJ/mole and $\Delta G^0_{f(CuS)}$ = -49 kJ/mole). Thus, Ni-doping

improves the CCTO film sensor response by facilitating the binding and subsequent oxidation of sulfide species.

CHAPTER VI

CONCLUSION

In this thesis work, the effects of Ni-doping concentrations in nickel doped calcium copper titanate thin films to their gas sensing properties were studied. Nickel oxide (NiO) and nickel (II) acetate were used as doping compounds in the CCTO films preparation process. Ni-doping concentrations of the films prepared by NiO were 0, 1, 4, and 7 wt%. The highest Ni-doping concentration that NiO can be completely dissolved is 7 wt%, and if more than 7 wt% the viscosity of the precursor became very high due to the saturation. In the case of Ni-doped CCTO films prepared by nickel (II) acetate, the films were doped with 0, 1, 2, 3, 4 and 5 wt% Even in the process of synthesis Ni-doped CCTO synthesis, nickel (II) acetate could be add more than 0.5385 g for making 5 wt% Ni-doping concentration batch. However, the 5 wt% Ni-doping concentration is maximum that was interested in this thesis work. Then, the deposition process of films was done on silicon (Si (100)) and alumina (Al_2O_3) substrates. The characterizations and gas sensing properties of undoped and Ni-doped CCTO films will be concluded as follows:

Topic 1: The undoped and Ni-doped CCTO films prepared by NiO.

As known, the atomic radius of Ni (149 pm) is close to the atomic radius of Ti (176 pm). In the precursor preparation, we calculated the amounts of titanium (IV) isopropoxide and nickel oxide based on the substituting Ni atoms into Ti sites (see in Appendix A). XRD patterns of undoped and Ni-doped CCTO films on silicon and alumina substrates showed the main peaks of CCTO corresponding to the

characteristic (220), (400) and (422) planes. This can be confirmed that the crystal structure of Ni-doped CCTO films is still perovskite cubic as seen in undoped CCTO film and the calculated lattice parameters of the films are slightly lower than bulk CCTO. However, there is only a small amount of impurity phase of rutile TiO_2 and there are no other nickel oxides or impurity phases involved with nickel. Overall undoped CCTO film shows the sharp CCTO peaks with high intensity compared to those of Ni-doped CCTO films. The shift of CCTO peaks among these films is not observed, and this is could be due to the comparable of atomic radius of nickel and titanium atoms. From FESEM images, the surface morphologies of all films exhibited granular particles on both types of substrate but the cluster forms can be especially seen only on the surface of 4 wt% and 7 wt% Ni-doped CCTO films on alumina substrates. Due to the roughness of alumina substrate, the obtained film thickness is fluctuated compared to the films on silicon. The size of granular particles is smaller as the doping level is higher. Also the granular particles of films on alumina substrate are slightly smaller than those found in the films on silicon substrates. In general, for both cases of substrate used, surface morphologies of 7 wt% Ni-doped CCTO film exhibited the highest porosity compared to that of undoped, 1 wt% and 4 wt% Ni-doped CCTO films. Chemical elements (Calcium (Ca), copper (Cu), titanium (Ti), oxygen (O) and nickel (Ni)) of undoped and Ni-doped CCTO films deposited on silicon substrates were confirmed by EDX analysis but nickel (Ni) signal was only observed in Ni-doped CCTO films. The measured Ni doping concentrations increase with increasing the Ni-doping concentration in precursor solutions whereas the measured Ti concentrations in the films decrease. This is caused by the substitution of Ni atoms into Ti sites and this means the substituting of Ni increases with increasing

Ni-doping concentrations. These results confirmed that Ni is doped into the Ni-doped CCTO films. The appearance of the bonding of Ni atom with other atoms in CCTO structure was also confirmed with Raman spectra. The nickel in +2 oxidation state is evidenced from by XPS analysis. Gas sensing properties of undoped and Ni-doped CCTO films were measured towards different types of gases (NO_2, H_2, NH_3, H_2S and ethanol) under operating temperature of 150 -350 °C. The films exhibited an excellent sensor response towards H_2S against NH_3 and ethanol gas and moderate sensor response toward NO_2 at 5 pmm. Moreover, Ni-dopants in the films acting as a catalyst improve much better sensor responses. The H_2S gas sensing responses of the Ni-doped CCTO films were clearly enhanced with Ni doping concentration. The 7 wt% Ni-doped CCTO film presented the highest sensor response of 112 towards 10 ppm of H_2S at 250 °C. This highest value was twelve times better than that of undoped CCTO film. Another good gas sensing property is that the response time of Ni-doped CCTO films exposure to H_2S is smaller than the undoped CCTO. The recovery time of 7 wt% Ni-doped CCTO sensor operated at 10 ppm H_2S was found to be the maximum at ~1220 s.

Topic 2: The undoped and Ni-doped CCTO films prepared by Ni (II) acetate.

The XRD, EDX and XPS results of the undoped and Ni-doped CCTO films prepared by Ni (II) acetate are similar to the results obtained from films prepared by NiO. Gas sensing measurements were performed. The doped films illustrated the best selectivity toward H_2S compared to NH_3, ethanol gas, H_2 and NO_2 and the second best selectivity is toward NO_2. However, the selectivity toward only H_2S is not the best compared to Ni-doped CCTO films prepared NiO. The resistance changes of undoped

and Ni-doped CCTO films prepared by nickel acetate after exposure to NO_2 is not that much. Ni-doped films showed higher sensor response, shorter response and recovery times than those of the undoped film under H_2S at 300 °C. Therefore, Ni doping using NiO and nickel acetate in the Ni-doped CCTO film preparation improves sensor response, recovery and response times of the sensors. Moreover, surface morphologies such high porosity and high roughness affect to better gas sensing properties.

Topic 3: Comparison the gas sensing properties of the resulting Ni-doped CCTO film sensors with the other materials.

Table 6.1: The gas sensing properties of various materials**.**

Types of film	Sensor response (H_2S)	Response time (s)	Recovery times (s)	Operating temperature (°C)	Types of selectivity gas	References
undoped CCTO	12	58	1240	250	H_2S	This work
undoped CCTO	10	20	1300	300	H_2S	This work
7 wt% Ni-doped CCTO prepared by NiO	112 at 10 ppm	5	1220	250	H_2S, NO_2	This work
4 wt% Ni-doped CCTO prepared by Nickel (II) acetate	175	4	1080	300	H_2S, NO_2 but the selectivity towards H_2S is not the best	This work

Table 6.1: The gas sensing properties of various materials. (cont)

Types of film	Sensor response (H_2S)	Response time (s)	Recovery times (s)	Operating temperature (°C)	Types of selectivity gas	References
CuO-NiO core-shell microspheres	35 at 100 ppm	-	-	300	H_2S, NO_2 with comparable results	[28]
9 wt% Fe-doped CCTO	126	8.5	500	250	H_2S	[22]
0.9 wt% Ag-doped CCTO	98.7	2.96	894	250	H_2S with the best selectivity	The work done by Aukrit [56]

Comparison of gas sensing properties with various materials was shown in Table 6.1. It is clearly to conclude that Ni-doped CCTO film sensors prepared by nickel acetate illustrated better sensor response value, selectivity and shorter response-recovery time than those of Ni-doped CCTO prepared by NiO. In addition, the optimum operating temperature of film prepared by NiO is lower than film prepared by nickel acetate. Normally, researchers are looking for ideal sensors that could operate at room temperature or near room temperature. Moreover, the best sensor response of Ni-doped CCTO film sensors prepared by both nickel oxide and nickel acetate towards H_2S is better than that of CuO-NiO core-shell microspheres. However, the worse thing about Ni-doped CCTO sensor is that the response time is very long compared to other materials. Figure 6.1 show histograms of log sensor response of different types sensor exposure to various gases and ratio between sensor response of H_2S and NO_2 which can identify the selectivity of the gas sensor. The Fe-

doped CCTO films illustrated the highest ratio which refer to the highest selectivity compared to other materials. Ni-doped CCTO films prepared by nickel (II) acetate exhibited the selectivity more than that Ag-doped CCTO films and Ni-doped CCTO films prepared by NiO. The selectivity of Ni-doped CCTO films prepared by NiO is least. However, it was found in this study that Ni-doped CCTO prepared by NiO is a good candidate for developing a gas sensor towards a toxic gas group besides H_2S.

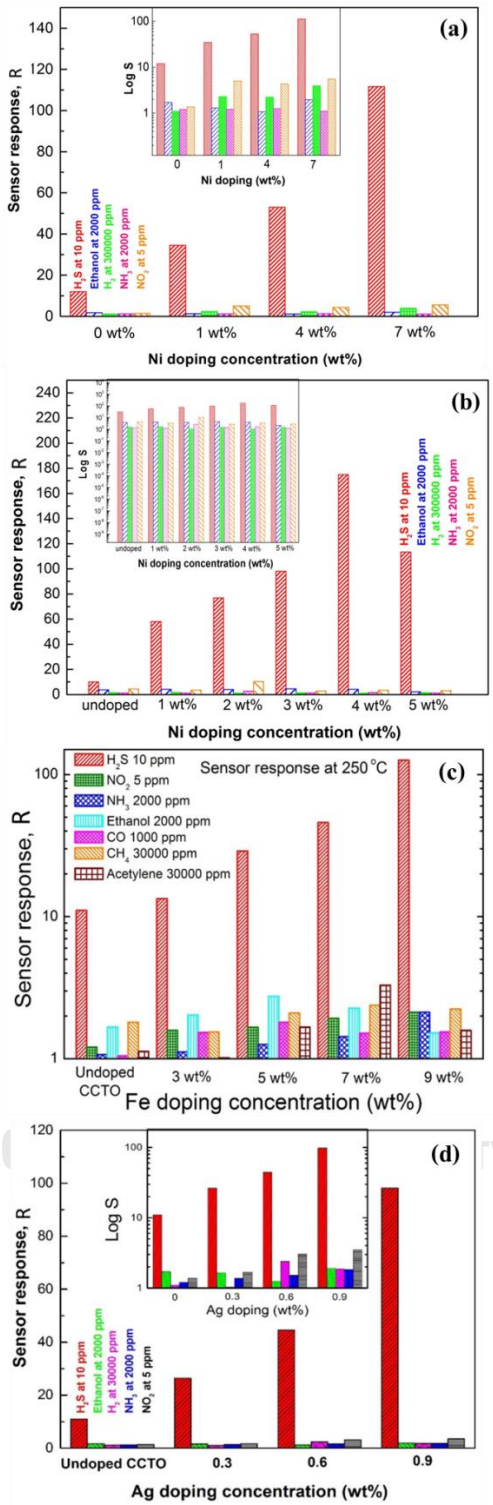

$\frac{R_{H_2S}}{R_{N_2O}}$ = 20.22

$\frac{R_{H_2S}}{R_{N_2O}}$ = 37.18

$\frac{R_{H_2S}}{R_{N_2O}}$ = 59.58

$\frac{R_{H_2S}}{R_{N_2O}}$ = 28.20

Figure 6.1: Histograms of sensor response of (a) 7 wt% Ni-doped CCTO prepared by NiO, (b) 4 wt% Ni-doped CCTO prepared by nickel (II) acetate, (c) 9 wt% Fe-doped CCTO and (d) 0.9 wt% Ag-doped CCTO exposure to various gases.

REFERENCES

[1] L. Singh, U.S. Rai, K.D. Mandal, N.B. Singh, Progress in the growth of $CaCu_3Ti_4O_{12}$ and related functional dielectric perovskites, Progress in Crystal Growth and Characterization of Materials, 60 (2014) 15-62.

[2] W. Yang, S. Yu, R. Sun, R. Du, Nano- and microsize effect of CCTO fillers on the dielectric behavior of CCTO/PVDF composites, Acta Materialia, 59 (2011) 5593-5602.

[3] L. Feng, Y. Wang, Y. Yan, G. Cao, Z. Jiao, Growth of highly-oriented $CaCu_3Ti_4 O_{12}$ thin films on $SrTiO_3$ (1 0 0) substrates by a chemical solution route, Applied Surface Science, 253 (2006) 2268-2271.

[4] P. Mishra, P. Kumar, Structural, dielectric and optical properties of [(BZT–BCT)-(epoxy-CCTO)] composites, Ceramics International, 41 (2015) 2727-2734.

[5] I.-D. Kim, A. Rothschild, T. Hyodo, H.L. Tuller, Microsphere Templating as Means of Enhancing Surface Activity and Gas Sensitivity of $CaCu_3Ti_4O_{12}$ Thin Films, Nano Letters, 6 (2006) 193-198.

[6] E. Joanni, R. Savu, P.R. Bueno, E. Longo, J.A. Varela, P-type semiconducting gas sensing behavior of nanoporous rf sputtered $CaCu_3Ti_4O_{12}$ thin films, Applied Physics Letters, 92 (2008) 132110.

[7] R. Parra, R. Savu, L.A. Ramajo, M.A. Ponce, J.A. Varela, M.S. Castro, P.R. Bueno, E. Joanni, Sol–gel synthesis of mesoporous $CaCu_3Ti_4O_{12}$ thin films and their gas sensing response, Journal of Solid State Chemistry, 183 (2010) 1209-1214.

[8] M. Ahmadipour, M.F. Ain, Z.A. Ahmad, A Short Review on Copper Calcium Titanate (CCTO) Electroceramic: Synthesis, Dielectric Properties, Film Deposition, and Sensing Application, Nano-Micro Letters, 8 (2016) 291-311.

[9] J.-C. Ding, H.-Y. Li, T.-C. Cao, Z.-X. Cai, X.-X. Wang, X. Guo, Characteristics and sensing properties of CO gas sensors based on $LaCo_{1-x}$ Fe_xO_3 nanoparticles, Solid State Ionics, 303 (2017) 97-102.

[10] L. Huo, X. Yang, Z. Liu, X. Tian, T. Qi, X. Wang, K. Yu, J. Sun, M. Fan, Modulation of potential barrier heights in Co_3O_4/SnO_2 heterojunctions for highly H_2-selective sensors, Sensors and Actuators B: Chemical, 244 (2017) 694-700.

[11] S. Xu, K. Kan, Y. Yang, C. Jiang, J. Gao, L. Jing, P. Shen, L. Li, K. Shi, Enhanced NH_3 gas sensing performance based on electrospun alkaline-earth metals composited SnO_2 nanofibers, Journal of Alloys and Compounds, 618 (2015) 240-247.

[12] X. Gao, Y. Sun, C. Zhu, C. Li, Q. Ouyang, Y. Chen, Highly sensitive and selective H_2S sensor based on porous $ZnFe_2O_4$ nanosheets, Sensors and Actuators B: Chemical, 246 (2017) 662-672.

[13] X. Cui, Y. Xu, X. Zhang, X. Cheng, S. Gao, H. Zhao, L. Huo, In-situ deposited flower-like Bi_2MoO_6 microspheres thin film based sensors for highly selective detection of ppb-level H_2S at low temperature, Sensors and Actuators B: Chemical, 247 (2017) 681-690.

[14] C.D. Parker, Mechanics of Corrosion of Concrete Sewers by Hydrogen Sulfide, Sewage and Industrial Wastes, 23 (1951) 1477-1485.

[15] M.F. Struve, J.N. Brisbois, R. Arden James, M.W. Marshall, D.C. Dorman, Neurotoxicological Effects Associated with Short-Term Exposure of Sprague–Dawley Rats to Hydrogen Sulfide, NeuroToxicology, 22 (2001) 375-385.

[16] C. Balamurugan, Y.J. Jeong, D.W. Lee, Enhanced H_2S Sensing Performance of a p-type Semiconducting PdO-NiO Nanoscale Heteromixture, Applied Surface Science, 420 (2017) 638-650.

[17] G.-J. Sun, H. Kheel, J.K. Lee, S. Choi, S. Lee, C. Lee, H_2S gas sensing properties of Fe_2O_3 nanoparticle-decorated NiO nanoplate sensors, Surface and Coatings Technology, 307 (2016) 1088-1095.

[18] R. Jiménez, M.L. Calzada, I. Bretos, J.C. Goes, A.S.B. Sombra, Dielectric properties of sol–gel derived $CaCu_3Ti_4O_{12}$ thin films onto Pt/TiO2/Si(100) substrates, Journal of the European Ceramic Society, 27 (2007) 3829-3833.

[19] R.L. Nigro, R.G. Toro, G. Malandrino, I.L. Fragalà, P. Fiorenza, V. Raineri, Effects of high temperature annealing on MOCVD grown $CaCu_3Ti_4O_{12}$ films on $LaAlO_3$ substrates, Surface and Coatings Technology, 201 (2007) 9243-9247.

[20] Y.L. Zhao, G.W. Pan, Q.B. Ren, Y.G. Cao, L.X. Feng, Z.K. Jiao, High dielectric constant in $CaCu_3Ti_4O_{12}$ thin film prepared by pulsed laser deposition, Thin Solid Films, 445 (2003) 7-13.

[21] W.-X. Yuan, S.K. Hark, H.Y. Xu, W.N. Mei, Investigation on the growth of $CaCu_3Ti_4O_{12}$ thin film and the origins of its dielectric relaxations, Solid State Sciences, 14 (2012) 35-39.

[22] Z. Lin, N. Li, Z. Chen, P. Fu, The effect of Ni doping concentration on the gas sensing properties of Ni doped SnO_2, Sensors and Actuators B: Chemical, 239 (2017) 501-510.

[23] M. Kaur, B.K. Dadhich, R. Singh, KailasaGanapathi, T. Bagwaiya, S. Bhattacharya, A.K. Debnath, K.P. Muthe, S.C. Gadkari, RF sputtered SnO_2: NiO thin films as sub-ppm H_2S sensor operable at room temperature, Sensors and Actuators B: Chemical, 242 (2017) 389-403.

[24] A.P. Rambu, L. Ursu, N. Iftimie, V. Nica, M. Dobromir, F. Iacomi, Study on Ni-doped ZnO films as gas sensors, Applied Surface Science, 280 (2013) 598-604.

[25] X. Wang, M. Zhao, F. Liu, J. Jia, X. Li, L. Cao, C_2H_2 gas sensor based on Ni-doped ZnO electrospun nanofibers, Ceramics International, 39 (2013) 2883-2887.

[26] Z. Jing, Fabrication and gas sensing properties of Ni-doped gamma-Fe_2O_3 by anhydrous solvent method, Materials Letters, 60 (2006) 3315-3318.

[27] Y. Wang, F. Qu, J. Liu, Y. Wang, J. Zhou, S. Ruan, Enhanced H_2S sensing characteristics of CuO-NiO core-shell microspheres sensors, Sensors and Actuators B: Chemical, 209 (2015) 515-523.

[28] X. Liu, J. Zhang, X. Guo, S. Wu, S. Wang, Enhanced sensor response of Ni-doped SnO_2 hollow spheres, Sensors and Actuators B: Chemical, 152 (2011) 162-167.

[29] W.-T. Li, X.-D. Zhang, X. Guo, Electrospun Ni-doped SnO_2 nanofiber array for selective sensing of NO_2, Sensors and Actuators B: Chemical, 244 (2017) 509-521.

[30] T. Vilic, E. Llobet, Nickel Doped WO_3 Nanoneedles Deposited by a Single Step AACVD for Gas Sensing Applications, Procedia Engineering, 168 (2016) 206-210.

[31] P. Thiruramanathan, A. Marikani, D. Madhavan, Optical and Electrical Properties of Sol-Gel Synthesized Calcium Copper Titanate Nanopowders, International Journal of ChemTech Research, 8 (2015) 293-299.

[32] O.A.A. Abdelal, A.A. Hassan, M.E.-S. Ali, Dielectric Properties of Calcium Copper Titanates ($CaCu_3Ti_4O_{12}$) Synthesized by Solid State Reaction, International Journal of Science and Research (IJSR), 3 (2012) 1356-1361.

[33] A.K. Rai, K.D. Mandal, D. Kumar, O. Parkash, Characterization of nickel doped CCTO: $CaCu_{2.9}Ni_{0.1}Ti_4O_{12}$ and $CaCu_3Ti_{3.9}Ni_{0.1}O_{12}$ synthesized by semi-wet route, Journal of Alloys and Compounds, 491 (2010) 507-512.

[34] M.A. Sulaiman, S.D. Hutagalung, J.J. Mohamed, Z.A. Ahmad, M.F. Ain, B. Ismail, High frequency response to the impedance complex properties of Nb-doped

$CaCu_3Ti_4O_{12}$ electroceramics, Journal of Alloys and Compounds, 509 (2011) 5701-5707.

[35] Y.F. Sun, S.B. Liu, F.L. Meng, J.Y. Liu, Z. Jin, L.T. Kong, J.H. Liu, Metal oxide nanostructures and their gas sensing properties: a review, Sensors, 12 (2012) 2610-2631.

[36] P. Shankar, J.B.B. Rayappan, Gas sensing mechanism of metal oxides: The role of ambient atmosphere, type of semiconductor and gases - A review, ScienceJet, 4 (2015) 126.

[37] R.J.B. Balaguru, Mimic of a Gas sensor, Metal Oxide Gas Sensing Mechanism, Factors Influencing the Sensor Performance and Role of nanomaterials based gas sensors, NPTEL – Electrical & Electronics Engineering – Semiconductor Nanodevices.

[38] S. Choopun, N. Hongsith, E. Wongrat, Metal-Oxide Nanowires for Gas Sensors, (2012).

[39] M.A. Ponce, M.A. Ramirez, F. Schipani, E. Joanni, J.P. Tomba, M.S. Castro, Electrical behavior analysis of n-type $CaCu_3Ti_4O_{12}$ thick films exposed to different atmospheres, Journal of the European Ceramic Society, 35 (2015) 153-161.

[40] N.Z. Misak, Langmuir isotherm and its application in ion-exchange reactions, Elsevier Science Publishers B.V., Amsterdam, 21 (1993) 53-64.

[41] A. Thain, A. Jaber, Y. Platon, A. Herve, G. Peres, B. Pasquier, L. Evain, G. Cambon, F. Harly, H. Lenquette, Thin Diffraction Grating Technology, 9th European Conference on Antennas and Propagation, (2015).

[42] J. Bernstein, G.R. Desiraju, J.R. Helliwell, T. Mak, P. Müller, P. Paufler, H. Schenk, P. Spadon, D. Viterbo, Crystal Structure Analysis Principles and Practice, 2009.

[43] F. JAUNDRELL-THOMPSON, W.J. ASHWORTH, X-Ray Physics and Equipment, 1965.

[44] Exploration Technique: X-Ray Diffraction (XRD), in, National Renewable Energy Laboratory, 2013.

[45] U.B.A.N.G. EROR, Raman Spectra of Titanium Dioxide, OURNAL OF SOLID STATE CHEMISTRY 42 (1982) 276-282.

[46] I. Ganesh, A.K. Gupta, P.P. Kumar, P.S. Sekhar, K. Radha, G. Padmanabham, G. Sundararajan, Preparation and characterization of Ni-doped TiO_2 materials for photocurrent and photocatalytic applications, ScientificWorldJournal, 2012 (2012) 127326.

[47] J.F. Fernández, P. Leret, J.J. Romero, J. de Frutos, M.Á. de la Rubia, M.S. Martín-González, J.L. Costa-Krämer, J.L.G. Fierro, A. Quesada, M.Á. García, Proofs of the Coexistence of Two Magnetic Contributions in Pure and Doped $CaCu_3Ti_4O_{12}$ Giant Dielectric Constant Ceramics, Journal of the American Ceramic Society, 92 (2009) 2311-2318.

[48] J. Xu, L. He, W. Xu, H. Tang, H. Liu, T. Han, C. Zhang, Y. Zhang, Facile synthesis of porous $NiCo_2O_4$ microflowers as high-performance anode materials for advanced lithium-ion batteries, Electrochimica Acta, 145 (2014) 185-192.

[49] P.R. Bueno, R. Tararan, R. Parra, E. Joanni, M.A. Ramírez, W.C. Ribeiro, E. Longo, J.A. Varela, A polaronic stacking fault defect model for $CaCu_3Ti_4O_{12}$ material: an approach for the origin of the huge dielectric constant and

semiconducting coexistent features, Journal of Physics D: Applied Physics, 42 (2009) 055404.

[50] M. Xue, Y. Tan, Hollow alloy nanostructures templated by Au nanorods: synthesis, mechanistic insights, and electrocatalytic activity, Nanoscale, 6 (2014) 12500-12514.

[51] M. Kuang, T.T. Li, H. Chen, S.M. Zhang, L.L. Zhang, Y.X. Zhang, Hierarchical $Cu_2O/CuO/Co_3O_4$ core-shell nanowires: synthesis and electrochemical properties, Nanotechnology, 26 (2015) 304002.

[52] W. Hao, H. Wu, P. Xu, Y. Shi, S. Yang, M. Wang, L. Sun, E. Cao, Y. Zhang, Influence of Sb-doping on dielectric properties of $NaCu_3Ti_3TaO_{12}$ ceramics and relevant mechanism(s), Ceramics International, 43 (2017) 3631-3638.

[53] A. Pareek, P. Paik, P.H. Borse, Stable hydrogen generation from Ni- and Co-based co-catalysts in supported CdS PEC cell, Dalton transactions, 45 (2016) 11120-11128.

[54] I. Luisetto, S. Tuti, C. Battocchio, S. Lo Mastro, A. Sodo, $Ni/CeO_2–Al_2O_3$ catalysts for the dry reforming of methane: The effect of $CeAlO_3$ content and nickel crystallite size on catalytic activity and coke resistance, Applied Catalysis A: General, 500 (2015) 12-22.

[55] S.R. Nalage, M.A. Chougule, S. Sen, V.B. Patil, Novel method for fabrication of NiO sensor for NO_2 monitoring, Journal of Materials Science: Materials in Electronics, 24 (2012) 368-375.

[56] A. Natkaeo, Modification of calcium copper titanate thin films by adding Ag compounds and their H_2S gas sensing response in: Physics, Chulalongkorn, 2016.

APPENDIX

Appendix A

Ni-doping concentration

In thesis, we used two nickel compound namely, nickel oxide (NiO) and nickel (II) acetate ($C_4H_6NiO_4$). In order to doped Ni in CCTO films, the percentage of Ni concentration for nickel oxide can be calculated by following expression.

$$\left(\frac{\frac{g_{NiO}}{MW_{NiO}}}{\frac{g_{Ca(C_2H_3O_2)_2\cdot xH_2O}}{MW_{Ca(C_2H_3O_2)_2\cdot xH_2O}}}\right)\left(\frac{MW_{Ni}}{MW_{CCTO}}\right)\times 100 = \ \ldots\ldots\% \text{ Ni by weight}$$

$$\left(\frac{\frac{g_{NiO}}{74.7}}{\frac{0.855}{158.17}}\right)\left(\frac{58.693}{613.37}\right)\times 100 = \ \ldots\ldots\% \text{ Ni by weight}$$

$$g_{Ni}\times 23.69 = \ \ldots\ldots\% \text{ Ni by weight}$$

In this thesis, we tried to dope Ni 1.42% (~ 1%), 4.3% (~ 4%) and 7.09% (~ 7%) by weight. By following the Equation above, we weighed Ni 0.0598 g, 0.1795 g and 0.2992 g for Ni doped 1%, 4% and 7% by weight, respectively. However, the quantity of Ni in our films were later measured from EDX experiments which are 0.46 %, 1.51% and 2.29% by weight instead of 1%, 4% and 7% by weight.

In order to doped Ni in CCTO films, the percentage of Ni concentration for nickel (II) acetate ($C_4H_6NiO_4$) can be calculated by following expression.

$$\left(\frac{\frac{g_{C_4H_6NiO_4}}{MW_{C_4H_6NiO_4}}}{\frac{g_{Ca(C_2H_3O_2)_2\cdot xH_2O}}{MW_{Ca(C_2H_3O_2)_2\cdot xH_2O}}}\right)\left(\frac{MW_{Ni}}{MW_{CCTO}}\right)\times 100 = \ \ldots\ldots\% \text{ Ni by weight}$$

$$\left(\frac{\frac{g_{C_4H_6NiO_4}}{176.78}}{\frac{0.855}{158.17}}\right)\left(\frac{58.693}{613.37}\right)\times 100 = \ \ldots\ldots\% \text{ Ni by weight}$$

$$g_{Ni}\times 10.01 = \ \ldots\ldots\% \text{ Ni by weight}$$

In this thesis, we tried to dope Ni 0.60% (~ 1%), 1.75% (~ 2%), 2.99% (~ 3%), 4.19% (~ 4%) and 5.39% (~ 5%) by weight. By following the Equation above, we weighed Ni 0.0598 g, 0.1795 g, 0.2292 g, 0.4188 g and 0.5385 g for Ni doped 1%, 2%, 3%, 4% and 5% by weight, respectively. However, the quantity of Ni in our films were later measured from EDX experiments which are 0.35%, 0.59%, 1.25%, 1.78% and 1.92%by weight instead of 1%, 2%, 3%, 4% and 5% by weight.

Appendix B

XRD database

The XRD patterns of the CCTO thin films were used to characterize the crystal structure by comparison with the XRD database from The International Centre for Diffraction Data (ICDD) which is shown as follow

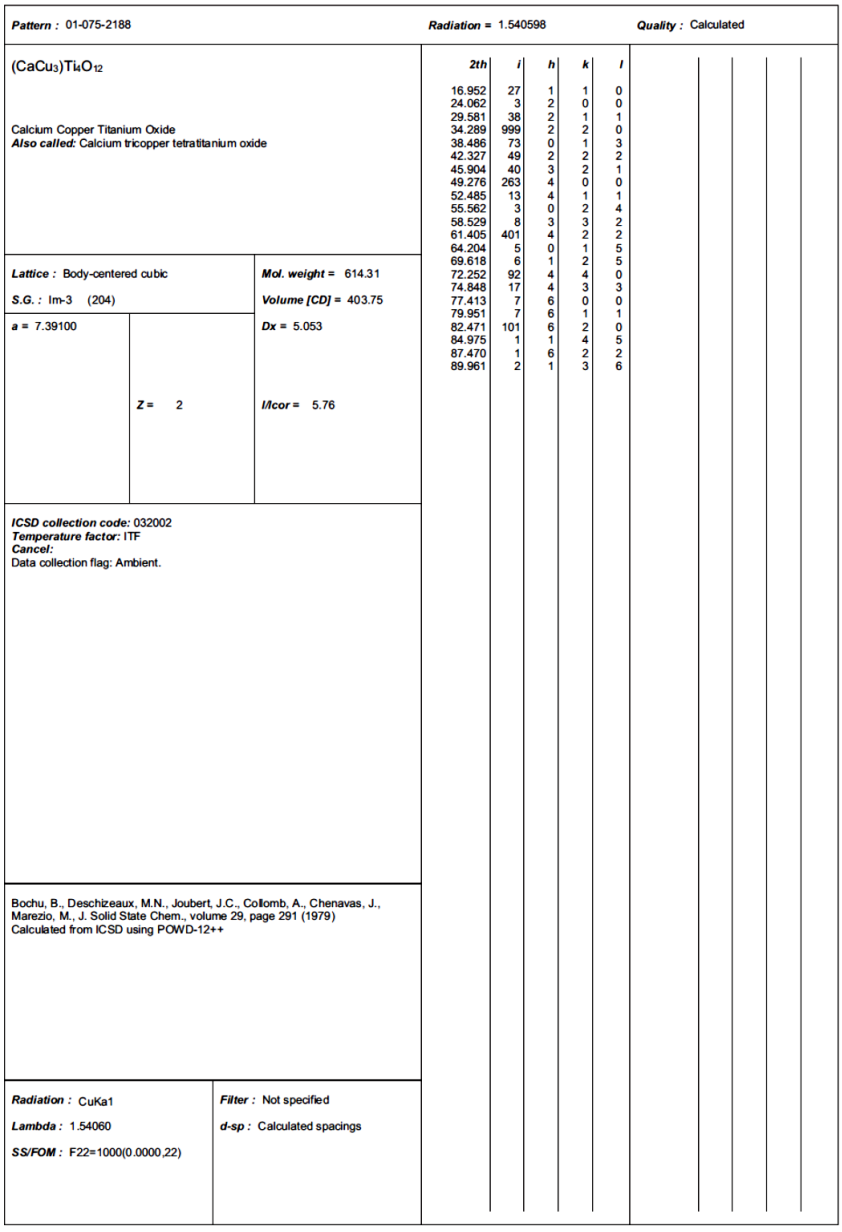

Pattern : 01-075-2188 ***Radiation =*** 1.540598 ***Quality :*** Calculated

$(CaCu_3)Ti_4O_{12}$

Calcium Copper Titanium Oxide
Also called: Calcium tricopper tetratitanium oxide

Lattice : Body-centered cubic
S.G. : Im-3 (204)
a = 7.39100
Z = 2
Mol. weight = 614.31
Volume [CD] = 403.75
Dx = 5.053
I/Icor = 5.76

ICSD collection code: 032002
Temperature factor: ITF
Cancel:
Data collection flag: Ambient.

Bochu, B., Deschizeaux, M.N., Joubert, J.C., Collomb, A., Chenavas, J., Marezio, M., J. Solid State Chem., volume 29, page 291 (1979)
Calculated from ICSD using POWD-12++

Radiation : CuKa1
Lambda : 1.54060
SS/FOM : F22=1000(0.0000,22)
Filter : Not specified
d-sp : Calculated spacings

2th	i	h	k	l
16.952	27	1	1	0
24.062	3	2	0	0
29.581	38	2	1	1
34.289	999	2	2	0
38.486	73	0	1	3
42.327	49	2	2	2
45.904	40	3	2	1
49.276	263	4	0	0
52.485	13	4	1	1
55.562	3	0	2	4
58.529	8	3	3	2
61.405	401	4	2	2
64.204	5	0	1	5
69.618	6	1	2	5
72.252	92	4	4	0
74.848	17	4	3	3
77.413	7	6	0	0
79.951	7	6	1	1
82.471	101	6	2	0
84.975	1	1	4	5
87.470	1	6	2	2
89.961	2	1	3	6

Pattern : 00-021-1276 **Radiation =** 1.540598 **Quality :** High

TiO_2

Titanium Oxide
Rutile, syn
Also called: titania

Lattice : Tetragonal
S.G. : P42/mnm (136)

a = 4.59330
c = 2.95920

Z = 2

Mol. weight = 79.90
Volume [CD] = 62.43
Dx = 4.250
Dm = 4.230
I/Icor = 3.40

General comments: No impurity over 0.001%.
Vickers hardness number: VHN_{100}=1132-1187.
Sample source or locality: Sample obtained from National Lead Co., South Amboy, New Jersey, USA.
General comments: Pattern reviewed by Syvinski, W., McCarthy, G., North Dakota State Univ, Fargo, North Dakota, USA, *ICDD Grant-in-Aid* (1990). Agrees well with experimental and calculated patterns.
General comments: Two other polymorphs, anatase (tetragonal) and brookite (orthorhombic), converted to rutile on heating above 700 C.
General comments: Additional weak reflections [indicated by brackets] were observed.
Optical data: A=2.9467, B=2.6505, Sign=+
Additional pattern: Validated by calculated pattern.
General comments: Optical data on specimen from *Dana's System of Mineralogy, 7th Ed.*, I 555.
General comments: Naturally occurring material may be reddish brown.
Color: White
Reflectance: Opaque mineral optical data on specimen from Sweden: $R_3R\%$= 20.3, Disp.=Std.
Temperature of data collection: Pattern taken at 25 C.
Data collection flag: Ambient.

Natl. Bur. Stand. (U.S.) Monogr. 25, volume 7, page 83 (1969)

Radiation : CuKa1
Lambda : 1.54056
SS/FOM : F30=108(0.0087,32)

Filter : Monochromator crystal
d-sp : Not given
Internal standard : W

2th	i	h	k	l
27.447	100	1	1	0
36.086	50	1	0	1
39.188	8	2	0	0
41.226	25	1	1	1
44.052	10	2	1	0
54.323	60	2	1	1
56.642	20	2	2	0
62.742	10	0	0	2
64.040	10	3	1	0
65.480	2	2	2	1
69.010	20	3	0	1
69.790	12	1	1	2
72.410	2	3	1	1
74.411	1	3	2	0
76.510	4	2	0	2
79.822	2	2	1	2
82.335	6	3	2	1
84.260	4	4	0	0
87.464	2	4	1	0
89.557	8	2	2	2
90.708	4	3	3	0
95.275	6	4	1	1
96.017	6	3	1	2
97.176	4	4	2	0
98.514	1	3	3	1
105.099	2	4	2	1
106.019	2	1	0	3
109.406	2	1	1	3
116.227	4	4	0	2
117.527	4	5	1	0
120.059	8	2	1	3
122.788	8	4	3	1
123.660	8	3	3	2
131.847	6	4	2	2
136.549	8	3	0	3
140.052	12	5	2	1
143.116	2	4	4	0
155.869	2	5	3	0

Pattern : 00-029-1360 **Radiation =** 1.540598 **Quality :** High

TiO_2

Titanium Oxide
Brookite

Lattice : Orthorhombic
S.G. : Pcab (61)

a = 5.45580
b = 9.18190
c = 5.14290
a/b = 0.59419
c/b = 0.56011

Z = 8

Mol. weight = 79.90
Volume [CD] = 257.63
Dx = 4.120
Dm = 4.140

Optical data: A=2.5831, B=2.5843, Q=2.7004, Sign=+, 2V=~28°
Additional pattern: To replace 00-016-0617 and validated by calculated pattern.
Color: Black
Additional pattern: See ICSD 36408 (PDF 01-076-1934).
Sample source or locality: Specimen from Magnet Cove, Arkansas, USA (USNM 97661).
Analysis: Spectrographic analysis: 0.1-1.0% Si; 0.01-0.1% each of Al, Fe, and V; 0.001-0.01% Mg.
General comments: Niobian brookite from Mozambique [Chemical analysis (wt.%): Ti O2 80.7, Nb2 O5 14.1, FeO 5.53]; Carvalho et al., *Rev. Cien. Geol. Ser. A*, **7** 61 (1974) reports an identical pattern.
Temperature of data collection: Pattern taken at 25 C.
General comments: Intensities verified by calculated pattern.
Data collection flag: Ambient.

Natl. Bur. Stand. (U.S.) Monogr. 25, volume 3, page 57 (1964)

Radiation : CuKa1
Lambda : 1.54056
SS/FOM : F30= 58(0.0115,45)

Filter : Beta
d-sp : Not given

2th	i	h	k	l
25.340	100	1	2	0
25.689	80	1	1	1
30.808	90	1	2	1
32.791	4	2	0	0
36.252	25	0	1	2
37.297	18	2	0	1
37.934	6	1	3	1
38.371	4	2	2	0
38.576	4	2	1	1
39.205	5	0	4	0
39.967	8	1	1	2
40.153	18	0	2	2
42.340	16	2	2	1
46.072	16	0	3	2
48.012	30	2	3	1
49.173	18	1	3	2
49.694	3	2	1	2
52.012	3	2	4	0
54.205	20	3	2	0
55.234	30	2	4	1
55.711	5	1	5	1
57.176	13	1	1	3
57.685	2	2	3	2
59.991	7	1	2	3
62.065	10	0	5	2
63.065	4	1	6	0
63.415	9	3	1	2
63.643	12	2	5	1
64.104	12	2	0	3
64.603	6	1	3	3
65.002	10	2	1	3
65.876	9	1	6	1
68.768	5	4	0	0
70.432	8	3	3	2
71.490	3	4	0	1
71.931	2	2	3	3
73.648	2	0	0	4
76.948	10	0	2	4
79.024	2	4	3	1
79.283	1	1	2	4
83.643	4	3	3	3
84.287	2	0	8	0
84.724	2	4	4	1
86.743	4	0	4	4
95.590	3	5	2	1
*95.590	3	4	2	3
95.993	2	2	8	1
97.609	4	3	2	4
102.559	2	1	2	5
103.201	4	3	7	2
*103.201	4	2	5	4

Pattern : 03-065-5714 **Radiation =** 1.540598 **Quality :** Calculated

TiO_2

Titanium Oxide

Lattice : Body-centered tetragonal
S.G. : I41/amd (141)

a = 3.78500
c = 9.51400

Z = 4

Mol. weight = 79.90
Volume [CD] = 136.30
Dx = 3.894
I/Icor = 5.04

NIST M&A collection code: A 50867 ST1243 1
Temperature factor: TF Isotropic TF given by author
Sample preparation: Commercial pigmentary material was used
Remarks from ICSD/CSD: Anatase-synthetic
Data collection flag: Ambient.

Cromer, D.T., Herrington, K., J. Am. Chem. Soc., volume 77, page 4708 (1955)
Calculated from NIST using POWD-12++

Radiation : CuKa1
Lambda : 1.54060
SS/FOM : F30=597(0.0014,35)

Filter : Not specified
d-sp : Calculated spacings

2th	i	h	k	l
25.304	999	1	0	1
36.949	56	1	0	3
37.793	175	0	0	4
38.566	71	1	1	2
48.036	238	2	0	0
53.886	148	1	0	5
55.061	146	2	1	1
62.107	23	2	1	3
62.684	103	2	0	4
68.756	49	1	1	6
70.287	49	2	2	0
74.053	4	1	0	7
75.046	74	2	1	5
76.032	20	3	0	1
80.740	3	0	0	8
82.156	5	3	0	3
82.672	35	2	2	4
83.154	15	3	1	2
93.244	5	2	1	7
94.202	17	3	0	5
95.162	19	3	2	1
98.325	11	1	0	9
99.812	7	2	0	8
101.236	5	3	2	3
107.478	24	3	1	6
108.988	12	4	0	0
112.826	2	3	0	7
113.868	22	3	2	5
114.918	13	4	1	1
118.472	35	2	1	9
*118.472	35	1	1	10
120.117	6	2	2	8
121.749	5	4	1	3
122.353	15	4	0	4
122.921	10	3	3	2
131.049	20	4	2	0
132.007	5	1	0	11
135.995	3	3	2	7
137.389	19	4	1	5
142.878	1	4	0	6
143.850	7	3	0	9

Pattern : 00-046-1212 ***Radiation =*** 1.540598 ***Quality :*** High

Al_2O_3

Aluminum Oxide
Corundum, syn
Also called: α- Al2 O3

Lattice : Rhombohedral
S.G. : R-3c (167)

a = 4.75870
c = 12.99290
Z = 6

Mol. weight = 101.96
Volume [CD] = 254.81
Dx = 3.987

Sample source or locality: The sample is an alumina plate as received from *ICDD.*
General comments: Unit cell computed from d_{obs}.
Optical data: A=1.7604, B=1.7686, Sign=-
Data collection flag: Ambient.

Huang, T., Parrish, W., Masciocchi, N., Wang, P., Adv. X-Ray Anal., volume 33, page 295 (1990)

Radiation : CuKa1
Lambda : 1.54056
SS/FOM : F25=379(0.0026,25)

Filter : Not specified
d-sp : Diffractometer

2th	*i*	*h*	*k*	*l*
25.579	45	0	1	2
35.153	100	1	0	4
37.777	21	1	1	0
41.676	2	0	0	6
43.356	66	1	1	3
46.176	1	2	0	2
52.550	34	0	2	4
57.497	89	1	1	6
59.740	1	2	1	1
61.118	2	1	2	2
61.300	14	0	1	8
66.521	23	2	1	4
68.214	27	3	0	0
70.420	1	1	2	5
74.299	2	2	0	8
76.871	29	1	0	10
77.226	12	1	1	9
80.422	1	2	1	7
80.700	2	2	2	0
83.217	1	3	0	6
84.359	3	2	2	3
85.143	1	1	3	1
86.363	2	3	1	2
86.503	3	1	2	8
88.997	9	0	2	10

Appendix C

Conference Presentations:

International Presentation:

2016, Arisara Boontum, Satreerat K. Hodak, Jose H. Hodak, Anurat Wisitsoraat and Disayut Phokharakul. Gas Sensing Response of Nickel Doped Calcium Copper Titanate Thin Films Synthesized by Sol-Gel Method. Poster presentation at the 3rd International congress on Advanced Materials (AM 2016) at Centara Grand, Central Plaza Ladprao, Bangkok, Thailand (November 27-30 2016) Code: ENM-P-33.

Local Presentations:

2017, Arisara Boontum, Satreerat K. Hodak, Jose H. Hodak, Anurat Wisitsoraat and Disayut Phokharakul. Gas Sensing Response of Nickel Doped Calcium Copper Titanate Thin Films Synthesized by Sol-Gel Method. Poster presentation at Siam Physics Congress 2017 at Rayong Marriott & Spa, Rayong, Thailand (May 24-26 2017) Code: P-SI09-248

VITA

Miss Arisara Boontum was born on 10th October 1991 in Surin province, Thailand. In 2009, she graduated high school from Surawittayakarn school, surin. She got bachelor degree in Physics, Department of Physics, Faculty of Science, Ubon Ratchathani university, in 2013 and she received the Science Achievement Scholarship of Thailand (SAST) in 2010 – 2015. She has been studying the master degree in Physics, Department of Physics, Faculty of Science, Chulalongkorn University in 2014.